Large Area Wireless Power Transfer with Coupled Relay Resonators

Xingyi Shi

A dissertation
submitted in partial fulfillment of the
requirements for the degree of

Doctor of Philosophy

University of Washington

2019

Reading Committee:

Joshua R. Smith, Chair

Matthew S. Reynolds

Chet Moritz

Shwetak Patel

Program Authorized to Offer Degree:
Department of Electrical and Computer Engineering

University of Washington

Abstract

Large Area Wireless Power Transfer
with Coupled Relay Resonators

Xingyi Shi

Chair of the Supervisory Committee:
Professor Joshua R. Smith
Computer Science & Engineering and Electrical & Computer Engineering

Emerging wireless charging technologies will become essential for medical implants, which currently require cables passing through patients' skin in order to provide power, or force the patient to undergo costly surgery operations to replace dead batteries. Likewise, makers of sensors and devices used on the factory floor are increasingly looking towards wireless power to eliminate the need for battery changes and eliminate downtime. Even the ever-increasing number and diversity of consumer electronics, such as smartphones, laptops, wearables, and VR headsets, will benefit from wireless power solutions that make battery charging more convenient.

Commercially available wireless chargers, such as those implementing the Qi standard, partially address the problem. Qi chargers can typically charge only one device at a time and require precise alignment of transmitter and receiver, and so are not effective as the number of electronics that need to be charged increases.

Magnetic resonance wireless power transfer systems, which use resonant coils as transmitters, have greater range and tolerance to misalignment. However, the size of the transmitter cannot be arbitrarily increased to fit any large area because large transmitter-to-receiver size ratios result in extreme inefficiency. As an enhancement on magnetic resonance, phased array transmitters explored in academic research can extend transmission range. However,

they have the tradeoff of increased cost and complexity, because each array element requires an independent RF source.

Non-magnetic methods of wireless power transfer, such as radiative ultra-high frequency beaming and tracking laser systems, have more extended power transfer range but much less efficiency, and they both have lower output power limits due to safety regulations. So whereas these methods may be useful for devices that only need small amount of energy and require long separation distances, they cannot be used for systems that require high power output while still being safe for use near humans and animals.

This dissertation focuses on the design of a wireless power transfer solution that can provide efficient wireless charging over a large area, can tolerate some amount of separation and misalignment, can charge multiple devices at the same time, at a reasonable complexity and cost, and can do all of this while staying well within safety regulations. To achieve this, we introduce an adaptive, passive wireless relay system to extend power transfer range.

A prototype of a centrally controlled array of reconfigurable relays (CARR) is implemented that can deliver power to multiple moving receivers. We show that the relay system is much more efficient at delivering power to small receivers over a large area than a single transmitter system, and has better uniformity of coverage. The CARR prototype can identify and adaptively route power to a new or moving receiver in as little as 120 microseconds.

Additionally, a method for enabling large area power transfer without a large transmitter is introduced, which proposes to use receivers themselves as relays when many receivers are in close proximity. We demonstrate a key step towards realizing this receivers-as-relay system by showing that a suitable routing configuration for delivering power to receivers can be identified using a load modulation technique.

Finally, in evaluating the safety of magnetic resonance systems, we conclude an interesting feature of coupled resonator systems which reduces safety concerns by reducing the SAR, a measure of the energy absorbed by biological tissue.

TABLE OF CONTENTS

LIST OF FIGURES

LIST OF TABLES

ACKNOWLEDGMENTS

Thanks to my advisor, Prof. Joshua R. Smith for his support and creative insights. A special thanks to all members past and present of the UW Sensor Systems Laboratory for their valuable help, motivation, and inspiring conversations.

DEDICATION

to my husband and my parents

Chapter 1

INTRODUCTION

The excitement of wireless power transfer was sparked by Nikola Tesla. He had a vision of delivering electricity wirelessly everywhere on earth and began carrying this out with the Wardenclyffe tower project in 1901 [39]. Because the project was ahead of its time and not well understood, funding was cut and it was never completed. In the 1960s, wireless power was revisited with pioneering work on microwave beamed power technology. After Brown demonstrated a microwave powered helicopter in 1964, NASA JPL showed power transfer of 30kW over one mile using microwaves [10, 9]. While impressive, these microwave systems are not suitable for all applications because they cannot be operated safely at these power levels around humans and require giant antenna infrastructure.

Tesla's work on resonant circuit has led to the start of modern wireless communication era. Nowadays wireless communications applications such as cell phones and WIFI have been integrated to most people's lifestyle, but the real era of wireless power has not arrived. The most widely adopted wireless power products are the wireless charger for electronic toothbrushes and the wireless cellphone charger. Both products are required to operate with contact distance because of the limitation of the deployed technology, which is magnetic induction that operates in near field and offers great efficiency but is lacking in distance freedom.

In the meantime, the motivation for larger area wireless power transfer is driven by patients with medical implants whose movement and health risk are limited by the charging environment, by factory operators who want to have all their robots automatically charged to finish their tasks on time and reduce down time, and by factories who want to save money and time on replacing thousands of batteries on the sensors used to monitor the conditions

and locations of items on conveyor belts [18, 45, 25, 34].

In 2007, Kurs et al. from MIT introduced a new way for wireless power transfer called magnetic resonance [24], which shows that resonators with high quality (Q) factor can wirelessly exchange power efficiently within certain loose coupling conditions. It means that efficient wireless power transfer can be achieved between high Q resonator with some separation distance, in comparing to the tight spacing requirement by the magnetic induction. Because it operates in near field, there is less energy that radiates out that causes EMI problems; Also, because the magnetic field carries the energy transfer, it has less impact on the human body. However, the range of the introduced magnetic resonance system is still limited by the transmitter and receiver size [43, 34].

Commonly studied non-magnetic means of power transfer include radiative UHF (ultra-high frequency) systems, which operate in the far-field and thus have longer range but far more limited power output capacity than near-field magnetic systems. Due to Friis path loss, the wireless power transfer efficiency of electromagnetic radiation method is proportional to $1/r^2$. Tracking lasers have become an interesting alternative to magnetic and UHF systems, delivering power over long distances by using coherent beams of laser light. Lasers can transfer power at long distance with a very focused beam and have very low loss when transferring in the air medium. But the efficiency of laser systems is mostly limited by the opto-electrical conversion efficiency. In addition to the lower efficiency, both systems have more limited power output capacity than near-field magnetic system for safety reasons. Thus, these technologies do not suit applications that need high power output and high efficiency applications.

As a result, due to the advantage of high output power capability, high efficiency, certain misalignment and separation tolerance, and better safety features to human than radiative methods, magnetic resonance method has become the most commonly chosen technique for applications with high power output and high efficiency requirement. The main challenge then becomes how to further extend the range of wireless power transfer with magnetic methods.

The simplest approach to extend coverage of wireless power transfer with magnetic resonance is to increase the transmitter size. But there are two problems with increasing transmitter coil size arbitrarily. First, as coil size increases, it becomes harder to build a highly efficient resonator at a target frequency. This is because as the coil size increases, the self resonant frequency goes down. When the self resonant frequency is lower than the target operating frequency, it is impossible to resonate. Second, a very large coil is not efficient at delivering power to a small receiver once their size ratio exceeds a limit. This is because larger transmitter to receiver ratio results in lower coupling.

From a research point of view, to make wireless power widely adopted, several challenges still remain to be solved:

- Increase wireless power transfer range while maintaining good efficiency.
- Enable delivering power to receivers that are much smaller than the power coverage space.
- Enable power delivery to moving receivers.
- Reduce the cost of the wireless power transfer system infrastructure.

1.1 Scope

The scope of this thesis work is to design and implement a magnetic resonant wireless power transfer system that solves the aforementioned challenges with coupled relay resonators. A passive relay is a resonator that sympathetically resonates when placed in an existing oscillating field whose frequency is the same as the relay's resonant frequency. The field generated by the relay effectively extends the range of the existing oscillating field.

Many works have demonstrated using relay to extend wireless power transfer range in one dimension[23, 50, 40], but the methodology of efficiently transferring power at any location in a 3D space has not been thoroughly studied.

My goal with this dissertation is to ***design a platform of reconfigurable relay resonators that can collectively and autonomously steer power to moving receivers quickly and efficiently and may cover a large space***.

More specifically, **reconfigurable** means that each relay in the platform can be reconfigured to be resonant or off-resonant to show or hide its existence; **collectively steer power** implies that the relays in the system can work together to form into the optimal configuration to any receiver locations; **autonomously to moving receivers** means that the system is capable of tracking multiple receivers at the same time and updating the power routing plan automatically; **quickly** indicates the selected tracking algorithm should be faster than the speed of moving receivers; **efficiently** is subjective so while improving the system efficiency can be an endless goal, we set the threshold of defining the system as efficient when the relay system is more efficient at delivering power when compared to a single transmitter with the same size and is optimized for its size.

The design and implementation towards the goal will be addressed step by step throughout the dissertation. Altogether the work will culminate in two different forms of a wireless power transfer system, which would address different applications of wireless power and are unavailable with the current state of art:

1. 2D planar array of relays with a centrally controlled transmitter.

2. Distributed system of receivers which can also act as relays.

Each of these culminating forms is discussed in more details in the following subsections.

1.1.1 Centrally controlled 2D planar array of relays

The ideal wireless power transfer system for patients with medical implants such as an artificial heart pump is that their implants can be wirelessly charged while they are sitting in the couch or sleeping in bed. For researchers on neurological studies, it is much preferred if the implants of test subjects for neural-recording and stimulation can be wirelessly powered

instead of cables going into their bodies. Power cables that go into bodies can not only severely increase the risk of infection, but also are more prone to be damaged. A confined space that is equipped with wireless power charging which can track one or more subjects' motion and steer power seamlessly is an ideal solution. For consumer electronics applications, it is desired if a table can be configured such that you can charge your phones, tablets and smart wearables all at once everywhere on the surface while keeping the cost down.

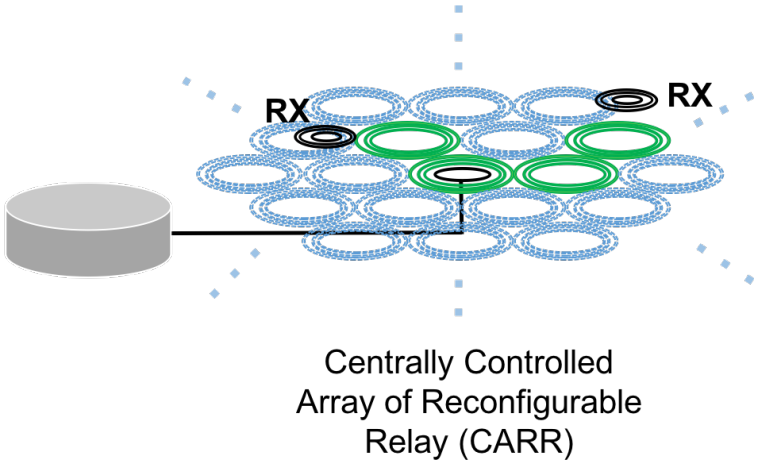

Figure 1.1: System illustration of CARR system. It consists of a central control unit that provide both the power signal to the single driven loop and the control signals for all the relays.

The centrally controlled 2D planar array of relays is designed for applications aforementioned. Fig.1.1 illustrates the concept of such system. **The system consists of a driven loop and a planar array of reconfigurable relays, of which the control of each relays are decided centrally by the transmitter based on optimal power delivery.** The benefit of centrally controlled transmitter is the ease of coordination on relay configuration plan, which makes receiver tracking fast. At the same time, because the control signal of the each relay is not a power signal, and adding each additional relay does not add much

construction complexity, the additional cost on top of traditional magnetic resonant system is minimal. The challenge to make this right is the coil geometry design which includes relay size and number of hops, as well as fast tracking algorithm.

1.1.2 Distributed Relay/Receivers

We want to deliver power to a large area without large infrastructure. Today's system can not do that because the power will all be consumed by the receivers closest to the transmitter, and when there are more other receivers placed in between the target receiver and the transmitter, the power cannot be delivered to it effectively.

So we propose a system that can configure itself into either receiver or relays to extend the power range further utilizing the existing receiver coils. Such a system can control whether it improves efficiency for others or gets charged itself.

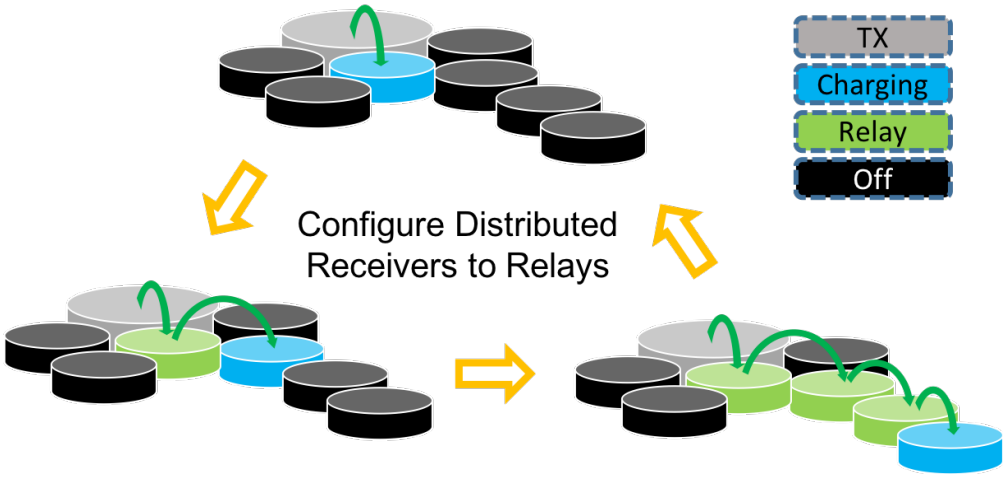

Figure 1.2: Illustration of a system that each distributed receiver can configure itself to be charged or to relay power to other receivers or to remove its existence to reduce interference.

The challenge of the proposed system is how to figure out which mode each device should be configured in. The transmitter does not have the receiver location information to be able

to tell all the receivers what they should do. Other existing localization methods are not only costly and complicated but does not provide enough resolution.

Because load modulation can transfer information only to the peers that are close enough to the load modulating coil, it can inherently be used to produce relative location information and exchange information with peers.

While there are a lot of steps to finish implementing the full system, we have completed several key steps in validating the proposal, which includes characterizing the speed and impact in efficiency of the load modulation with a hardware implementation, and experimental results that support that load modulation can be used for extracting relative location information. The design of the coil geometries and reconfigurability, as well as efficiency calculations follows the same rule as those of the centrally controlled transmitters. Fig.1.2 illustrate the concept of such system.

1.2 Roadmap

We begin with Chapter 2 on range extension of the basic 4-coil system with loop-coil-coil-loop structure, which is useful because they are the unit element of the relays. It starts with the overview on analyzing the coil system with circuit model analysis in Section 2.1. Section 2.2 describes the impact coil geometries on vertical range of a 4-coil system. Section 2.3 describes the limit of transmitter-receiver ratio of the single loop-coil transmitter for coverage extension. Section 2.4 talks about optimizing the coil geometry based on receiver motion to extend effective coverage area.

Chapter 3 characterizes the resonant modes of relay resonators when they are placed with different arrangements, and extracts different techniques for optimizing range extension with one-dimensional relay arrays. Chapter 4 describes the change of impedance characteristics with different relay arrangement, which is an important factor when designing to optimize efficiency with impedance matching. Chapter 5 presents about the design and rules for reconfigurable relay systems and the implementation of a centrally controlled 2D planar array prototype. Chapter 6 presents using load-modulation for communication with coupled res-

onators, how to utilize its waveform characteristics to exchange location information between receivers and its trade-off between efficiency and data rate. Lastly we talk about the regulation on wireless power transfer and analyze safety related issues when using relay resonators in Chapter 7.

In summary, this thesis work will explore the strategies, challenges, and solutions to enable large area wireless power with reconfigurable relay resonator arrays.

Chapter 2

WIRELESS POWER TRANSFER RANGE WITH 4-COIL SYSTEM

It is all started with a phenomenon called electromagnetic induction. Ampere's circuital law tells us that a flowing current loop generates a magnetic field which is perpendicular to the current loop. Faraday's law of induction tells us that if we put a closed wire loop in a changing magnetic field, an electromotive force will be induced that is negative to the rate of the changing magnetic flux. This is how a magnetic field is generated with electrical current and then converted back to electrical current. James C. Maxwell then derived a set of equations that relate the electromagnetic fields and extended the original laws with correction terms. The pursuit of wireless power transfer is then started by Nikola Tesla. His famous Tesla coil can generate millions of volts, which is high enough to exceed the breakdown voltage of air as an insular, with only a small total input power. While this is one form of transferring power through air, it is limited in practicality. Later-on, he continued his wireless power research with the Wardenclyffe project with a vision of delivering power wirelessly everywhere on earth [39]. Even though the project was never finished with budget cut, his work has set the fundamentals for modern wireless communication systems. In addition to his contribution to the modern electric era, his work on the Tesla coil had introduced the concept of the coupled resonant electric circuit, which leads the invention of one wireless power transfer techniques – magnetic resonance with coupled resonators.

Magnetically coupled resonance happens when a tuned circuits starts to resonate when the circuit is placed near another resonating circuit with the same resonant frequency. With different resonator properties, the degree of coupling required for efficient wireless power transfer varies. In general, we need to worry about orientations and sizes of the coils, so

the geometry of a coil is critical. The geometry that reduces the amount of magnetic flux going through degrades the coupling. Distance is one important and major contributor of a reduced coupling. Thus, for a wireless power transfer system, we want to minimize the coupling required between two resonators for longer distance wireless power transfer. In 2007, Kurs et.al from MIT demonstrated a loop-coil-coil-loop topology for magnetic resonance that is able to transfer power wirelessly without tight coupling. The loosely coupled structure is called 4-coil system. This Chapter talks about the key parameters in a magnetic coupled resonator system that determines the system efficiency, as a function of k and Q, and how the range of the wireless power system changes with these parameters.

2.1 Overview of Magnetic Coupled 4-coil System

Magnetic coupled systems are commonly comprised of loops and coils. Both loops and coils form RLC networks that are either self-resonant or tuned to the same resonant frequency. The difference is that loops refer to low Q coils and generally single-turn, while coils refer to high Q coils and generally multi-turn.

Quality factor Q is a parameter that was originally invented to define the concept of "inductive purity" that is a ratio of the inductive reactance and the unavoidable resistance of the inductor. Because each coil can be represented with a serial R, L, C network as shown in Fig. 2.1, the Q of a coil can be expressed in Eq. 2.1, where ω_0 is the resonant frequency of the LC network.

$$Q = \frac{1}{R}\sqrt{\frac{L}{C}} = \frac{\omega_0 L}{R} \tag{2.1}$$

Quality factor Q can also be expressed as a ratio between energy stored in the resonator and the energy dissipated per cycle:

$$Q = 2\pi \frac{maximum\ energy\ stored}{total\ energy\ lost\ per\ cycle\ at\ resonance} \tag{2.2}$$

The greater the energy loss is, the less the wireless power transfer efficiency is; so one major technique in wireless power transfer system design is to optimize the Q of the coil. Details of optimizing the coil design can be found in [43].

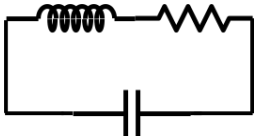

Figure 2.1: Lumped element model of a coil

The other important factor on determining how a wireless power transfer system performs is the coupling coefficient k between the resonators. The coupling coefficient is a physical parameter that indicates how well the flux is shared between each pair of the resonators. It is a function of the inductance of primary and secondary inductor, and the mutual inductance between the two (Eq. 2.3).

$$k_{12} = \frac{M_{12}}{\sqrt{L_1 L_2}} \tag{2.3}$$

The mutual inductance is determined by the shape, distance and alignment between the pair of inductors.

Furthermore, the amount of coupling can be categorized into three conditions: over coupled, under coupled, and critical coupled [32]. In under coupling, the linkage between the two resonators is small enough that there exists only one resonant mode and the flux of both resonators are in phase. In over coupling region, the interaction between the two resonators is large enough that the flux of the two resonators can resonate both in phase and out of phase, which results in two resonant modes. The difference in frequency of the two resonant modes becomes larger and larger as the coupling increases, but the peak gain of both resonant modes stays high during the change. This phenomenon is commonly referred as frequency splitting in wireless power transfer systems. Critical coupling refers to the between the over coupled and the under coupled region where highest transfer gain can be achieved with only one resonant mode. When the system is in under coupled zone, the efficiency decay is proportional to $1/d^3$, where d is the separation distance between the transmitter and receiver [32]. Thus, the critical coupling distance is a good measure of the wireless power transfer range for such systems.

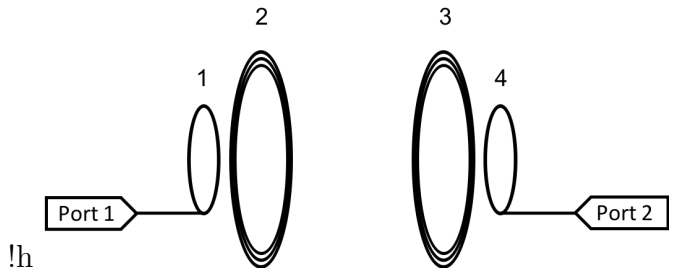

!h

Figure 2.2: Illustration of a 4-coil magnetic coupled resonator system

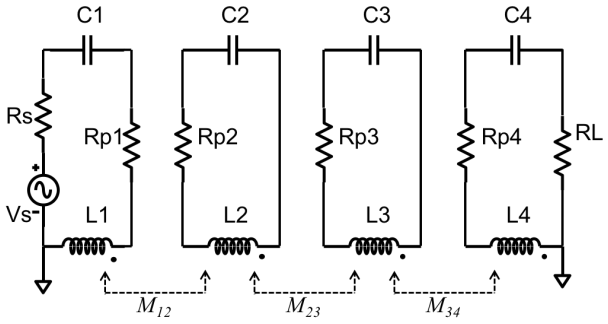

!h

Figure 2.3: Eq. ivalent circuit model of a 4-coil magnetic coupled resonator system

A 4-coil system is a commonly chosen topology for wireless power transfer system because it has longer range than 2-coil and 3-coil systems [22]. For a 4-coil system illustrated in Fig. 2.2, *coil* 1 is a loop that is connected to the power signal, referred to the **driven loop**, and *coil* 4 is a loop that is connected to the load, referred to the **load loop**. *Coil* 2 and *coil* 3 are high Q resonators that are placed near each loop without any ohmic connection.

2.1.1 Circuit Model Analysis

In order to characterize the efficiency of a 4-coil system to be used as a wireless power transfer method, we model the system with lumped elements as shown in Fig. 2.3. Each coil can be represented with a serial R, L, C network, which comprises the parasitic resistance, inductance, and capacitance respectively. The mutual inductance between each coil is rep-

resented with M. Applying Kirchhoff's voltage law (KVL), we can generate a equation for each loop. The mutual inductance links all of the equations and form a matrix in Eq. 2.4. In the matrix, the crossing coupling between each loop and the non-adjacent coil is so small that it is ignored. Solving for I, we can obtain the voltage gain of the system in Eq. 2.7. According to [32], we can express S_{21} in Eq. 2.8. Then we can obtain $|S_{21}|$ of a 4-coil system in Eq. 2.9 by plugging Eq. 2.7 to Eq. 2.8. Thus, the efficiency of the coil system can be expressed by $|S_{21}|^2$ in Eq. 2.10 if the source impedance and load impedance are conjugately matched.

$$\begin{bmatrix} Vs \\ 0 \\ 0 \\ 0 \end{bmatrix} = \begin{bmatrix} Z_1 & j\omega M_{12} & j\omega M_{13} & j\omega M_{14} \\ j\omega M_{12} & Z_2 & j\omega M_{23} & j\omega M_{24} \\ j\omega M_{13} & j\omega M_{23} & Z_3 & j\omega M_{34} \\ j\omega M_{14} & j\omega M_{24} & j\omega M_{34} & Z_4 \end{bmatrix} \begin{bmatrix} I_1 \\ I_2 \\ I_3 \\ I_4 \end{bmatrix} \tag{2.4}$$

$$k_{ij} = \frac{M_{ij}}{\sqrt{L_i L_j}} \tag{2.5}$$

$$V_L = I_n \times R_L \tag{2.6}$$

$$\left.\frac{V_L}{V_S}\right|_{\omega=\omega_0} = \frac{ik_{12}k_{23}k_{34}Q_2Q_3\sqrt{Q_1Q_4}}{(Q_1Q_2k_{12}^2+1)(Q_3Q_4k_{34}^2+1)+Q_2Q_3k_{23}^2} \tag{2.7}$$

$$S_{21} = 2\frac{V_L}{V_S}\sqrt{\frac{R_S}{R_L}} \tag{2.8}$$

$$|S21|_4 = \frac{2k_{12}k_{23}k_{34}Q_2Q_3\sqrt{Q_1Q_4}}{(Q_1Q_2k_{12}^2+1)(Q_3Q_4k_{34}^2+1)+Q_2Q_3k_{23}^2} \tag{2.9}$$

$$\eta = |S21|^2 \tag{2.10}$$

2.2 Range of 4-coil System in Co-axial Dimension

When we talk about large area wireless power transfer, we also want to know the vertical range capability of the transmitter. Let's assume two coils are co-axially aligned along the z-axis (Fig. 2.4). We want to know the maximum distance that the transmitter is still efficient. The critical coupling coefficient can be used for a convenient replacement for distance. Thus, we will discuss how k and Q of the coil system affect the critical coupling distance and the corresponding efficiency, thereby optimizing the vertical range capability.

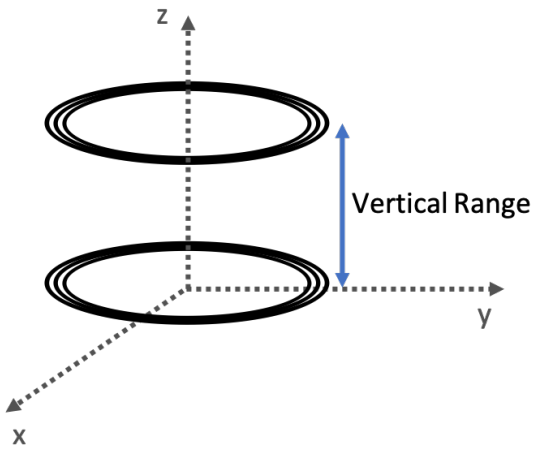

Figure 2.4: Vertical range of a 4-coil system.

To highlight the impact of k and Q to the vertical range, we use a symmetrical model of the 4-coil system where the receiver coil geometry is identical to the transmitter coil. We can simplify the V_L/V_S expression in Eq. 2.7 and the S_{21} expression in Eq. 2.9 to Eq. 2.11 and Eq. 2.12 respectively with four variables: k_{lc}, k_{cc}, Q_l and Q_c. k_{lc} represents the coupling between a loop to its adjacent coil, k_{cc} represents the coupling between two coils,

Q_l represents the Q of the loop, and Q_c represents the Q of the coil.

$$\left.\frac{V_L}{V_S}\right|_{\omega=\omega_0,symetric} = \frac{ik_{cc}k_{lc}^2Q_c^2Q_l}{(1+Q_lQ_ck_{lc}^2)^2+Q_c^2k_{cc}^2}^1 \tag{2.11}$$

$$|S21|_{4,symetric}= \frac{2k_{cc}k_{lc}^2Q_c^2Q_l}{(1+Q_lQ_ck_{lc}^2)^2+Q_c^2k_{cc}^2} \tag{2.12}$$

By finding the expression of k_{cc} when the derivative of $|S21|$ with k_{cc} equals to zero, we obtain $k_{critical}$ in Eq. 2.13.

$$k_{critical} = \frac{1}{Q_c} + k_{lc}^2Q_l \tag{2.13}$$

Plug in Eq. 2.13 to Eq. 2.12, $|S21|_{critical}$ is obtained in Eq. 2.14.

$$|S21|_{critical}= \frac{Q_lQ_ck_{lc}^2}{Q_lQ_ck_{lc}^2+1} \tag{2.14}$$

Based on Eq. 2.13, when Q_c is the only parameter increased, $k_{critical}$ decreases, which means the vertical range is longer. From Eq. 2.14, $|S21|_{critical}$ approaches 1 as either Q_l or Q_c increases while the rest parameters are unchanged. Thus, we always want to improve Q_c for better efficiency and longer vertical range if possible. But we are practically limited to Q_c due to the increase in parasitic resistance with the increase in inductance. In addition, improving Q_c of a coil that works with high operation frequency is challenging because the skin effect causes a larger parasitic resistance, which degrades Q further. However, if we increase Q_l only, the increase in $S21_{critical}$ comes with the drawback of increased $k_{critical}$, which means that the vertical range becomes more limited. A similar effect happens with changing k_{lc} only. To compare how effective Q_l and k_{lc} are at adjusting the efficiency and vertical range trade-off, we compute the derivative of $S21_{critical}$ and $k_{critical}$ with respective to Q_l and k_{lc} respectively in Eq. 2.15 and Eq. 2.16.

$$\frac{d|S21|_{critical}}{dQ_l} = \frac{k_{lc}^2Q_c}{(Q_lQ_ck_{lc}^2+1)^2} \tag{2.15}$$

$$\frac{d|S21|_{critical}}{dk_{lc}} = \frac{2Q_lQ_ck_{lc}}{(Q_lQ_ck_{lc}^2+1)^2} \tag{2.16}$$

[1]Eq. 2.11 is a corrected version of Eq. 7 in [32]. The original equation has a typo; Q_{loop} in the numerator should not be squared.

$$\frac{dk_{critical}}{dQ_l} = k_{lc}^2 \tag{2.17}$$

$$\frac{dk_{critical}}{dk_{lc}} = 2Q_l k_{lc} \tag{2.18}$$

From the derivative expressions of $|S21|_{critical}$ and $k_{critical}$, it can be concluded that adjusting k_{lc} is more effective at changing efficiency and vertical range when $k_{lc} < 2Q_l$. This assumption is always valid when Q_l is greater than 0.5, which applies to most of the coil systems. We plot the simulated relationship of how Q_l and k_{lc} affect efficiency and vertical range in Fig. 2.5 and Fig. 2.6, where x-axis k_{cc} is the measure of vertical range between the transmitter and receiver. The two figures show that increasing Q_l or k_{lc} while keeping the other parameters unchanged makes the $|S21|_{critical}$ larger and vertical range shorter.

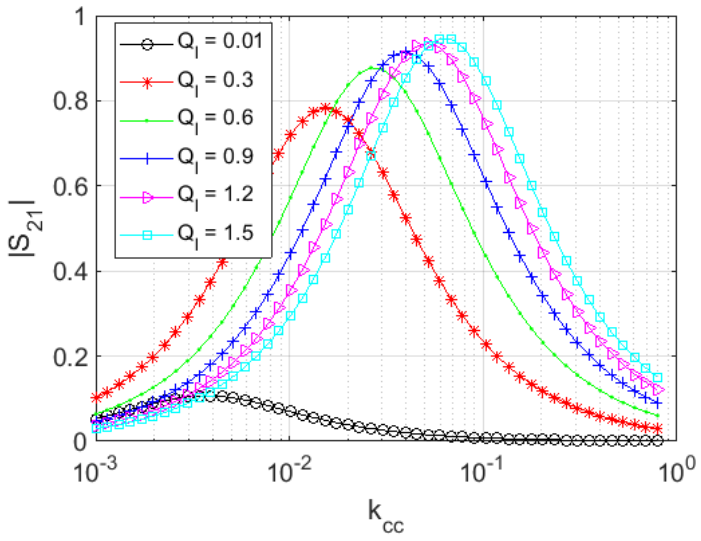

Figure 2.5: Simulated result of how Q_l affects $|S21|$ and critical coupling range. (Q_c=300, k_{lc}=0.2)

In summary, $k_{critical}$ is positively proportional to $S21_{critical}$, which means vertical range can be traded for maximum achievable efficiency and vice versa. This relationship is also described in [32]. In addition, optimizing Q_c when possible is always good for improving vertical range and efficiency. To control the tradeoff between efficiency and vertical range,

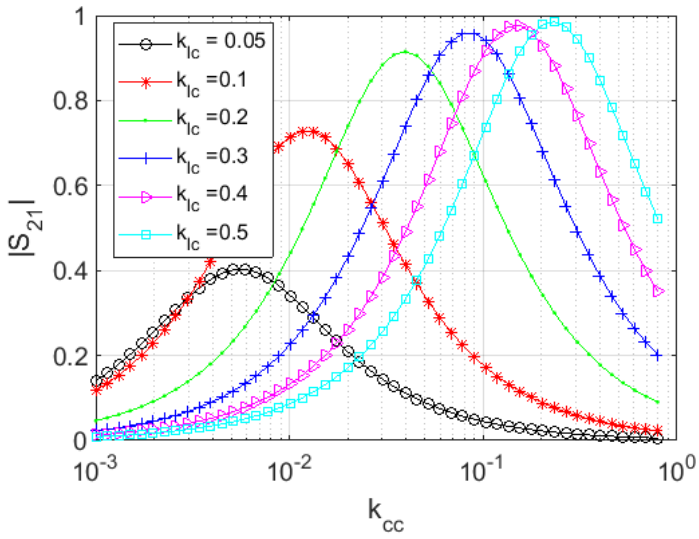

Figure 2.6: Simulated result of how k_{lc} affects $|S21|$ and critical coupling range. (Q_c=300, Q_l=0.9)

adjusting k_{lc} is more effective. Increasing k_{lc} only makes $|S21|_{critical}$ larger but shorter vertical range and vice versa.

2.3 Range of 4-coil System in Planar Dimension

After exploring the parameters that affect the vertical range of a 4-coil system, this section focuses on optimizing the range extension of a 4-coil system in the planar dimension. Furthermore, we will discuss why simply using a larger coil to cover an intended space is not a good solution.

2.3.1 Inefficient Wireless Power Transfer Caused by Large Tx-Rx Size Ratio

Based on the coupling equation, as the distance between transmitter and receiver coil reduces, the coupling between them increases. As the coupling between the two high Q resonators increases, the $|S_{21}|$ at the natural resonant frequency increases until it exceeds the critical coupling point. However, when the size ratio between the transmitter and receiver coil

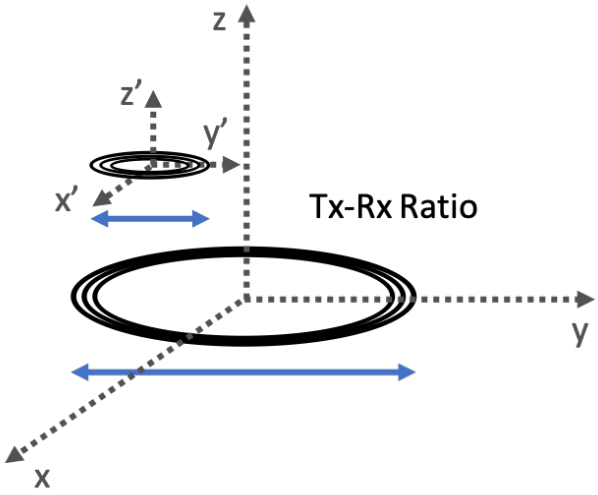

Figure 2.7: Tx-Rx ratio of a 4-coil system.

becomes very large, the coupling between them can still be a very small value even at contact distance. Under this condition, even if the transmitter covers a large area, the power efficiency delivered to the receiver is very limited. Thus, for each receiver geometry, there is a Tx-Rx ratio limit that indicates the maximum transmitter area when efficient wireless power transfer can be achieved. To find the ratio limit, we define a reference coupling value k_{thresh} to assist. The point where the increasing diameter of the transmitter coil causes the coupling with the receiver to become smaller than k_{thresh} is considered as the Tx-Rx ratio limit.

The threshold coupling value k_{thresh} can be found by finding the largest coupling that makes the derivative of the $|S21|$ greater than zero. This condition is shown in Eq. 2.19:

$$\frac{d|S21|}{dk_{23}} > 0 \tag{2.19}$$

Finding the derivative of $|S21|$ in Eq. 2.9 gives:

$$\frac{d|S21|}{dk_{23}} = \frac{2k_{12}k_{34}Q_2Q_3\sqrt{Q_1Q_4}((1+k_{12}^2Q_1Q_2)(1+k_{34}^2Q_3Q_4)-Q_2Q_3k23^2)}{(Q_2Q_3k_{23}^2+(1+k_{12}^2Q_1Q_2)(1+k_{34}^2Q_3Q_4))^2} \tag{2.20}$$

Simplifying Eq. 2.19 and Eq. 2.20 gives:

$$k_{23} < \sqrt{\frac{(Q_1Q_2k_{12}^2+1)(Q_3Q_4k_{34}^2+1)}{Q_2Q_3}} \tag{2.21}$$

Thus, k_{thresh} in Eq. 2.22 is the threshold coupling value that sets the limit of the TX-RX ratio of a 4-coil system.

$$k_{thresh} = \sqrt{\frac{(Q_1Q_2k_{12}^2+1)(Q_3Q_4k_{34}^2+1)}{Q_2Q_3}} \tag{2.22}$$

It should be noted that this k_{thresh} expression is also the $k_{critical}$ of an 4-coil system with asymmetric transmitters and receivers.

The relationships of efficiency as a function of transmitter size simulated with two different receivers are shown in Fig. 2.8 and Fig. 2.9. The three transmitter sizes used in both simulation are the same, which are 16 cm, 28 cm and 40 cm in diameter. The coil parameters Q_c, Q_l and k_{lc} of the three transmitters are 312, 1.14 and 0.28 respectively. They are chosen to be the same to highlight the effect of coupling change with asymmetric Tx-Rx size ratio on $|S21|$ while isolating the impact of the other parameters. The receiver in Fig. 2.8 is 5.6 cm in diameter and the one in Fig. 2.9 is 2 cm in diameter. The plots show that for each receiver, when the Tx-Rx ratio exceeds a threshold, the maximum achievable efficiency with that ratio drops dramatically, regardless of how small the Tx-Rx separation is. The experimental results in [43] also show the same conclusion. In addition, the different Tx-Rx ratio limits of the two plots indicate that the Tx-Rx ratio limit is different for different receivers.

In summary, we have shown that, due to efficiency limits, one cannot choose a single large coil to cover an arbitrarily large area. As the Tx-Rx ratio becomes larger, the maximum coupling of the 4-coil system reduces. The maximum Tx-Rx ratio is different for different receivers. For efficiency consideration, the maximum Tx-Rx ratio for a given receiver is defined when the maximum achievable coil-coil coupling k_{23} is equal to a newly defined parameter k_{thresh}.

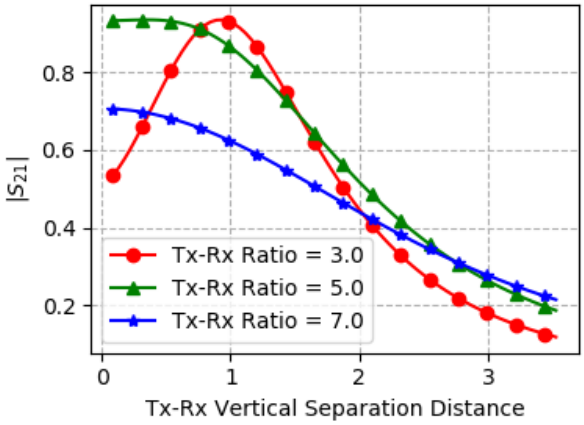

Figure 2.8: Simulated result of $|S21|$ with change of Tx-Rx Size Ratio. Receiver size is 5.6 cm in diameter. Tx-Rx vertical separation distance is normalized to the diameter of the receiver.

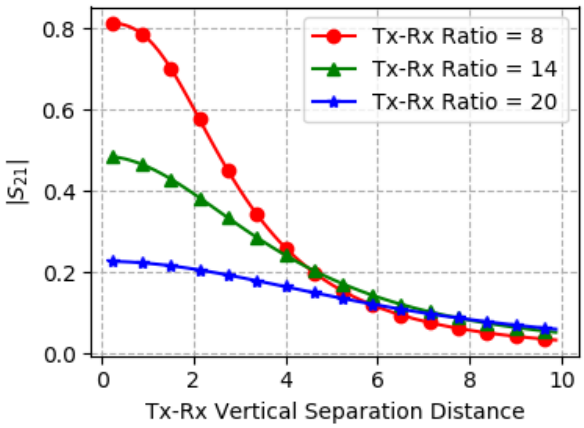

Figure 2.9: Simulated result of $|S21|$ with change of Tx-Rx Size Ratio. Receiver size is 2 cm in diameter. Tx-Rx vertical separation distance is normalized to the diameter of the receiver.

2.4 Range Extension with Rectangular Coils for Moving Receivers

Wireless power transfer systems have conventionally been modeled and optimized in static configurations, with immobile receivers and transmitters. However, many real-world use cases are not well addressed by this simplified model. For example, to charge sensors placed on a conveyor belt (Fig. 2.10), it is most convenient to charge the sensors while they are moving on the belt instead of manually removing them to a dedicated charging station.

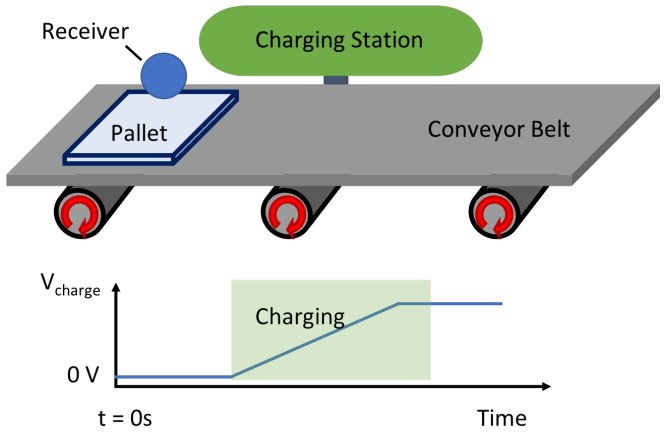

Figure 2.10: A moving receiver on a conveyor belt is wirelessly charged via magnetic resonance.

Based on the results from the previous section (Section 2.3) and in [43], the largest area of efficient wireless power transfer coverage is approximately 5 times the receiver diameter if we use the same receiver and a circular shaped coil for transmitter. When this receiver has a known path that moves on a straight line, the longest path this receiver can be charged when passing the transmitter is 5 times its diameter. The rest of the circular area is wasted if no receiver passes by.

To solve this problem, this section focuses on exploring the design of the transmitter coil shape to extend the range along the direction of motion, to prolong the charging time of the moving receiver. The optimal design is based on the velocity of the receiver, energy required

by the load, Tx-Rx distance, and maximum receiver size. We provide simplified equations for modeling the optimization, and implement and characterize hardware based on the design.

2.4.1 Optimal Coil Geometry Design

The purpose of this section is to provide the design steps and equations used to determine the optimal transmitter geometry for moving receiver applications. Particularly, when the motion of the receiver is predictable rather than random. In this application, we limit ourselves to the following constraints:

- A maximum receiver size
- Energy the receiver must accumulate
- Path of the receiver's motion
- Speed of the receiver's motion
- Maximum allowable transmit power

In this section, we will answer the question of finding the optimal coil width and length given these constraints. Traditional wireless power transfer systems choose coil shapes based on the available space which optimize the quality factor (Q). Though we have shown in the previous section that when the receiver size is fixed but transmitter coil does not have a size constraint, simply optimizing quality factor of the transmit coil does not necessarily result in the optimal efficiency. The resulting coupling between the transmitter and receiver plays a significant role. In this section, our exploration focuses on the design of the transmitter coil that is optimal for both Q and k in the context of a moving receiver application with a known straight path.

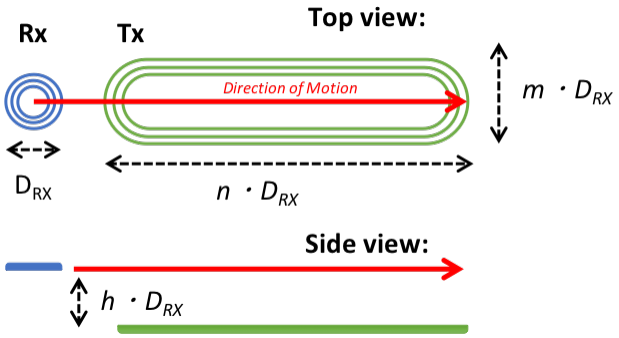

Figure 2.11: Illustration of the dimensional parameters of the transmitter and receiver of the rectangular coil designed for a moving application.

Modeling and Analysis

We have defined a term called transmission factor F_{TX} to represent how efficient and long the transmit coil needs to be. It is calculated in Eq. 2.23, where E is the total amount of energy needed by the receiver, v is the velocity of the moving receiver, P_{TX} is the transmitted power and D_{RX} is the diameter of the receiver.

$$F_{TX} = \frac{E \cdot v}{P_{TX} \cdot D_{RX}} \tag{2.23}$$

To design the optimal dimension, first calculate the transmission factor F_{TX} in Eq. 2.23 based on the application requirements. Next, find the transmitter dimension (n, m) defined in Fig. 2.11 that agrees with Eq. 2.24, while maximizing η.

$$\eta(n, m) \cdot n = F_{TX} \tag{2.24}$$

where η is the WPT efficiency, and n is the size ratio between the longer dimension of the transmitter coil and D_{RX}.

The efficiency η of the coil system is represented by $|S21|^2$ with the assumption of the source and load impedances being matched. We also assume the cross couplings between the loops and the non-adjacent coils are small enough to be ignored [32]. The $|S21|$ of a 4-coil

system can be obtained with Eq. 2.9 through circuit model analysis and is represented again in Eq. 2.25 below.

$$|S21|_{asymmetric}= \frac{2k_{12}k_{23}k_{34}Q_2Q_3\sqrt{Q_1Q_4}}{(Q_1Q_2k_{12}^2+1)(Q_3Q_4k_{34}^2+1)+Q_2Q_3k_{23}^2} \tag{2.25}$$

In Eq. 2.25, subscript 1, 2, 3 and 4 represent transmitter loop, transmitter coil, receiver coil and receiver loop, respectively. Because the problem assumes a fixed size receiver and varying transmitter size, we can assume Q_1, Q_3, Q_4, k_{12}, k_{34} are constant, and the quality factor of the transmitter coil Q_2 and the coupling between transmitter coil and receiver coil k_{23} are changing variables.

The coupling k between two asymmetric rectangular coils can be found using the known expression for the mutual inductance between two rectangular coils in Eq. 2.26 and Eq. 2.27 [12].

$$k_{ij} = \frac{M_{ij}}{\sqrt{L_iL_j}} \tag{2.26}$$

$$M = 2[H(\frac{nD_{RX}}{2}, \frac{mD_{RX}}{2}, \frac{D_{RX}}{2}, \frac{D_{RX}}{2}, hD_{RX}) + H(\frac{mD_{RX}}{2}, \frac{nD_{RX}}{2}, \frac{D_{RX}}{2}, \frac{D_{RX}}{2}, hD_{RX})] \tag{2.27}$$

The function H is calculated in Eq. 2.28 based on Biot-Savart law [12]. The assumption of this law is that the two coils are co-axial. Even though the flux distribution is not uniform across the horizontal plane, we make the assumption that the flux value is constant across the moving path, and the results of the prototype evaluation in the later-on section show that this assumption is valid.

$$\begin{aligned} H(a,b,c,d,z) = \frac{\mu_0}{2\pi}\Bigg[& \sqrt{(b+d)^2+z^2+(a+c)^2} - (a+c)\cdot \operatorname{arctanh}\frac{a+c}{\sqrt{(b+d)^2+z^2+(a+c)^2}} \\ & - \sqrt{(b+d)^2+z^2+(a-c)^2} + (a-c)\cdot \operatorname{arctanh}\frac{a-c}{\sqrt{(b+d)^2+z^2+(a-c)^2}} \\ & - \sqrt{(b-d)^2+z^2+(a+c)^2} + (a+c)\cdot \operatorname{arctanh}\frac{a+c}{\sqrt{(b-d)^2+z^2+(a+c)^2}} \\ & + \sqrt{(b-d)^2+z^2+(a-c)^2} - (a-c)\cdot \operatorname{arctanh}\frac{a-c}{\sqrt{(b-d)^2+z^2+(a-c)^2}}\Bigg] \end{aligned} \tag{2.28}$$

The other factor that changes with the varying coil dimension is the quality factor:

$$Q = \frac{\omega L}{R} \tag{2.29}$$

The inductance of a single turn square loop is calculated in Eq. 2.30. The assumption is that the width w and the length l of the loop are much larger than the radius of the wire r [29].

$$\begin{aligned} L_{loop} = \frac{\mu_0 \mu_r}{\pi} \Bigg[& - l \cdot \ln\left(\frac{l + \sqrt{l^2 + w^2}}{w}\right) - w \cdot \ln\left(\frac{w + \sqrt{l^2 + w^2}}{l}\right) \\ & + l \ln\frac{2l}{r} + w \ln\frac{2w}{r} + 2\sqrt{l^2 + w^2} - 2w - 2l \Bigg] \end{aligned} \tag{2.30}$$

The resistance formula is the AC resistance approximation based on Kaiser[21], where δ represents the skin depth of the loop material, l is the length of the wire and σ is the conductivity of the wire.

$$R_{loop} = R_{dc} \cdot \frac{r}{2\delta},\ R_{dc} = \frac{l}{\sigma \pi r^2},\ \delta = \sqrt{\frac{1}{\pi f \sigma \mu}} \tag{2.31}$$

Computational Results for Rectangular Coil Transmitter

This section summarizes the feature of $|S21|$ (Fig. 2.12) and F_{TX} (Fig. 2.13) with different coil geometry in terms of (n, m, h). The k_{23} and Q_2 are computed with Eq. 2.26 and Eq. 2.29 with different transmitter coil dimensions represented in terms of (n, m). The rest of the parameters use fixed values based on previous literature. The geometry with the smallest (n, m) set that results in the required F_{TX} is optimal for the application on charging time and cost.

The result shows that when the transmitter and receiver are closely spaced or over-coupled, having the longer coil ($n > 10$) with narrower width ($m \leq 2$) is the optimal choice because the $S21$ increases as the width n becomes larger. When they are critically coupled, choosing $m = 2$ is the best and the optimal n is based on the required F_{TX} because the $|S21|$ stays near optimal across the largest range of n. As the coils become more and more under coupled, the m dimension need to increase to give the better efficiency over the longest

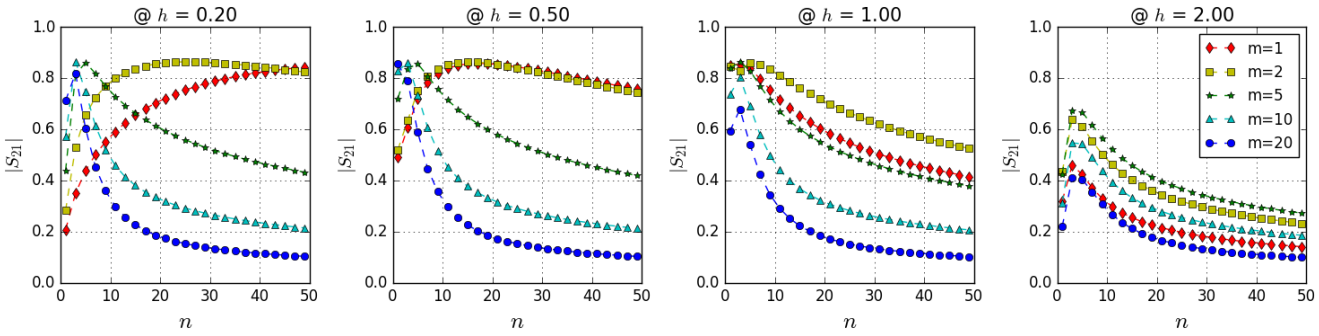

Figure 2.12: Result based on circuit model analysis of $|S21|$ between loop with dimensions n by m and loop with dimension 1 by 1 for four different separation distances. n, m, and h are Tx length, width, and Tx-Rx separation ratios with respect to D_{Rx} defined in Fig. 2.11. $Q_1, Q_3, Q_4, k_{12}, k_{34}$ used in the computation are 0.7, 150, 0.5, 0.1 and 0.3, respectively, which are taken from prior literature [43, 32].

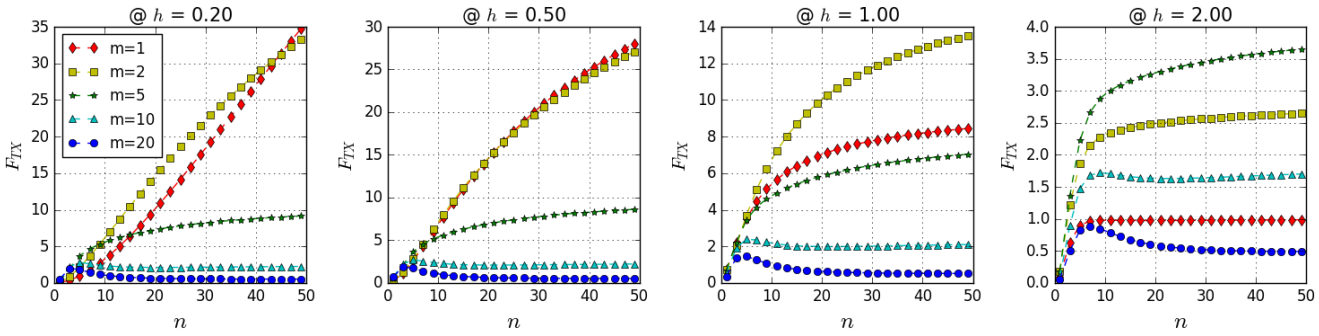

Figure 2.13: Result of F_{TX} calculated with Eq. 2.24 between the loop with n by m dimension and the loop with 1 by 1 dimension with four different separation distances. The efficiency η is the square of $|S21|$ in Fig. 2.12

range. The examples of optimal geometry given specific input conditions are listed in Table 2.1.

Table 2.1: Examples of Optimal Geometry

Input Parameters	**Case 1**	**Case 2**	**Case 3**
$E\ (J)$	30	30	30
$v\ (m/s)$	0.2	0.2	0.2
$P_{TX}\ (W)$	20	20	10
$D_{RX}\ (cm)$	4	4	4
h	1	0.5	1
Optimal Geometry	**Value**	**Value**	**Value**
m	2	2	2
n	10	20	30

Even though the model uses only a single turn loop for simplicity, the same relationship applies to the multi-turn coil. However, in order to obtain the precise optimal dimensions for a multi-turn coil system, one should adjust the formulas for mutual inductance, inductance, and resistance of the multi-turn system for better accuracy, which can be easily modeled using superposition. In addition, the increase in parasitic capacitance with more turns needs to be considered, because it could result in a low self-resonant frequency that limits the quality factor.

2.4.2 Experiments and Results

To emulate wirelessly charging sensors on a conveyor belt, we use a model train moving at about 0.2 m/s to carry the wireless charging receiver and the sensor load. The sensor load consumes 1 mW, and the allowable Rx size is 4.5 cm x 4.5 cm. The target separation distance between Tx and Rx is 0 to 8 cm. Given this spec, we have designed an Rx coil with 4.5 cm diameter and Tx coil size of 48.5 cm x 10 cm which makes the Tx-Rx ratio $n = 10.8$ and

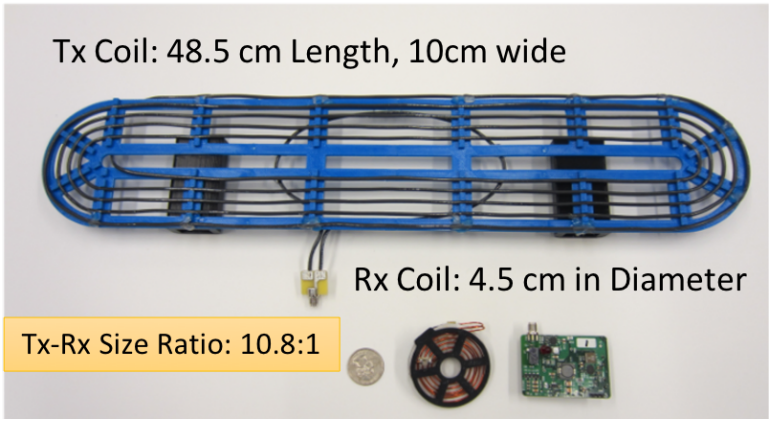

Figure 2.14: Transmitter coil (48.5 cm by 10 cm), receiver coil (6 cm by 6 cm) and the wireless charging receiver.

$m = 2.2$ (Fig. 2.14). This Tx dimension gives the optimal efficiency when the separation distance is between 1 cm to 5 cm, according to the analysis shown in Fig. 2.12.

Coil Efficiency Result

Fig. 2.15 shows the $|S21|$ with various receiver locations. Fig. 2.15-a,b show the results when the Tx-Rx distance is 3 cm, which is slightly over coupled. In Fig. 2.15-a, the receiver moves along the center line of the transmitter. It shows the efficiencies under such condition are mostly constant along the path. This agrees with the assumption that we can use the mutual inductance equation Eq. 2.27 that is modeled for the co-axial condition to estimate the mutual inductance when the receiver is moving along the center line of the transmitter under slightly over coupled condition. When the receiver is under coupled with 5 cm Tx-Rx distance (Fig. 2.15-c,d), the efficiencies become less constant because the flux along the path is less uniform. In addition, when the Rx moves off the center line of the Tx (Fig. 2.15-b,d), the efficiencies become worse than that along the center line dut to uniform flux distribution.

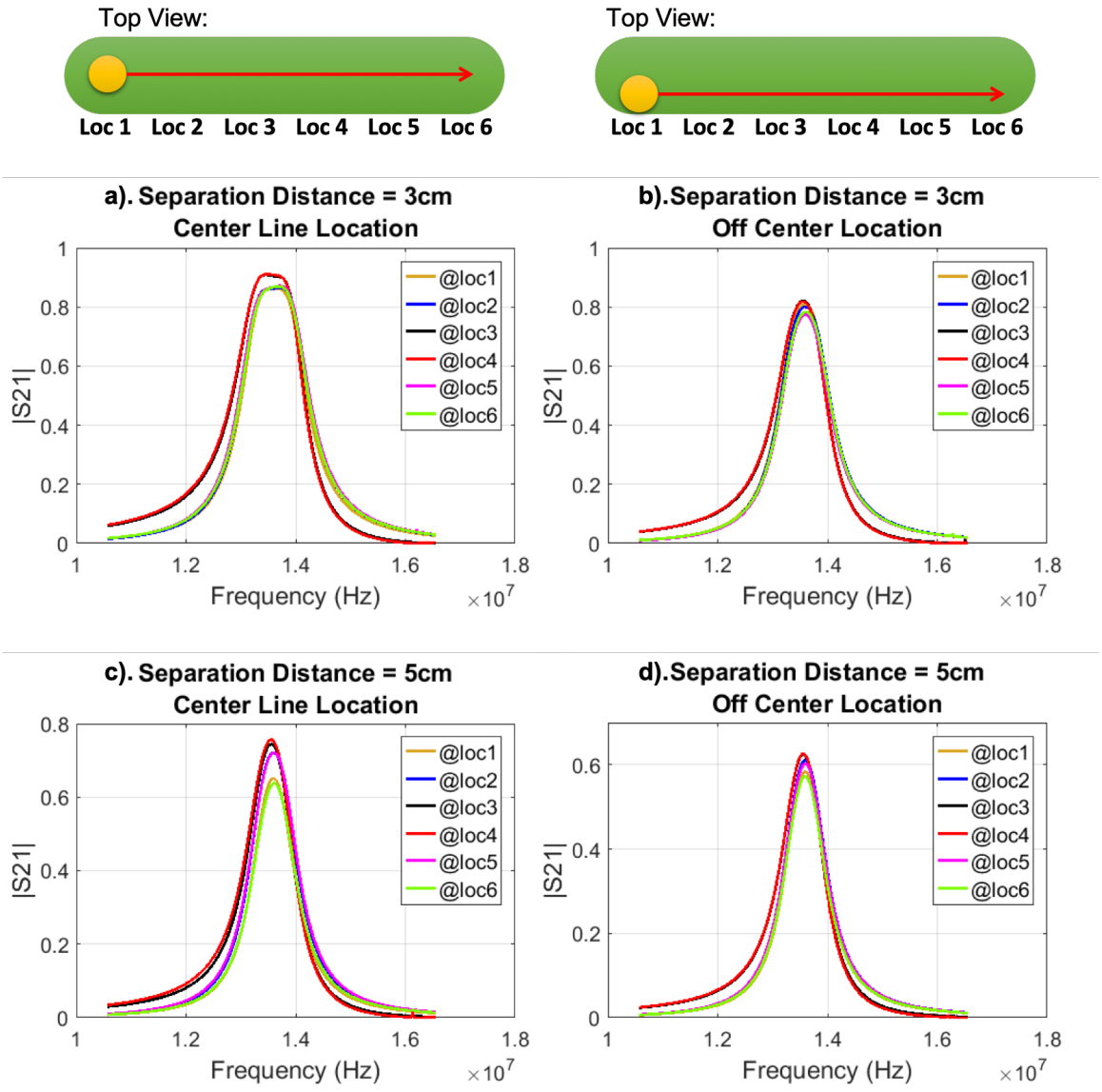

Figure 2.15: Measurement result of $|S21|$ between transmitter and receiver coil with 4 cm (a and b) and 8 cm (c and d) vertical separation distance along center line of the transmitter (a and c) and off the center line (b and d).

Receiver Hardware Result

For a moving receiver, the energy storage device needs to be charged rapidly in a short time. In this system, a 2.5 F supercapacitor bank rated for 5.4 V was used to store energy. The

5.4 V rating was selected in order to provide sufficient headroom to operate a 3.7 V linear regulator.

The receiver is in active mode when the voltage of the supercapacitor exceeds 4 V, providing a regulated output to the load. When supercapacitor voltage drops below 4 V, the receiver enters a sleep mode and ceases to provide power to the load to preserve energy.

With a wireless power transmitter from Wibotic set to transmit 20 Watts, we can fully charge the receiver in 18 seconds, allowing the 1mW sensor to run for 1.5 hours before it returns to sleep mode. After this initial cold start, it only takes 2.5 seconds to charge it back to active mode. Because the leakage of the supercapacitor is small in the sleep mode, it takes weeks for the voltage of supercapacitor to drop below 2V. Thus, the average charging time required to switch from sleep mode to active mode is under 2.5 seconds if the receiver is charged at least once per day.

2.4.3 Conclusions

This section described a method of designing transmitter coil geometries for wireless charging applications in which the receiver is moving. We provide simplified equations and procedures to optimize the design. We implement and characterize wireless power transfer coils and a wireless charging receiver that demonstrates the suitability of long rectangular transmitters for charging receivers moving in a straight line.

Chapter 3

RANGE EXTENSION WITH 1D ARRAY OF COUPLED RESONATORS

The term relay resonator refers to a passive resonator that is neither physically connected to a power source nor to a load, but is placed between the two to extend the range of the power transfer. To ensure that this resonator acts as a power relaying device, its self resonant frequency has to match with the frequency of the resonant field [47]. For use in a wireless power transfer system, a relay resonator can be constructed with a spiral coil and capacitor in series [48]. In this chapter, we talk about the range extension ability of an array of coupled resonators (relay coils) in one-dimension.

Conventionally relays are studied in the form of axial arrangements. The wireless power transfer range can be extended by inserting one or more relays at the right location on a straight line or a curved line [50]. But with the axial arrangement, when the receiver moves, the relays have to be physically moved to continue guiding the power. A more practical arrangement is coplanar relays because it gives the receiver freedom of motion near the surface. However, the power received along the path is very not uniform. This phenomenon is caused by the interference between the relay coils. This interference results in multiple resonant modes which vary at different locations along the path. The multiple resonant modes can shift the best pass band away from the resonant frequency that each resonator is tuned to, which results in inefficient power delivery with a single fixed operation frequency. One can think of this phenomenon as the over coupling region of a 4-coil system, where there are two frequency bands that can both deliver power efficiently but neither is the natural resonant frequency of the resonators [32].

This chapter explores and characterizes this phenomenon of multiple resonant modes

caused by a group of coupled relay resonators in 1D. We identify methods of delivering power with different arrangements of 1D relays. More specifically the methods are split into two categories: using relays at the non-natural resonant frequency, and using relays at their natural resonant frequency. By analyzing the condition when the receiver is over coupled to the relay array, we introduce a new method of improving efficiency with correcting the arrangement of relays. We call this technique *spatial tuning* [36].

3.1 Background on Wireless Power Transfer with Relay Resonators

Since magnetic resonance wireless power transfer operates at near field, the decay of efficiency is proportional to $1/r^3$ which is faster than that in far field with $1/r^2$. The term r represents the distance away from the transmitter coil. Such a near field operation limits the mobility of the receiver, assuming that the transmitter is static. Researchers have studied different ways of using relay resonators to extend the wireless power transfer range. Zhong et al. demonstrated that relays can be placed on a curved coaxial path to guide power transfer [50]. Wang et al. has analyzed that planar relays also guide power along the path [40]. On the other hand, Waters et al. and Ghovanloo et al. have developed phase array system to extend transfer range. In these cases, each coil of the phases array system is connected to a RF power source. The added control gives more degree of freedom on the direction and shape of the generated field, with the trade-off in system complexity and cost [25, 44].

3.2 Resonant Modes of 1D Relay Array with Loose Coupling

3.2.1 Relay Under Test

Different number and alignment of coupled resonators create different resonant modes [19]. So when a receiver is moving along a path of linearly arranged 1D relay array, we expect to observe the change of resonant modes as a function of receiver locations. To better extract the feature of relays, we design a series of experiments that collects the frequency response as a receiver moves along a group of relays. Two relay configurations are compared: **edge-**

driven, and **middle-driven**. Figure 3.1 shows the two different configurations. Edge-driven relay refers to the relay configuration where the primary relay coil is on the edge of the 1D linearly arranged relay path. Primary relay coil is the relay coil that has the strongest coupling with the driven loop that it is in parallel with it. Middle-driven relay refers to the relay configuration when the primary relay coil is at the center of the linear relay array, which divides the rest of relays into two linear paths with equal number of hops. Each divided linear path is referred as a **leg**.

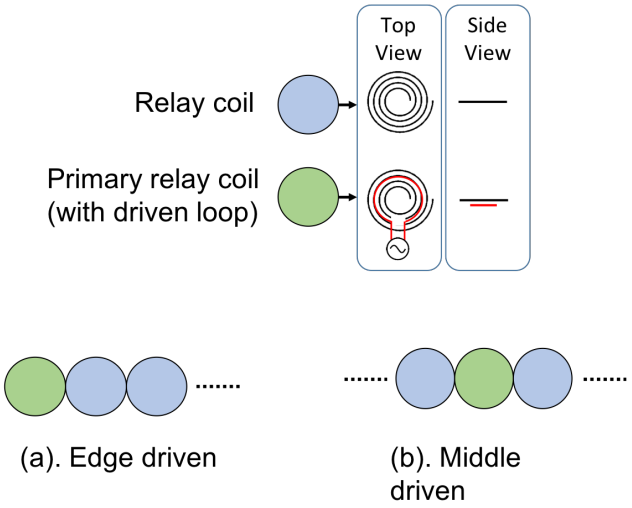

Figure 3.1: Illustration of two methods of driving 1D relay array with the same number of coils. The green circle represents the driven loop and the primary relay coil, and the blue circle represents a passive relay. a) represents the edge-driven setup, with which the transmitter drives the array at the edge. b) represents the middle-driven setup, with which the transmitter drives from the middle.

While edge-driven setup is popularly studied, the other driven methods is rarely presented. The motivation to have middle-driven relays in this study is to better understand the impact of relays when they are not directly on the power path. Even when the relays are not in between the transmitter and receiver, their existence can still change the overall

resonant mode. Middle-driven configuration is a special case with having the same number of hops in each leg. We choose the symmetric structure so that we can expect the change in resonant modes along each leg should also be the same.

Since the goal of Section 3.2 is to characterize the resonant modes that is only caused by having multiple relays in the system, we want to exclude the over coupling effect. To do so, we use coil placement that ensures **loose coupling** between each relay coil and receiver coil. This means that the coupling between each coil will not exceed the critical coupling of their equivalent 4-coil system.

To ensure the relays in the tests are identical and have the same coupling relationship, the relay test platform is implemented with a hexagonal tessellated sheet of identical planar coils on a printed circuit board. The coils are designed based on the work from [42]. Each coil has a tuning capacitor in series to tune its resonant frequency at 13.56 MHz. A mechanical switch is also connected in series so that each relay can be enabled or disabled independently to form the intended relay configuration tests.

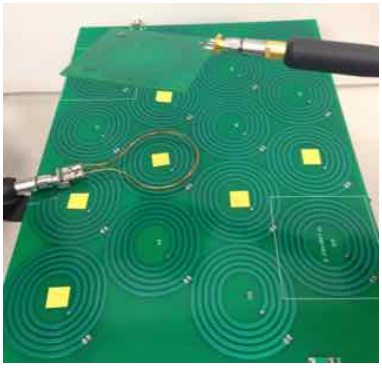

Figure 3.2: Experimental setup used for all tests in this section. The planar relay array is constructed with a 4-layer PCB. Each coil has a tuning capacitor and mechanical switch to enable/disable the resonance of each coil. The receiver has a loop-coil structure.

3.2.2 Resonant Modes in Frequency Spectrum

Experiments are performed for both middle-driven and edge-driven configurations with 1-hop, 2-hop, and 3-hop using the planar relay array shown in Figure 3.2. The number of hops represents the number of relays in one leg. We form these configurations under tests with the control of the mechanical switches. Both the experiment setup illustration and result are shown in Figure 3.3. The receiver is placed above the relay path at locations with marked number, at a fixed separation of 37 mm parallel to the relay plane. This distance is the measured critical coupling distance between the receiver and the transmitter with zero hop.

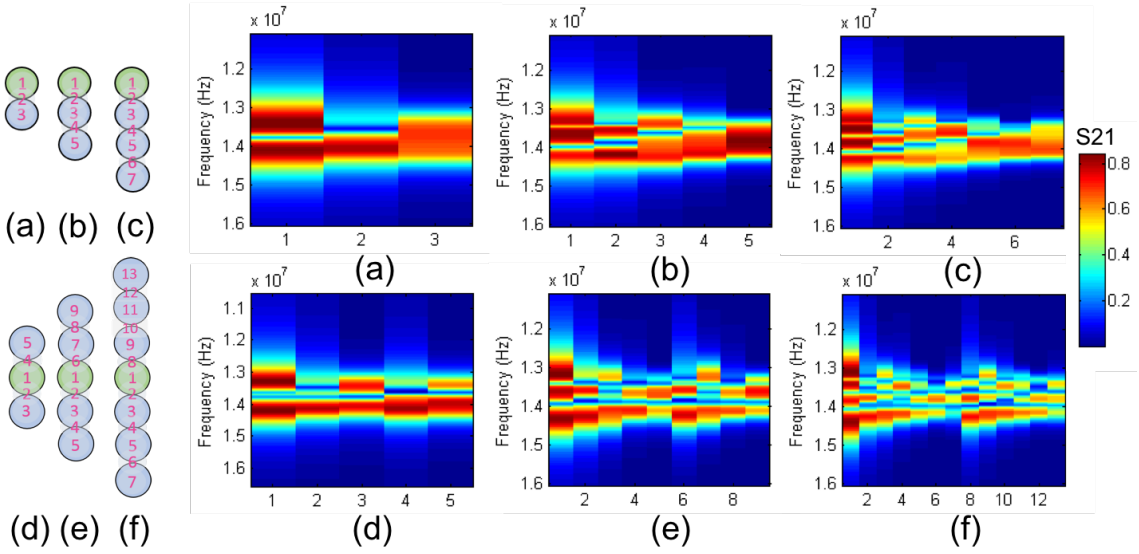

Figure 3.3: a), b), and c) are edge-driven 1-hop, 2-hop and 3-hop configurations, respectively. d), e), and f) are middle-driven 1-hop, 2-hop and 3-hop configurations. g) and h) are relay sheet configurations used as points of comparison. S21 response across a frequency range along the relay path is determined for each configuration. In each test, the receiver is moved on top of each labeled location in parallel with the transmitter plane for a separation distance of 37 mm.

Figure 3.3 shows the bandwidth with both type of configurations becomes narrower as

the receiver moves further down the path away from the primary relay location.

For the edge-driven case (Figure 3.3a-c), the number of resonant modes is the highest at the primary location, which is proportional to the number of hops of the configuration. As the receiver moves down the path, the frequency of the peak of each resonant mode shifts. The natural frequency of the relays overlaps with the peak frequency at some locations and nulls at other locations. When the receiver moves to the last hop, the resonant mode reduces to one and it includes the natural resonant frequency.

On the other hand, the middle-driven case shows the loading effect of relays on non-power paths. Figure 3.3d-f shows that for each configuration, there is at least one null of the resonant modes with similar frequency is shared among all the locations. This pushes one of the resonant modes next to the null having similar frequency among different locations as well. Hence, the resonant modes at the end hop of middle-driven configurations is more than one.

3.2.3 Maximized Power Transfer with Optimal Frequency

A metric for comparison of power delivery coverage is developed for the different relay coil configurations. Due to regulations, a wireless power system will be constrained to operation at a single frequency. Therefore, simple comparison of S21 maximums (which shift as a function of receiver position) are not effective as a metric. However, we also note that any relay coil configuration can be tuned to operate in a desired frequency band, and therefore that the absolute frequency values observed in these results are of little importance.

The metric we propose below addresses these observations by first identifying the optimal frequency of operation for each configuration based on a coil efficiency, and then by comparing across configurations (assuming that the optimal frequency would be used for each, but that frequency cannot be allowed to change between receiver positions):

- **Metric:** To evaluate a particular relay coil configuration at a particular separation distance: for each test frequency, count the number of equally-spaced locations across the

test volume where the power efficiency exceeds 50% (S21 value is greater than approximately 0.7). Then, find the peak value of this count across all frequencies. This peak represents the *best possible single-frequency coverage for each relay coil configuration.*

The efficiency threshold of 50% was selected as a reasonably acceptable efficiency for many applications. Figure 3.4a-3.4c compare the coverage between the optimal frequency mode (top) and the natural frequency mode (bottom). Natural frequency mode operates at the frequency at which each coil would resonate if it were independently tested. Figure 3.4d-3.4f compare the performance of the three configurations based on the computed results from the metric at the critical coupled region 4cm. The frequency which has the most number of locations with $S21 > 0.7$ is selected for use in the optimal frequency mode for the corresponding relay configuration.

The bar plot in Figure 3.4 shows that optimal frequency mode is always better than the natural frequency mode, and the 2-leg-2-hop has better coverage than the other two configurations. Moreover, the five-coil middle-driven relay geometry provides a 43% coverage improvement over a five-coil edge-driven geometry. However, for the natural frequency mode, there is always a null spot after the good coupling locations (3.4a-3.4c). The pattern of high followed by low repeats with a decaying envelope as the location is increasingly distant from the driven coil.

To further illustrate the advantages of using optimal frequency method, Figure 3.5 directly compares the S21 achieved to the other two methods: natural frequency mode and frequency tracking mode. Frequency tracking mode is a post processing step that picks the largest S21 at each receiver location across the whole tested frequency spectrum, which represents the optimal result. Since it requires changing the operating frequency adaptively, it is not practical and is only used as an analysis reference. The result shows significant efficiency improvement with the optimal frequency mode over the natural frequency mode. Moreover, the optimal frequency method can maximize the achievable efficiency.

In summary, this section characterizes the pattern of the resonant modes of 1D relay array,

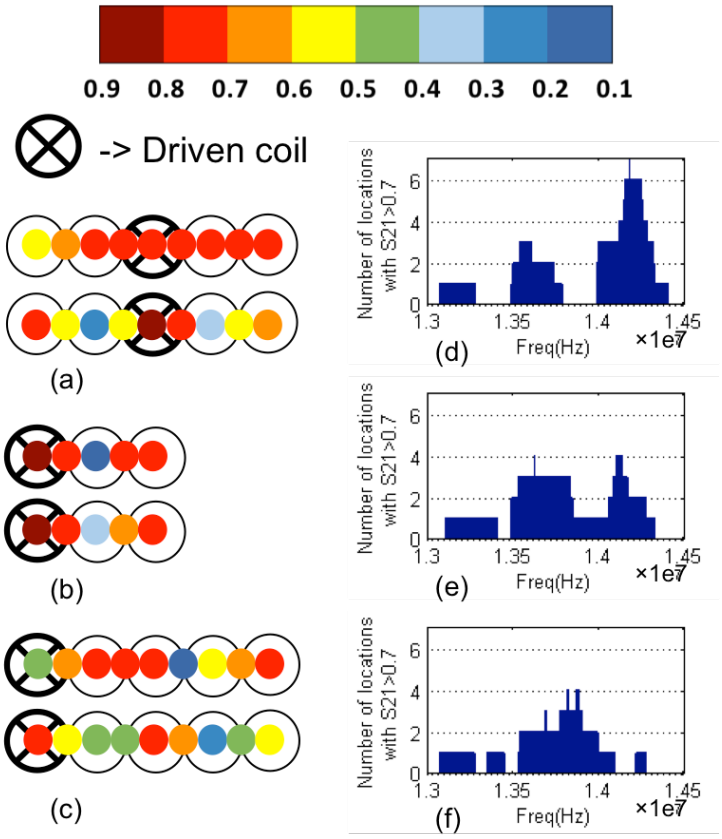

Figure 3.4: Comparing the 2-leg-2-hop a), 1-leg-2-hop b) and 1-leg-4-hop c) using the metric defined in Section 3.2.3. Figure d) e) and f) show the results of configuration a)-c) with 4cm separation distance (critical coupled) based on the metric. The color map of the top figures of a), b) and c) illustrates the S21 values at the optimal frequency based on result d)-f); the bottom figures of a)-c) shows the S21 at the natural frequency 13.56MHz based on result d)-f). The optimal frequencies used for these three configurations are 14.2MHz, 14.1MHz and 13.8MHz,respectively.

and studies the impact of relays when they are not on the shortest path between transmitter and receiver. In conclusion, using optimal frequency method which chooses operating frequency that is not the natural resonant frequency with middle-driven configuration can enable the largest coverage area with optimal average efficiency. The studies and conclusion

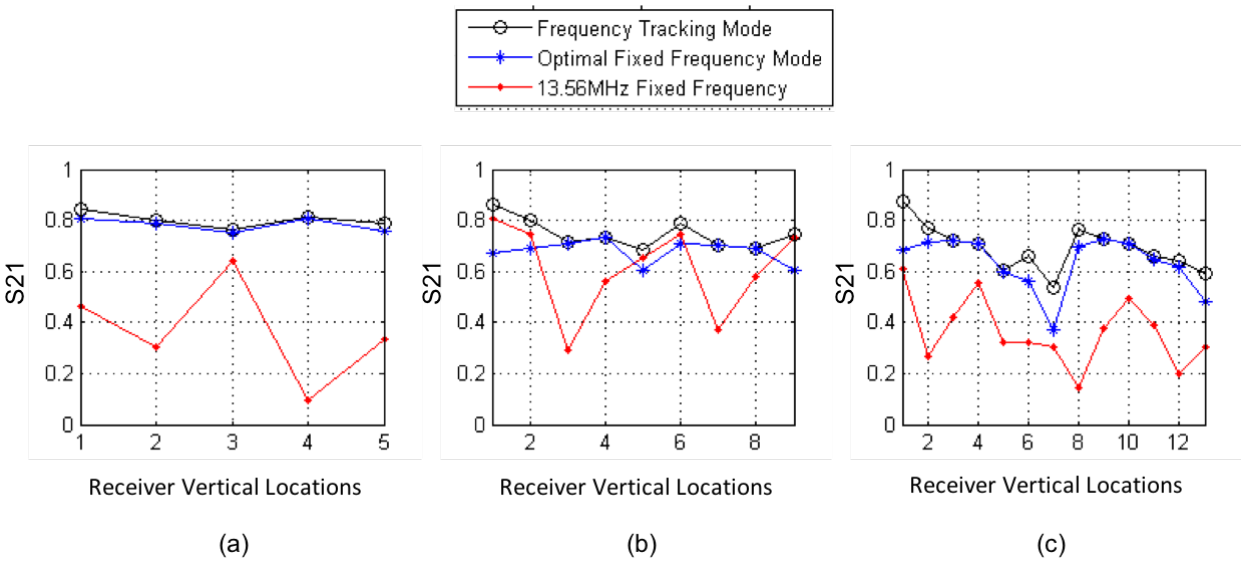

Figure 3.5: Comparing optimal fixed frequency mode with frequency tracking and default synchronously tuned frequency modes. a), b) and c) are results for 2-leg-1-hop, 2-leg-2-hop and 2-leg-3-hop, respectively (configurations are shown in Figure 3.3d-3.3f). The optimal fixed frequency mode is the proposed one in this work.

are for relay system of which the relays and receiver are loosely coupled. Next section will characterize the system when the receiver is over coupled to the relay system, and methods for improving efficiency accordingly.

3.3 Spatial Tuning with Relay Resonators at Tight Coupling

Previous section (Section 3.2) characterize the relay system under loosely coupled condition. This section first describes the difference in the over coupled condition and then introduces a method to improve efficiency called spatial tuning.

3.3.1 Operation at the over coupled region

n the conventional single transmitter-receiver system, improving transmission efficiency when the receiver is in the over coupled region can only be done through frequency tracking and active impedance matching [32]. Fortunately, the multi-relay system offers one more degree of freedom which it can change the coupling between the transmitter and receiver by altering the locations of the active relays. We can select a relay coil path which produces the desired amount of coupling, avoiding the over coupled region in favor of critical coupling and thereby eliminating the need for frequency tracking and active impedance matching.

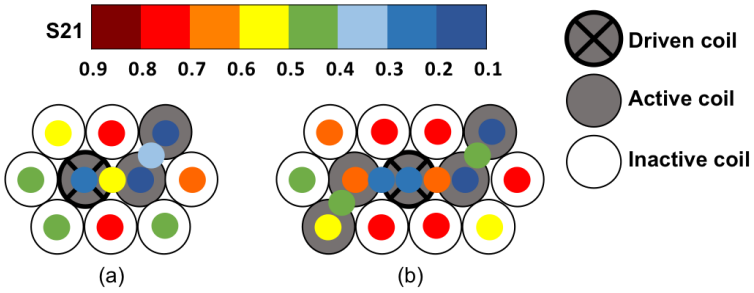

Figure 3.6: Compare the S21 at locations that are not directly above the relay path when the receiver has 1 cm separation distance from the transmitter plane.

Figure 3.6 shows the S21 of the system when the receiver is separated 1 cm away from the transmitter plane. These frequencies are the optimal values obtained for the 4 cm separation case of the 2-leg-2-hop (Figure 3.4d) and 1-leg-2-hop (Figure 3.4e) configurations, respectively. The coil colored in gray highlights the active relay path, and the smaller colored circle represents the S21 value when the receiver is at the corresponding location. The result agrees with the assumption that using relays directly under the receiver does not return a good S21 with the closely coupled condition. For easier reference, the location that is directly under the receiver is called the receiver shadow. The S21 is better when the enabled relays surround the receiver shadow, or connect the receiver shadow with the fewest number of hops excluding the receiver shadow.

3.3.2 Performance with various separation distance, with comparison to single driven coil

The performance of the proposed middle-driven relay coil system is also studied in the over coupled region and under-coupled region by changing the separation distance between the receiver and the plane of the relay array. Distance is varied from 1 cm to 6 cm, in 1 cm increments. The relay configurations chosen for this test are 2-leg-2-hop, 1-leg-2-hop and 1-leg-4-hop (Figure 3.4a-3.4c), and they are tested with the metric value.

When the separation distance between the receiver and the transmitter plane is very small, only locations that are directly above or very close to the driven coil have good coupling, though these resonant modes are pushed further away from the natural frequency. As a result, the number of locations that has S21 greater than 0.7 is much less than those in the critical coupled region (Figure 3.7). When the receiver is in the under coupled region, the edge-driven configuration decays slower comparing to the middle-driven setup, which is probably due to the fewer resonant modes.

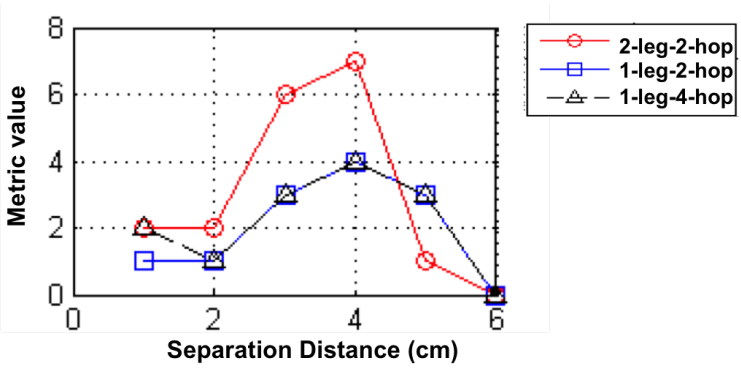

Figure 3.7: Compares the best metric value at separation distance 1 cm to 6 cm with 1 cm increment for the three configurations.

From Section 3.2.2 on analyzing frequency response of the relay resonators, we have concluded that using optimal frequency method with middle driven relay configuration can enable the largest coverage area and deliver optimal WPT efficiency. However, if we have the flexibility of enabling any sets of relay coils on a 2D planar array, the added freedom of

array can tune the coupling between the driven loop and receiver coil by activating the best set of relays. We call the tuning method by enabling and disabling specific relays to optimize S21 as spatial tuning.

To best perform spatial tuning on a 2D array of relay resonator, the transmitter has to have the knowledge of the receiver location, therefore, to provide the best configuration solution. In addition, being able to enable and disable each relay separately is important. The details will be discussed in the Chapter 5.

3.3.3 Conclusion

In order to deliver wireless power with good efficiency over a large area, using 1D array of relays with different arrangements is characterized. Different configurations of activated relay sets are studied, and the middle-driven relay geometry with the single optimal frequency mode is observed to have the best coverage area when compared to the edge-driven configuration. When the receiver has a very tight coupling with the relay array plane, the efficiency decreases. Use spatial tuning that changes the enabled relays can re-tune the coupling and optimize efficiency.

3.4 Extending Range with Relays at Natural Resonant Frequency

Previous sections of this chapter analyze the characteristics of coupled relay resonator system at different frequencies. We have identified that the use of middle-driven and optimal frequency method for optimizing coverage and efficiency. While this method is great for fixed-area applications, it is hard to be scaled because systems with different number of hops have different optimal frequencies. However, the end hop with edge-driven configuration (defined in Section 3.2.1), always has the optimal S21 at the natural resonant frequency under loose coupling condition. If we assume that each relay resonator is reconfigurable so that we can always use the end hop with edge-driven configuration, the optimal frequency of operation can stay at the natural frequency of each resonator which makes scaling easier.

This section focuses on modeling and optimizing the relay system with edge-driven relay

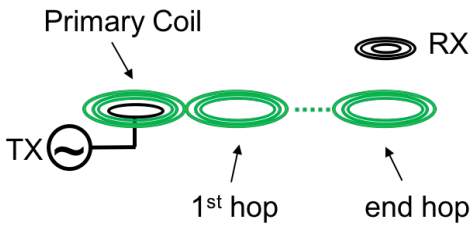

Figure 3.8: A relay system with edge-driven relay configuration and receiver at end hop.

configuration and receiver at the end hop. Figure 3.8 illustrates such system. In this section, we discuss a general model for the edge-driven-end-hop relay networks, which allows us to derive the transmitter-to-receiver transfer function S_{21} of such system. We use this general model to characterize the effect of varying inter-relay coupling on S_{21}, and in doing so we validate a simplifying assumption which will be used in determining how to place the relay coils for optimal coverage. We then develop an expression for the change in end-hop-gain, a proxy for efficiency, as more hops are added to the system. Understanding this incremental reduction in end-hop-gain is helpful in determining how far a relay system can extend power transfer range. This novel mathematical model allows quick and easy computation of this incremental reduction.

3.4.1 General Multi-resonator Network Model

Unlike higher-frequency systems, the frequencies used in magnetic resonance systems have a wavelength much larger than the coils themselves. This makes the quasi-static assumption valid and thus allowing us to use lumped element circuit analysis to model the relay system. We use the coupling relationships between coils of the relay system as part of the circuit model. Coupling is a proxy for coil location, but it is also a highly complex function of many parameters of the system. Because the coupling between relay resonators is based on many factors, the same coupling value can be achieved with many different spacings and angular relationships between coils. Thus, we determine the optimal coupling value between coils but

do not specify an optimal location; coupling provides the most comprehensive and general solution, and can be used to determine the arrangement of resonators (e.g., with specific coil geometries) [1].

Each coil element can be represented with lumped elements R, L and C. The coupling between any two coils i and j is expressed with k_{ij}. Figure 3.9 shows the equivalent circuit model diagram of a n-coil system. Using Kirchhoff's voltage law (KVL), we can derive an equation for each loop. The mutual inductance relates those equations together and form a matrix (Eq.3.1). With solving this matrix, we can obtain the voltage gain to calculate S_{21} of the relay system with Eq.3.3, and Eq3.4.

$$\begin{bmatrix} Vs \\ 0 \\ 0 \\ \vdots \\ 0 \end{bmatrix} = \begin{bmatrix} Z_1 & j\omega M_{12} & j\omega M_{13} & \cdots & j\omega M_{1n} \\ j\omega M_{21} & Z_2 & j\omega M_{23} & \ddots & j\omega M_{2n} \\ j\omega M_{31} & j\omega M_{32} & Z_3 & \ddots & \vdots \\ \vdots & \ddots & \ddots & \ddots & j\omega M_{(n-1)n} \\ j\omega M_{n1} & j\omega M_{n2} & \cdots & j\omega M_n(n-1) & Z_n \end{bmatrix} \begin{bmatrix} I_1 \\ I_2 \\ I_3 \\ \vdots \\ I_n \end{bmatrix} \tag{3.1}$$

$$\begin{aligned} Z_1 &= R_S + R_{p1} + j\omega L_1 + \frac{1}{j\omega C_1} \\ Z_i|_{i\neq n} &= R_{pi} + j\omega L_i + \frac{1}{j\omega C_i} \\ Z_n &= R_L + R_{pn} + j\omega L_n + \frac{1}{j\omega C_n} \end{aligned} \tag{3.2}$$

$$V_L = I_n \times R_L \tag{3.3}$$

$$S_{21} = 2\frac{V_L}{V_S}\sqrt{\frac{R_S}{R_L}} \tag{3.4}$$

For instance, $|S21|$ of the 4-coil system with matched source and load impedance is computed in Eq.2.9.

---

[1] In this section, the optimal coupling is used to implement a planar 1D array, but because of the general purpose nature of coupling as a system parameter this result could also be applied to a relay system in any 3D arrangement

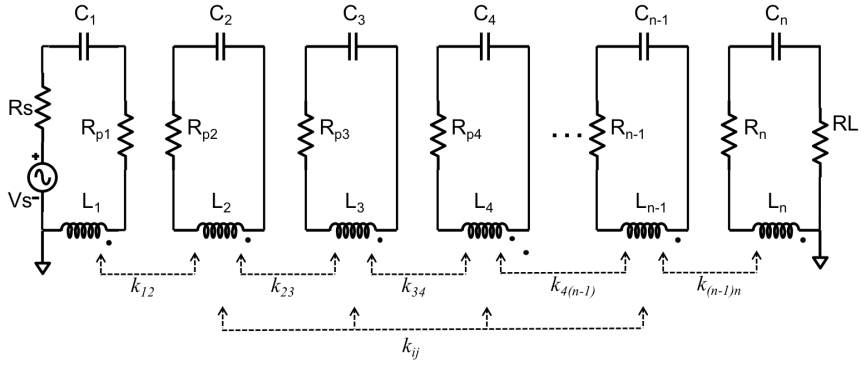

Figure 3.9: Equivalent circuit model of n-coupled resonators

3.4.2 Adjust the coupling between adjacent relay resonators

This section focuses on answering two questions: finding the optimal coupling condition to place relays for extending the range, and concluding assumptions on coupling that can simplify the transfer function matrix of a multi-resonator system.

To capture the full characteristics, we model the coupling between all the coils including all the nonadjacent coil pairs except that the loop-coil coupling is modeled only between the loop and its closest coil. We make an assumption that the coupling between each neighboring pair of relays is the same, so that we can apply the result to systems with different hops. Four different cases of relay setup are modeled: zero-hop, one-hop, two-hop, and three-hop, which consists of four coils, five coils, six coils, and seven coils respectively. Figure 3.10 shows the simulation test setups.

It should be noticed that the setup illustrations are in coaxial arrangement, even though our system consists of planar relays. We choose to model coaxially instead because the mutual inductance formula of the coaxial arrangement is much easier than those with offset and inclination angles [5], and two planar relays can achieve the same coupling value as two coaxial relays with different location arrangement.

The mutual inductance is formulated with Eq.3.5 [5]. Then the coupling coefficient k is

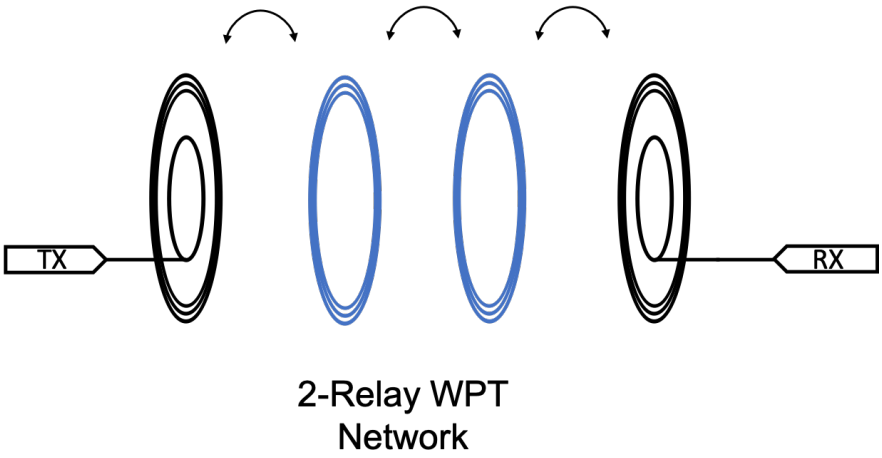

Figure 3.10: Example of a 4-coil WPT system with two coaxial relays inserted for range extension.

calculated with Eq.2.5 accordingly.

$$M = u_0 \frac{\sqrt{r_1 r_2}}{m}((2 - m^2)\boldsymbol{K}(m) - 2\boldsymbol{E}(m)) \tag{3.5}$$

where r_1 and r_2 are the radius of the two loops, K is the complete elliptic integral of the first kind, E is the complete elliptic integral of the second kind, and m is calculated in Eq.3.6.

$$m = \sqrt{\frac{4r_1 r_2}{d^2 + (r_1 + r_2)^2}} \tag{3.6}$$

where d is the distance between the center of the two coaxial loops.

Figure 3.11 shows the change in S_{21} with the increase in the coupling between each adjacent relay pair kcc. The plot shows that the peak S_{21} of each case occurs when kcc is at around the critical coupling point of the no-relay case. In addition, the results of the two-relay and three-relay cases show that with some specific over coupled condition, the system can also achieve good efficiency in addition to the critical coupling case, which is a very useful characteristic to optimize power transfer under crowded relay condition. Whereas,

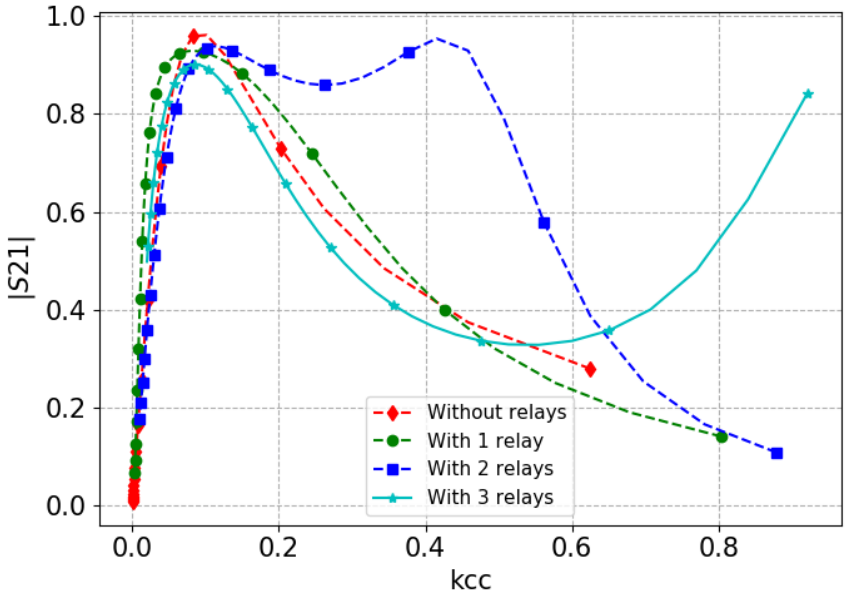

Figure 3.11: $|S21|$ as function of k_{cc} when inserting different number of relays with equal space in between a 4-coil system. Observe the change in S_{21} as the distance between each adjacent relay changes. The change in distance is reflected in terms of kcc, the coupling between each adjacent relay pair. All the cross couplings between any coils are included in this simulation. The couplings with loops are only accounted with the primary coil and the receiver coil.

because the goal for this section is to design the relay platform that optimizes coverage area, we do not explore further in this phenomenon. Thus, we can conclude that **using critical coupling point for adjacent relay coupling is the optimal relay system design**.

We have shown the optimal coupling condition for adjacent coils. The second step is on analyzing the coupling between non-adjacent coils. To observe the impact of coupling between non-adjacent coils, we model and compare each relay system with two conditions: model all the cross couplings between coils, and only model the coupling between adjacent coils. There are relay setups under test, which includes 1-relay, 2-relay and 3-relay. The transmitter to receiver end-to-end distance are adjusted from contactable distance to five

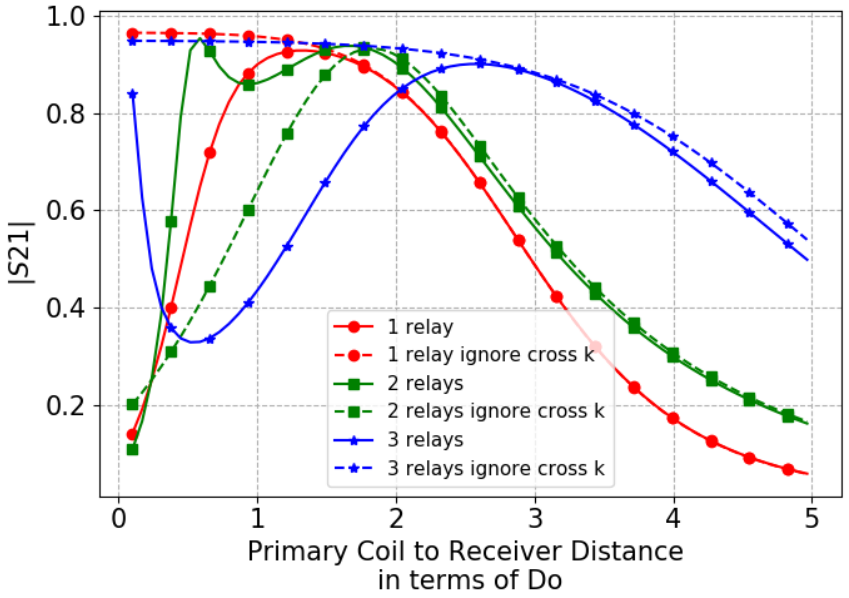

Figure 3.12: The effect of ignoring coupling between non-adjacent relay pairs on S_{21} as the distance between relays changes. The distances between each adjacent relay pairs are the same and changed altogether.

times the relay diameter. For each test of transmitter to receiver distance, the distance between each adjacent coil is adjusted with the same amount to ensure the coupling between adjacent coils to be the same.

Figure 3.12 shows the resulting difference with the two assumptions. It shows that the difference between the two modelings begins to show when the coupling between adjacent coils becomes larger than their critical coupling point. The $S21$ predicted for the 1-relay and 3-relay setup in the over coupled region while ignoring the cross coupling between non-adjacent coils are overestimated in comparison to the modeling when all the cross-coupling are included; on the other hand, the $S21$ predicted for the 2-relay setup is underestimated. Thus, the coupling between non-adjacent coils are negligible when adjacent coils are critically coupled.

In summary, the optimal coupling relationship between every adjacent coil in a linearly arranged relay is critical coupling point. Additionally, certain special over coupled conditions can be as efficient as critical coupled on power transfer but the special over coupling value is different for different number of hops. It means that the spacing which gives rise to optimal over coupling point varies depending on the number of hops, which makes the optimized design of a relay system with one hop number not applicable to another one with different hop number. Because the over coupling condition requires relays to be placed closer, it is not good for extending the wireless power range. Thus, we choose to use critical coupling as the optimal design choice for adjacent coils. When adjacent coils are critical coupled, it is safe to assume that the non-adjacent coils are very under-coupled that their couplings are negligible.

3.4.3 Math Model of Gain Loss with increased number of hops

In the previous section, we presented the analysis of the optimal coupling condition and assumption to extend the wireless power transfer range. In this section, we derive a mathematical expression that quickly predicts the incremental gain reduction with the increase in the number of relay hops with given receiver and relay coil parameters. Incremental gain reduction is a measure of how much the voltage gain is reduced as the number of relays increases to extend the range. Then we can calculate the incremental efficiency reduction. The incremental gain or efficiency reduction of a relay system is a helpful indicator for designers and users to understand the trade-off between efficiency and range of the system.

To simplify the S_{21} matrix calculation, we apply the three assumptions concluded from Section 3.4.2:

- The cross coupling between non-adjacent coils are assumed to be negligible.
- The coupling between each adjacent relay pair is critically coupled, expressed by k_{cc}.
- The receiver coil and end hop relay are critically coupled, expressed by k_{rr}.

k_{cc} is expressed by the critical coupling point between a symmetric 4-coil system in Eq.3.7 [32].

$$k_{cc} = \frac{Q_l Q_c k_{lc}^2 + 1}{Q_c} \tag{3.7}$$

k_{rr} is obtained by finding the critical coupling for asymmetric system in Eq.3.8, which can be computed by differentiating $|S21|$ of an asymmetric 4-coil system in Eq.2.9).

$$k_{rr} = \sqrt{\frac{(Q_l Q_{lc} k_{lc}^2 + 1) * (Q_{rl} Q_{rc} k_{rlc}^2 + 1)}{Q_c Q_{rc}}} \tag{3.8}$$

However, because as the Tx-Rx coil size ratio becomes larger, the voltage gain will no longer have a point where its derivative equals to zero (Section.2.3.1). Thus, Eq.3.8 is only valid when frequency splitting exists within the coil system.

Plug k_{cc} and k_{rr} into the coil system matrix (Eq.3.1), we can obtain the voltage gain equation V_L/V_S for arbitrary number of relay condition. Example expressions of V_L/V_S for 1 relay, 2 relays and 3 relays are shown below.

$$\frac{V_L}{V_s}(1) = \frac{\sqrt{AB(A+1)}}{\sqrt{B+1} \cdot [2(A+1)+1]} \tag{3.9}$$

$$\frac{V_L}{V_s}(2) = \frac{-i\sqrt{AB(A+1)} \cdot (A+1)}{\sqrt{B+1} \cdot [2(A+1)^2 + 2(A+1) + 1]} \tag{3.10}$$

$$\frac{V_L}{V_s}(3) = \frac{-\sqrt{AB(A+1)} \cdot (A+1)^2}{\sqrt{B+1} \cdot [2(A+1)^3 + 3(A+1)^2 + 2(A+1) + 1]} \tag{3.11}$$

where,

$$A = Q_l Q_c k_{lc}^2, \quad B = Q_{rl} Q_{rc} k_{rlc}^2 \tag{3.12}$$

Because A and B are important factors in determining the voltage gain in a relay system and they are both consisted of Q factor and coupling coefficient of the loop and coil, we define them as the **loop-coil parameter**, where A is the Tx loop-coil parameter and B is the Rx loop-coil parameter.

A general expression is summarized in Eq.3.13 with the three equations above in terms of A, B and n, where n represents the number of relays.

$$\frac{V_L}{V_s}(n) = [cos[\frac{3\pi}{2}(n-1)] + i \cdot sin[\frac{3\pi}{2}(n-1)]] \cdot \frac{\sqrt{AB(A+1)} \cdot (A+1)^{n-1}}{\sqrt{B+1} \cdot f(A,n)} \tag{3.13}$$

The phase angle increases by $3\pi/2$ with every added hop. We can simplify Eq.3.13 into Eq.3.14 if we assume that the n^{th} term in $f(A,n)$ is much larger than the $(n-2)^{th}$ term. The assumption is in Eq.3.15.

Approx 1 :

$$\left|\frac{V_L}{V_s}(n)\right| \approx \frac{\sqrt{AB(A+1)}}{\sqrt{B+1}} \cdot \frac{1}{2(A+1)+n} \tag{3.14}$$

Assumption :

$$\begin{aligned} 2(A+1) &>> \frac{2(n-2)}{A+1} \\ A &>> \sqrt{(n-2)} - 1 \end{aligned} \tag{3.15}$$

The assumption shows that *Approx* 1 becomes less accurate as the Tx loop-coil parameter A becomes smaller.

The change in voltage gain of *Approx* 1 is close to a linear relationship with small n and large A, so the second approximation is computed by finding the linear approximate of *Approx* 1, shown in Eq.3.16. The benefit of *Approx* 2 is that it is faster to characterize the speed of incremental gain reduction when increasing the relay hops by calculating the slope of Eq.3.16, and it is moderately accurate for system with fewer relays.

Approx 2 :

$$\begin{aligned} \left|\frac{V_L}{V_s}(n)\right| \approx &- \frac{\sqrt{AB(A+1)}}{\sqrt{B+1}\cdot(4A^2+14A+12)} \cdot n \\ &+ \frac{\sqrt{AB(A+1)}}{2\sqrt{B+1}\cdot(A+1)} \end{aligned} \tag{3.16}$$

The slope of Eq.3.16 is computed by finding the difference between $|V_L/V_s(n=2)|$ and $|V_L/V_s(n=1)|$ with Eq.3.14. Because a smaller absolute value of the slope is desired for a slower decrease in voltage gain when increasing the coverage area, a larger A is wanted.

To validate the simplified approximation expressions, we plot in Figure 3.13 the voltage gain result as the number of relays increases in the system with the two approximation

methods and compare them (Eq.3.14 and Eq.3.16) with the full expression in Eq.3.13. Figure 3.13a shows the comparison with a high Q coil relay system. Figure 3.13b shows the comparison with a relay system with smaller A by having lower Q in relays and the receiver.

The results in Figure 3.13 show that both approximation methods are good for relay systems with high Q, especially with Approx 2. For relay systems with low Q and smaller relays, Approx 2 under-estimates the result as the number of relays increases and Approx 1 over-estimates the result. This makes the average of the two approximation methods closer to the original expression, though low Q coils are not recommended for relay system or other WPT system due to its lossy nature. This agrees with the conclusion that a larger loop-coil parameter is wanted.

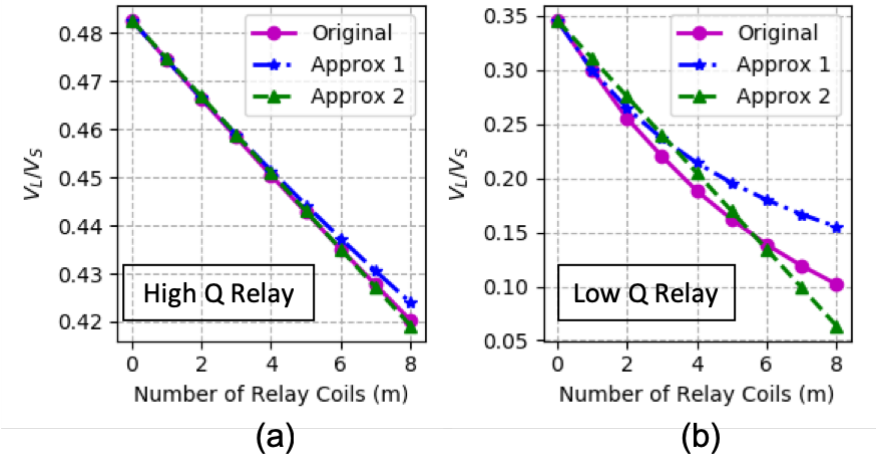

Figure 3.13: Change in voltage gain as the number of relays increases with two approximation methods and the original expression. (a) and (b) compares the difference in the rate of incremental gain reduction and approximation formula accuracy between high Q relay system and low Q relay system. The coils in (a) are modeled with diameter of 16.8 cm and Q of 312. The transmitter and receiver loops in (a) are modeled with Q of 1.14 and loop-coil coupling of 0.28. The coils in (b) are modeled with diameter of 2.8 cm and Q of 90. The loops in (b) are modeled with Q of 0.1 and loop-coil coupling of 0.5.

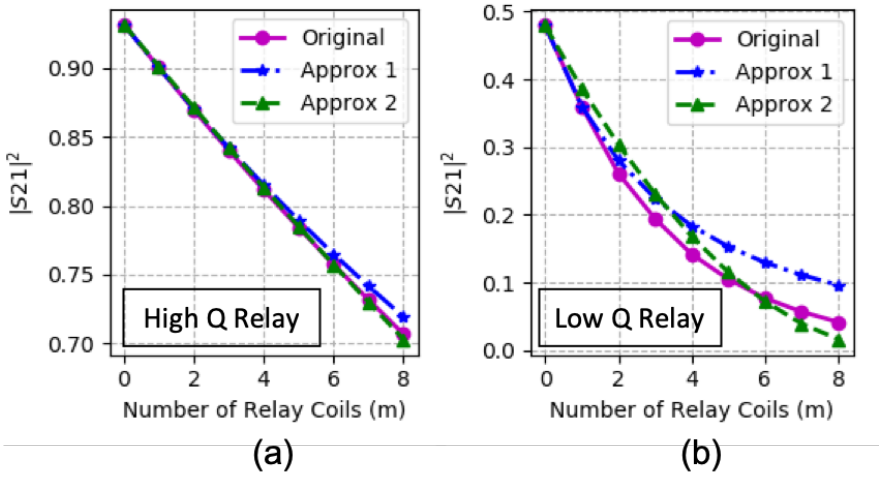

Figure 3.14: Efficiency relationship of the models in Figure 3.13, where (a) shows the high Q relay system and (b) shows the low Q relay system.

Figure 3.14 shows the corresponding efficiency relationship calculated with Eq.2.8 and Eq.2.10, where Figure 3.14a shows the trend with a high Q system and Figure 3.14b shows that with a low Q system. The peak efficiency of the high Q system without relays is 94 %. Its peak efficiency drops to 90 % with one relay added in the system, and 87 % with two relays added. The efficiency with adding n relays is larger than $(\eta_{4coil})^{n+1}$.

In summary, the proposed approximation formulas of incremental gain reduction are accurate when used with high Q relay systems. It simplifies the process of estimating the efficiency reduction as the number of relays increases with given loop-coil parameters of transmitters and receivers.

Chapter 4

IMPEDANCE CHARACTERISTICS OF THE RELAY SYSTEM

Understanding the unique characteristics of the input impedance of a multi-hop relay system is essential. This is because impedance can be used in predicting the power efficiency of the system, and can assist in tuning techniques such as impedance matching to optimize system efficiency. The formula to compute efficiency for the 4-coil system given in Eq.2.10 is under the assumption that the load and source impedances are conjugate matched, with zero reflection [30]. This case represents the maximum efficiency that can be achieved by the passive coil network. To improve the system efficiency in an unmatched impedance condition, we need to know the impedance characteristics of the relay system to design an impedance matching network. In addition, when using coils with non-linear power amplifiers, which is common for wireless power transfer systems, mismatched output impedances change the output power levels and efficiencies of the power amplifiers themselves [35].

In this section, we start by comparing the impact of the load condition of a 4-coil system to a 3-coil system. We then characterize the different impedance characteristics of an unloaded 1D relay array with an even or odd number of hops, with both a lossless and lossy model.

4.1 Impact of the Load on a 4-coil System

We choose to use a 4-coil system as the base structure in our coupled resonator system for its range advantage. Thus, each receiver consists of a loop and a coil. To compare the impact of the change in load impedance on the 4-coil system versus a 3-coil system, we transform the effective impedance of the loaded loop of the 4-coil system into its equivalent 3-coil form with reflected load theory. Reflected load theory is a conventional technique used in the filter theory to obtain the impedance of filter circuits [19]. We choose to use the reflected

load theory rather than the coupled-mode theory used in Chapter 2 and 3 because it is computationally easier than the latter if the cross couplings between non-adjacent coils are negligible.

Figure 4.1 shows the lumped element model of the 4-coil system and its equivalent 3-coil form.

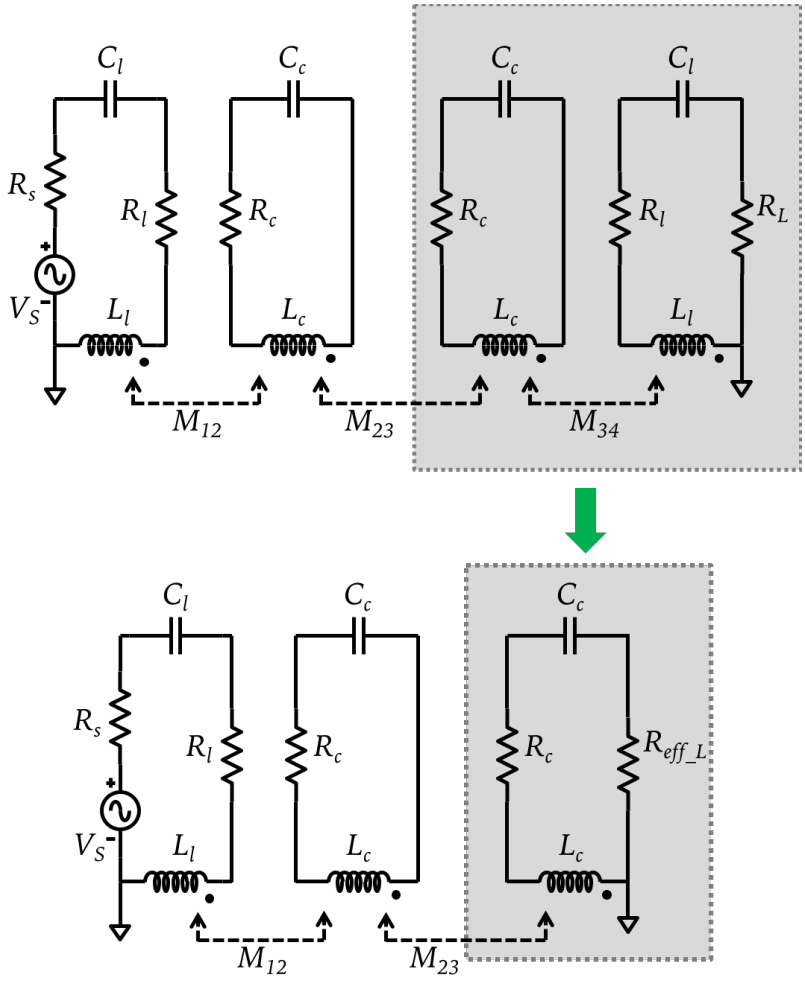

Figure 4.1: Transformation circuit model of a 4-coil system to its equivalent 3-coil model for load impedance analysis.

The highlighted circuit section in Figure 4.1 can be rewritten to its alternative circuit form

in Figure 4.2 [19]. Then, based on the reflected impedance theory, the circuit in Figure 4.2 can again be transformed to the circuit shown in Figure 4.3.

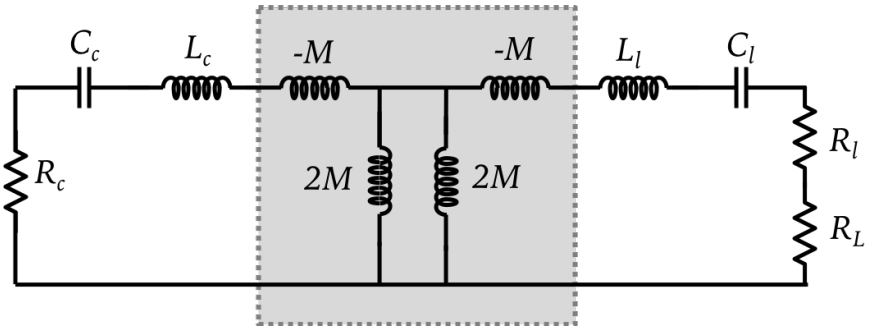

Figure 4.2: Alternative form of two magnetic coupled coils.

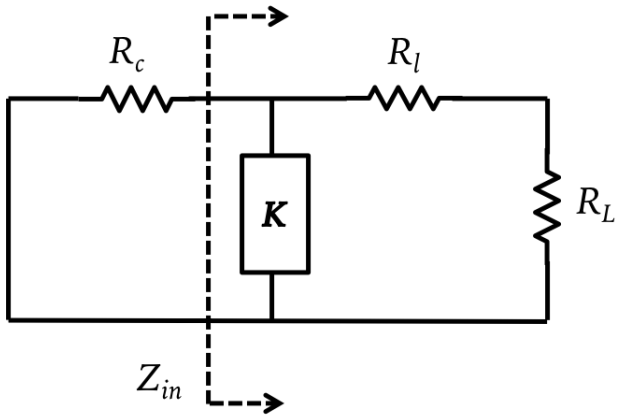

Figure 4.3: The equivalent circuit of two magnetic coupled coils with impedance inverter K, where $K = \omega M$.

The transformation assumes that the operating frequency is the resonant frequency of the coils and loops so that the inductive and capacitive reactance is canceled out, and only parasitic resistance R_c and R_l are left. Z_{in} in Figure 4.3 is the equivalent reflected load

impedance R_{eff_L} in Figure 4.1. It can be computed:

$$Z_{in} = \frac{K^2}{Z} \tag{4.1}$$

Z represents the load impedance and K is expressed in Eq.4.2.

$$K = \omega M \tag{4.2}$$

ω here is the angular frequency, and M is the mutual inductance shown in Figure 4.2. Thus, the reflected impedance of the loaded loop seen by the receiver coil Z_{in} can be calculated in Eq.4.3 with Eq.4.1, Eq.4.2 and Eq.2.5.

$$\begin{aligned} Z_{in} &= \frac{K^2}{Z} \\ &= \frac{\omega^2 M^2}{R_l + RL} \\ &= \frac{\omega^2 k_{lc}^2 L_l L_c}{R_l + R_L} \\ &= Q_{lL} Q_c R_c k_{lc}^2 \\ &\text{or} \\ &= \omega Q_{lL} L_c k_{lc}^2 \end{aligned} \tag{4.3}$$

where Q_{lL} is the loaded Q of the receiver loop, Q_c is the Q of the receiver coil, R_c is the parasitic resistance of the receiver coil, and k_{lc} is the coupling value between the receiver loop and coil.

To compare the change of load impedance of a 4-coil system to that of a 3-coil system, we plot the impedance of R_{eff_L} with a range of R_L from 10 Ω to 250 Ω with Eq.4.3 in Figure 4.4. The Q_c, k_{lc}, R_c, R_l, and L_l values are chosen based on practical examples that are 122, 0.5, 0.8 Ω, 0.1 Ω, and 0.0918 μL respectively. The figure shows that the change of R_{eff_L} is inversely proportional to the change of R_L. The key takeaway is that R_{eff_L} stays within a very limited range even with large variation of R_L. This means with the same range of loading conditions, the 4-coil system exhibits a smaller impedance range than that seen with a 3-coil system. When the same impedance matching network is applied at the receiver

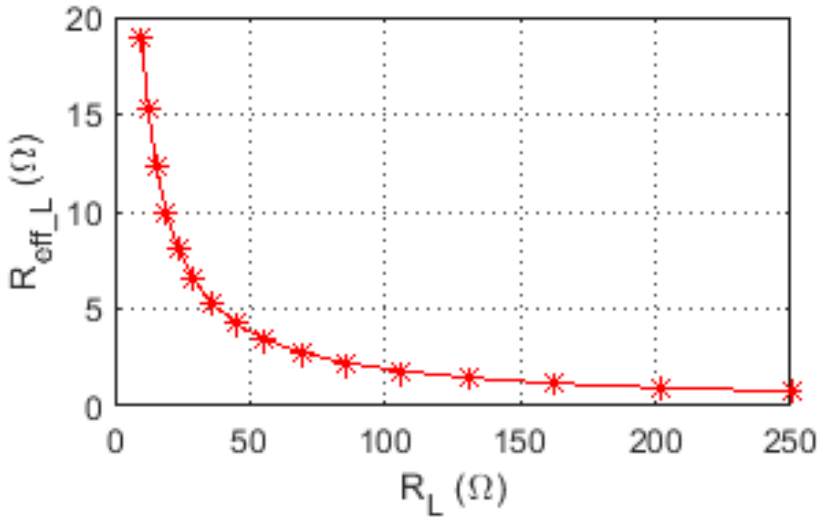

Figure 4.4: The reflected impedance R_{eff_L} of the loaded Q of a 4-coil system as the load R_L changes.

of a 4-coil system, the effect of tuning is not as pronounced as it would be on a 3-coil system.

4.2 Impedance Characteristics of 1D Unloaded Relay with Even or Odd Number of Hops

Understanding the unique characteristics of the input impedance of an adaptive multi-hop system is important in predicting and optimizing efficiency because power amplifier efficiency varies with the load impedance. In this section, we focus on characterizing the input impedance of the unloaded 1D relay array as the number of relay hops increases and comparing the impedance characteristics between even and odd number of relays.

4.2.1 Impedance characteristics with lossless coils

To characterize the impedance change as the number of hops increases, we start the modeling with lossless coils in an ideal case. Figure 4.5 shows the model of the n coil relay array, where

1^{st} *coil* is the driven loop, 2^{nd} *coil* is the primary coil, 3^{rd} *coil* is the first hop and n^{th} *coil* is the $(n-2)^{th}$ *hop*. Because we have concluded in Section 3.4 that extending the range with a 1D relay array is optimal when each adjacent pair of relays are critically coupled, we assume the relays in Figure 4.5 are equally spaced, which means the coupling between each adjacent pair of relays are the same, and the coupling between all the non-adjacent coils can be ignored. The equivalent circuit model with impedance inverter K of the 1D relay array is shown in Figure 4.6. The impedance of the network is calculated with two cases: odd and even in Eq.4.4 and Eq.4.5 respectively.

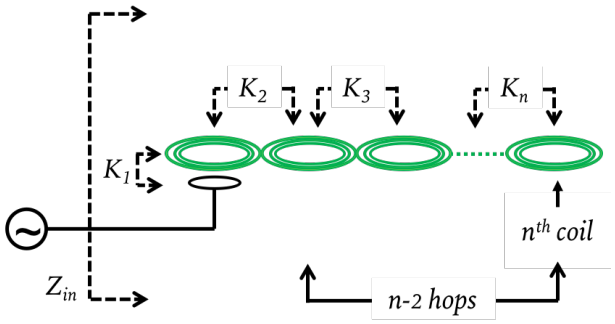

Figure 4.5: 1D relay array network with n coils. There are equivalently $n-2$ hops.

In the ideal lossless case, the even number of hops results in the expected input impedance of the 1D relay to be infinity, which is equivalent to an open circuit case (Eq.4.5); when the 1D relay has an odd number of hops, the expected input impedance of the system is zero, a short circuit equivalent (Eq.4.4). This is a very distinct difference in input impedance caused by the different number of hops in the system.

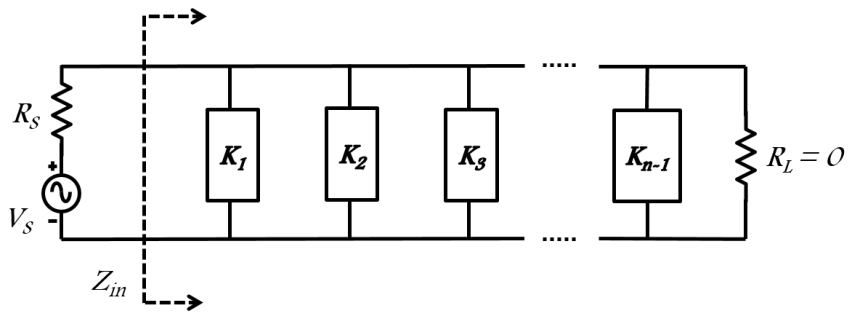

Figure 4.6: Circuit equivalent of 1D relay array of n lossless coils with impedance inverter K.

n is odd (odd hops) :

$$\begin{aligned} Z_{in} &= \frac{K_1^2 \cdot K_3^2 \cdots K_{n-2}^2 \cdot R_L}{K_2^2 \cdot K_4^2 \cdots K_{n-1}^2}, \quad K_1 \neq K_2 = \cdots K_{n-1} \\ &= \frac{K_1^2 \cdot \cancel{K_3^2} \cdots \cancel{K_{n-2}^2} \cdot R_L}{\cancel{K_2^2} \cdot \cancel{K_4^2} \cdots K_{n-1}^2} \\ &= \frac{K_1^2}{K_{n-1}^2} \cdot R_L \\ &= 0 \end{aligned} \tag{4.4}$$

n is even (even hops) :

$$\begin{aligned} Z_{in} &= \frac{K_1^2 \cdot K_3^2 \cdots K_{n-3}^2 \cdot K_{n-1}^2}{K_2^2 \cdot K_4^2 \cdots K_{n-2}^2 \cdot R_L}, \quad K_1 \neq K_2 = \cdots K_{n-1} \\ &= \frac{K_1^2 \cdot \cancel{K_3^2} \cdots \cancel{K_{n-3}^2} \cdot \cancel{K_{n-1}^2}}{\cancel{K_2^2} \cdot \cancel{K_4^2} \cdots \cancel{K_{n-2}^2} \cdot R_L} \\ &= \frac{K_1^2}{R_L} \\ &= \infty \end{aligned} \tag{4.5}$$

This information can be used to guide the design of the wireless power transfer system. For instance, a commonly used non-linear power amplifier, a class E power amplifier, is designed for a specific load impedance. When the load is mismatched, the efficiency of

the power amplifier is significantly affected, and an impedance matching network ideally would be added to mitigate the problem. For the condition without an impedance matching network, an open load condition is typically better than the short circuit condition because most power amplifiers can operate with an open load condition, but a short circuit load will most likely trigger the circuit protection module as it is considered as a malfunction.

In summary, whether the number of hops is even or odd results in a significant difference in the input impedance value of a 1D unloaded relay array. The even number of hops results in the input impedance of the relay system to be infinity in a lossless world, while the odd number of hops results in zero input impedance. This feature should be well acknowledged by designers and users before designing or using the relay system. These formulas, computed for a lossless system, gives a reasonable expectation of opposite impedance characteristics when using even versus odd numbers of relays. In the next section, we will explore the relationship in the practical case where the coils have parasitic resistance.

4.2.2 Impedance characteristics with lossy coils

The previous section (Section 4.1) characterizes the input impedance of the unloaded 1D relay array under the assumption of a lossless condition for easier calculation. It gives a rough expectation of the different trends when using different numbers of relays: even numbers of hops results in an open circuit, while odd numbers of hops results in a short circuit. However, when the relay system is used with a power amplifier, the exact value of the input impedance becomes very important, because each type of power amplifier responds to load impedance differently in terms of its efficiency and power output. To realistically model a relay array, the parasitic resistance must be considered. Thus, there is a need to do the input impedance analysis with lossy coils. In this section, we include parasitic resistance in the model to see the impact it has on the input impedance, and conclude how the input impedance changes as the number of hops increases.

Figure 4.7 shows the circuit model of a lossy n-coil 1D relay array system. The analytical

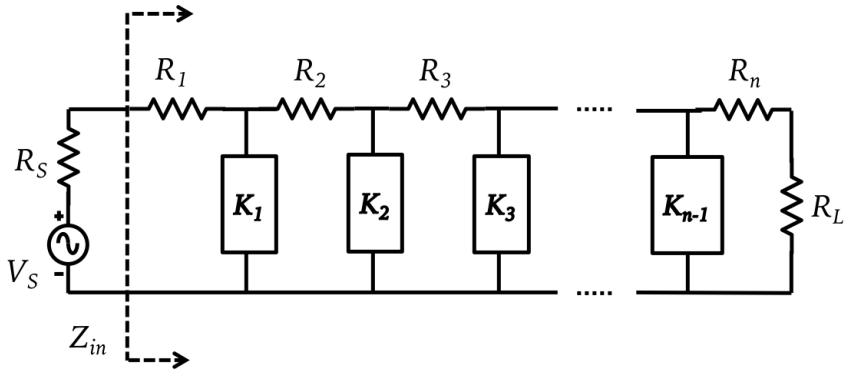

Figure 4.7: Circuit equivalent of 1D relay array of n lossy coils, using the impedance inverter K.

input impedance Z_{in} is computed in Eq.4.6:

$$Z_{in} = R_1 + \cfrac{K_1^2}{R_2 + \cfrac{K_2^2}{R_3 + \cfrac{K_3^2}{R_4 + \cdots + \cfrac{K_{n-2}^2}{R_{n-1} + \cfrac{K_{n-1}^2}{R_n}}}}} \tag{4.6}$$

where:

$$\begin{aligned} K_1 \neq K_2 = K_3 = \cdots K_{n-1} = K_{cc} \\ R_1 \neq R_2 = R_3 = \cdots R_{n-1} = R_c \end{aligned} \tag{4.7}$$

Z_{in} in Eq.4.6 can be then simplified into Eq.4.8 for the odd hop case, and Eq.4.10 for the even hop case with assumptions in Eq.4.9 and Eq:4.11 respectively.

n is odd (odd hops) :

$$Z_{in}(n) = R_1 + \frac{n-1}{2} \cdot R_c \cdot \frac{K_1^2}{K_{cc}^2} \tag{4.8}$$

Assumption :

$$K_{cc}^2 >> R_c^2 \cdot \frac{n-1}{2} \tag{4.9}$$

n is even (even hops) :

$$Z_{in}(n) = R_1 + \frac{K_1^2}{\frac{n}{2} \cdot R_c} \tag{4.10}$$

Assumption :

$$K_{cc}^2 >> R_c^2 \cdot \frac{n-2}{2} \tag{4.11}$$

From Eq.4.8, the input impedance of the relay array with an odd number of hops increases proportionally as the number of hops and parasitic resistance of the coils increase. The input impedance with an even number of hops shows the opposite trend (Eq.4.10). However, the two assumptions Eq.4.9 and Eq.4.11 used to simplify and compute the approximation equations indicate that when K_{cc} cannot keep up with the increasing speed of the number of hops and parasitic resistance of relay coils, the assumptions become less accurate. To compare the difference, Figure 4.8 plots the input impedance as a function of number of relay hops and coil parasitic resistance with the approximation equations (Eq.4.9 and Eq.4.11) and the original equation (Eq.4.6). The other parameters used in the calculation are modeled based on a PCB coil 5 cm in diameter and summarized in Table.4.1.

Table 4.1: Parameters for the Coils and the Loop

Coil Parameters	**Value**
Inductance (L_c)	$1.148\mu H$
Parasitic Resistance (R_c)	0.8 Ω
Coil-Coil Coupling (k_{cc})	0.045
Loop Parameters	**Value**
Inductance (L_l)	$0.0918\mu H$
Parasitic Resistance (R_l)	0.1Ω
Coil-Coil Coupling (k_{lc})	0.5

Figure 4.8a shows the comparison of approximate and original expressions with an odd number of hops. Figure 4.8b shows the comparison with an even number of hops. In both subplots, the picture on the right is the side view of the one on the left. The result shows

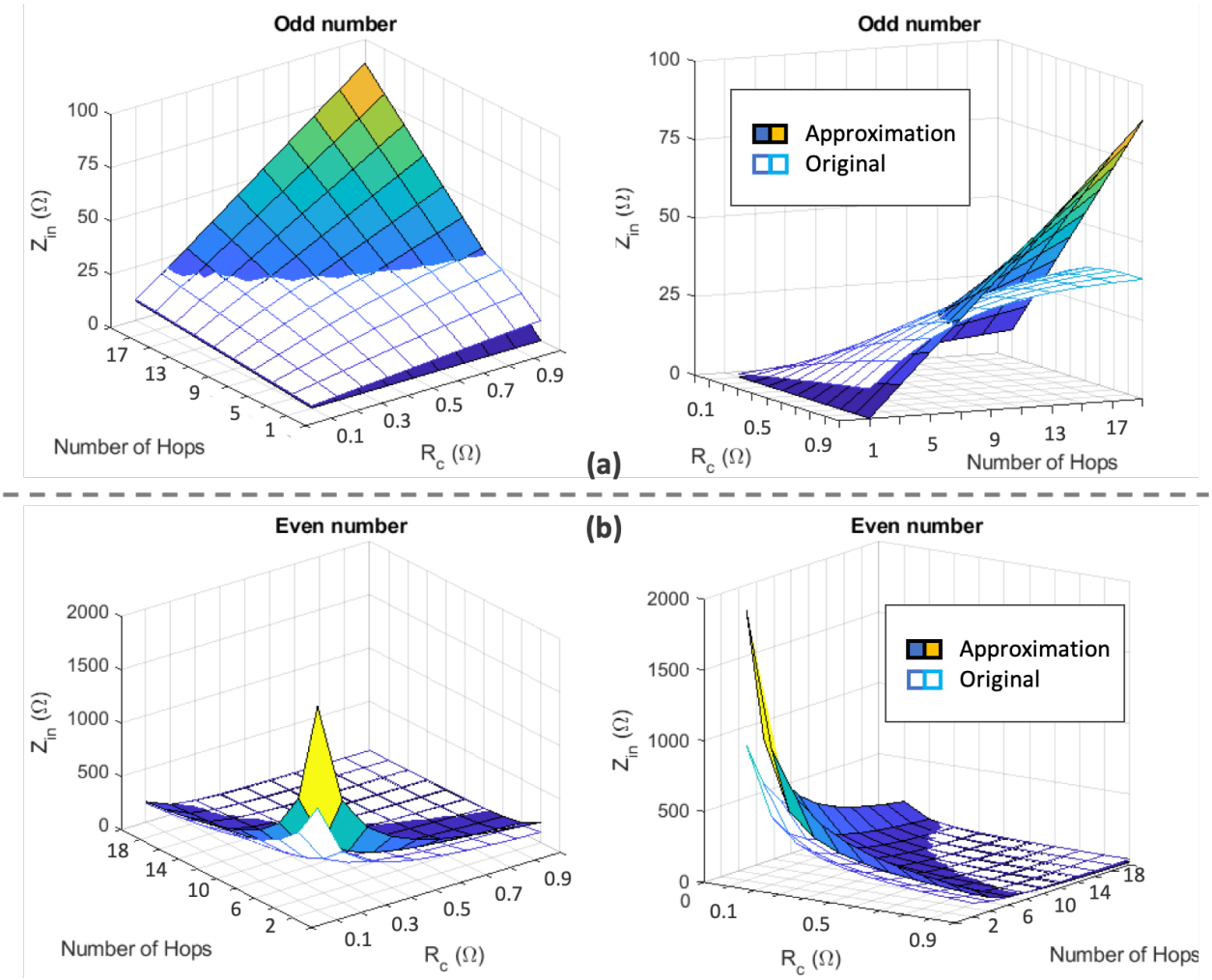

Figure 4.8: Comparing approximate and exact analytical result of input impedance Z_{in} of a 1D relay array as a function of the number of hops and parasitic resistance of the coils. The approximate formulas are given in Eq.4.8 and Eq.4.10, and the full expression is given in Eq.4.6. (a) shows the Z_{in} comparison with an odd number of hops, and (b) shows the Z_{in} comparison with an even number of hops. The other parameters used in computing the result are listed in Table.4.1.

that the approximate formulas are more accurate with either small R_c or fewer number of hops, which is consistent with the assumption. Eq.4.8 underestimates Z_{in} while Eq.4.10 overestimates Z_{in} with smaller n and R_c. At larger n and R_c, Z_{in} of the even and odd number of hops converges when they are calculated with the original expressions, while Z_{in} calculated with the approximate method for the even case and the odd case continues to decrease and increase as the number of hops increases, respectively.

While the approximate formulas are useful to quickly estimate the input impedance for high Q relay arrays with fewer hops, it is also useful to understand the converging phenomenon when modeling relay system with longer hops. Figure 4.9 shows the converging in Z_{in} computed with Eq.4.6. The input impedance converges to the same value with different R_c. The larger the R_c is, the faster it converges. The more it converges, the less difference there is between even and odd hops, which may or may not be a preferred feature. When the relay is connected to a Class E power amplifier, and the input impedance is close to the designed output impedance of the amplifier, the power will be efficiently delivered to the relay system even without any load. This is what we try to avoid because any power used under this condition is wasted; the energy is dissipated by the ohmic loss as heat. To prevent this from happening, one strategy is to design the system so that the impedance difference between the even and odd number of hops is large enough to take advantage of the more desirable of the two impedances. Thus, it is essential to know the input impedance characteristics of the relay system in order to understand the limits of its scaling.

In summary, this section covered the input impedance characteristics of a 1D relay array system. Approximate formulas were derived to calculate the input impedance value quickly. The approximations are accurate when used with high Q resonators and fewer number of hops.We described how different the input impedance is between relay systems with even and odd numbers of hops and how the two converge as the number of hops increases or the parasitic impedance of coils increases. The impedance characteristics of the relay system are helpful when optimizing efficiency of the system's operation.

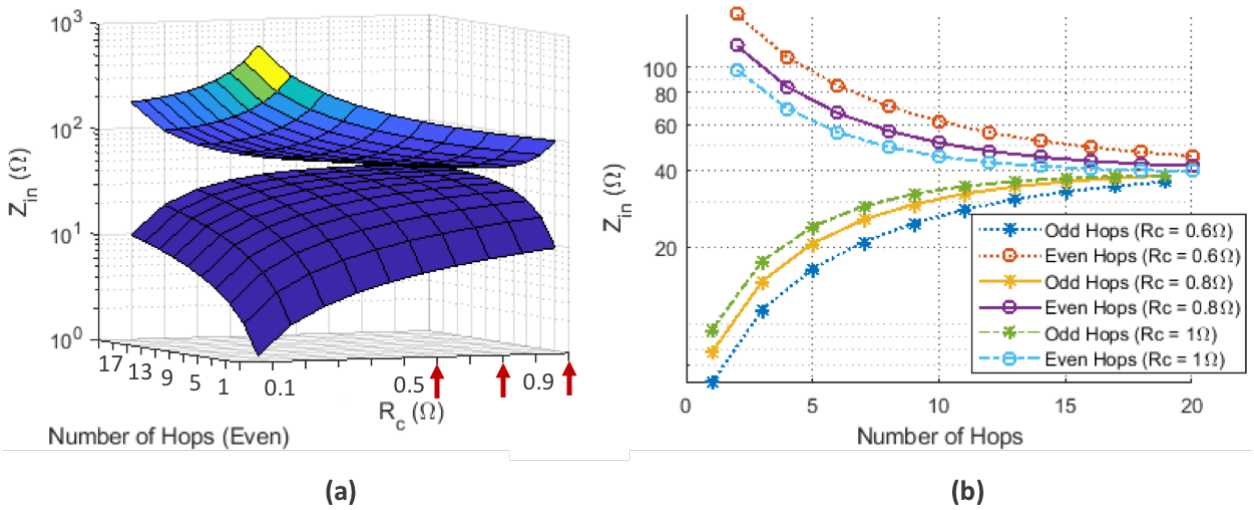

Figure 4.9: Convergence of input impedance Z_{in} of a 1D relay array as number of hops increases and parasitic resistance increases, simulated with Eq.4.6. (a) shows how Z_{in} changes with respect to number of hops and R_c. (b) shows the selected cases of Z_{in} that are highlighted with red arrows in (a), where $R_c = 0.6\ \Omega$, $R_c = 0.8\ \Omega$, and $R_c = 1\ \Omega$. The other parameters used in computing the result are listed in Table.4.1.

Chapter 5

RECONFIGURABLE 2D RELAY PLATFORM

Previous chapters have discussed how we can use relays to extend wireless power range. However, when we try to cover a large two-dimensional (2D) area with relays, just simply placing relays side by side is not an efficient method of on transferring power everywhere on the surface [36]. In addition, as we have shown in Chapter 3, when constrained to a single fixed operating frequency, even a simple linear path of arranged planar relays cannot transfer power efficiently to every location along the linear path, but end-hop strategy and spatial tuning can help boost the efficiency. Thus, we need reconfigurability to be implemented on a 2D transmitter, enabling optimal relay configurations based on receiver loading conditions.

To design the 2D reconfigurable relay transmitter system, we characterize the optimal relay configuration for different receiver location conditions which suggests how we should reconfigure relays based on receiver location. Next, we describe how to implement the reconfigurable relay system in hardware, which specifically includes how to design the coil geometries and the switchable coils. Then we discuss how to track receiver movements and present three algorithms that are designed for delivering power to moving receivers with a centrally controlled array of reconfigurable relays (CARR). Lastly, we discuss the implementation and evaluation of the CARR system.

5.1 Motivations for Reconfigurable Relays

If simply placing a plane of tessellated relays can effectively extend the power transfer efficiency, there is no need for reconfigurable relays. To examine the need, this section first analyzes the frequency response of a 2D relay array, all of which resonate at the same frequency in Section.5.1.1. Then it summarizes the benefit that a reconfigurable relay platform

can improve in Section.5.1.2.

5.1.1 All-on Relay Array

The resonant modes of the 1D relay array have been thoroughly studied in Chapter 3. That chapter shows that the difference in resonant modes at different locations, which is caused by the interference between relays, results in very non-uniform distribution of power transfer efficiency at the relays' natural resonant frequency. Knowing the impact of interference among 1D relays, this section examines the performance of the 2D relay array.

Figure 5.1a shows a rotational symmetrical 2D relay array with the primary relay coil located at the center, and all the relays tuned to resonate at 13.47 MHz. Figure 5.1b,c,d show the $|S_{21}|$ result, an indicator for efficiency, received when a receiver is critically coupled to the relay plane at three difference frequencies. These $|S_{21}|$ results are measured at the dotted locations, and then extrapolated to the rest of the surface area based on the rotational symmetry of the transmitter.

Figure 5.1b shows the $|S_{21}|$ at the natural resonant frequency 13.47 MHz of the coils. Figure 5.1c shows the response at 13.55 MHz in which the array has the highest average $|S_{21}|$. Figure 5.1d shows the response at 13.95 MHz when the receiver conceives the highest $|S_{21}|$ at the primary coil location. The results show that when the 2D relays are all resonant at the same time, the locations that receive peak $|S_{21}|$ change with different frequencies. For instance, the locations where maximum $|S_{21}|$ occur at 13.55 MHz are the null locations when operated with 13.95 MHz. Among all three frequencies, the system has the worst $|S_{21}|$ when operating with the natural frequency. Thus, if frequency tracking method is not prohibited by regulation, it can improve efficiency when moving across the plane.

Figure 5.2 shows the frequency response at the five test locations respectively. It shows how the frequency where peak $|S_{21}|$ occurs changes as the receiver location changes. In addition, it shows that at locations that are two-hop away from the primary coil (location 1 and 2), the maximum achievable $|S_{21}|$ across frequency at each location is below 0.4, which is much worse than the result of the 1D relay case with the same distance apart in Figure 3.3.

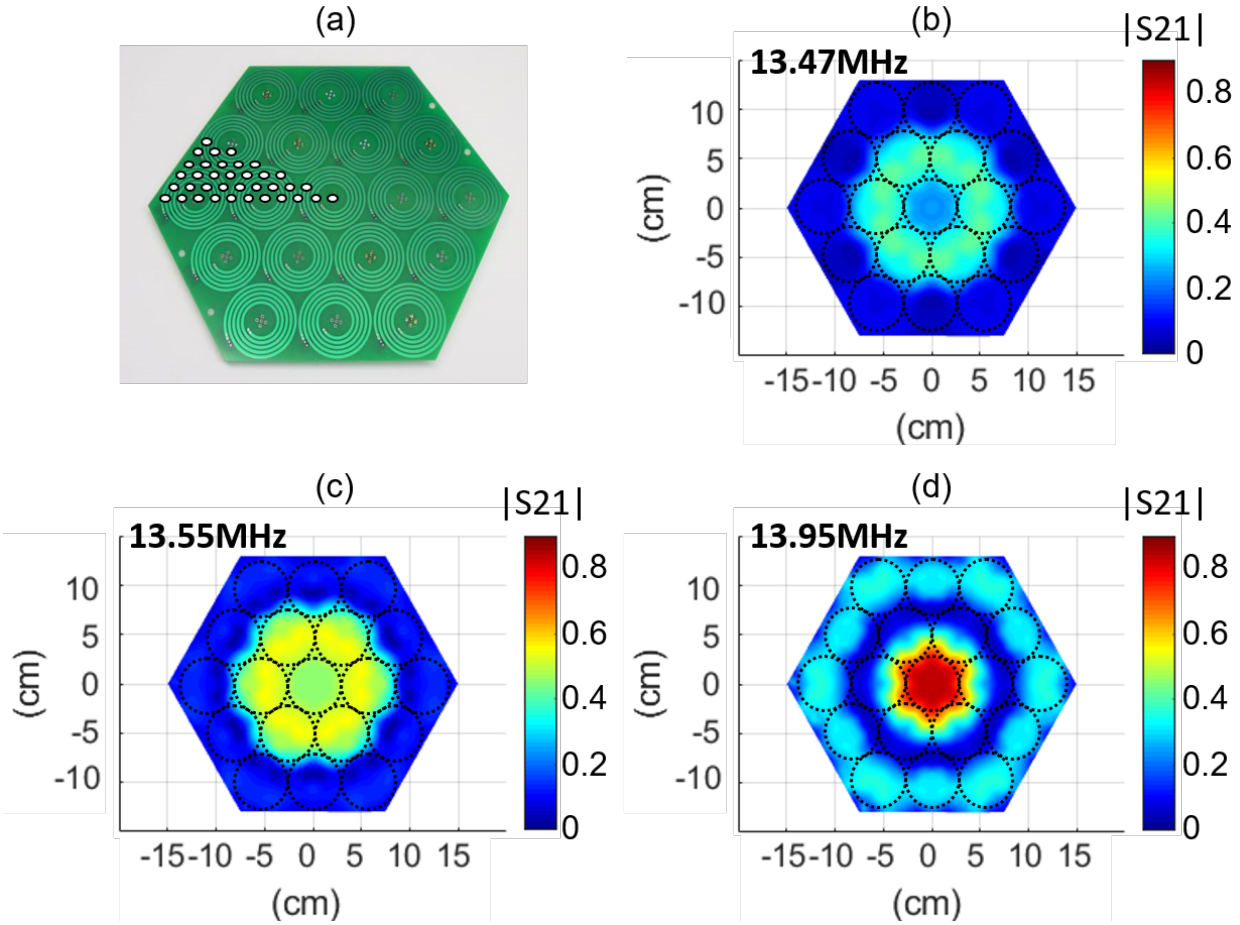

Figure 5.1: (a). Picture of a rotational symmetrical 2D relay transmitter, with primary relay coil in the center. The dots indicate the locations where $|S_{21}|$ measurement were taken with a receiver that is the same geometry of the unit relay with s separation distance of 4 cm. (b). The $|S_{21}|$ value at 13.47 MHz, the natural resonant frequency of each relay. (c). The $|S_{21}|$ value at 13.55 MHz which the relay has the highest average $|S_{21}|$ among all the locations. (d). The $|S_{21}|$ value at 13.95 MHz when the $|S_{21}|$ reaches its peak at the primary coil location.

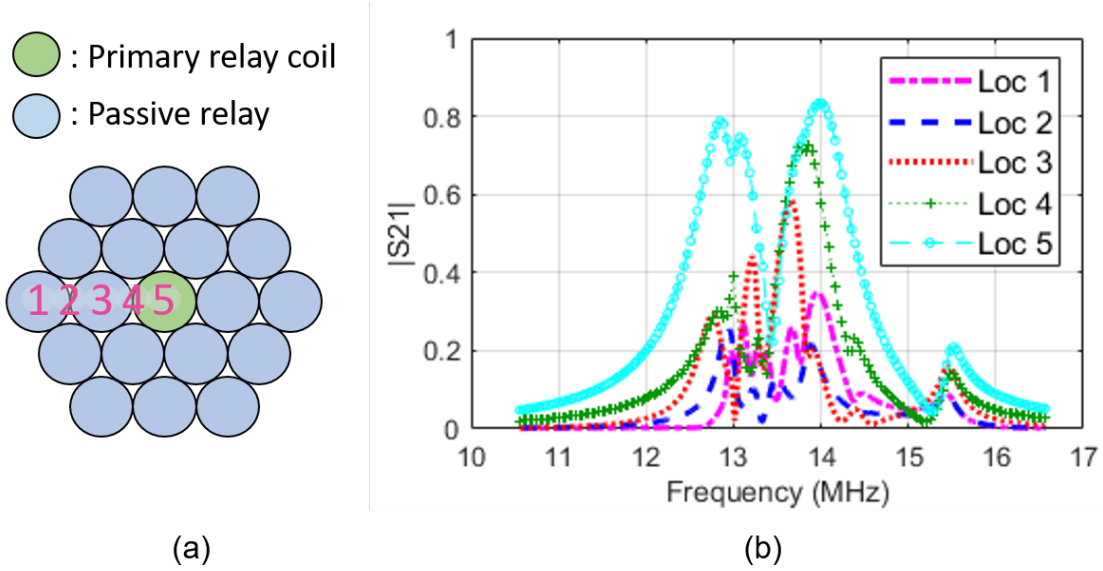

Figure 5.2: (a). Five locations where $|S_{21}|$ was measured. (b). The frequency responses of $|S_{21}|$ of receiver at locations 1 to 5 when all the resonators are resonant at 13.47 MHz.

The results show that, it is difficult to find an optimal frequency that works for all the locations with a 2D all-on relay transmitter compared to the 1D relay case. Even if the frequency tracking method can be implemented, it is not efficient at delivering power to large area.

5.1.2 Capability of Reconfigurable Relays

An explanation for the result of the 1D relay array being more efficient than the 2D relay array is that even though the distance of the shortest path between the end hop and the primary coil for both cases is the same, the interference of each surrounding relay generates more loss and destructively interferes the resonant modes of each other. Thus, it can be concluded that in order to extend the same distance away from the primary coil, using 1D relay is better than 2D relay. But if we want to have a 2D coverage, we need the relay transmitter to be reconfigurable so it can switch between different configurations. The 2D

relay plane gives many possible relay configuration patterns. To decide on the optimal configuration for each loading condition and location, we develop a method in the following section.

5.2 Optimal Relay Configurations with 1D and 2D relays

5.2.1 Spatial Tuning with 2D Cluster Relays

Chapter 3 introduces the idea that using spatial tuning can improve efficiency in 1D relay resonator systems. This section discusses how a 2D relay array can be used to improve efficiency with spatial tuning. Spatial tuning refers to adding or reducing relays to change the resonant modes in our favor so that the $|S_{21}|$ at the natural frequency is optimized.

To study the effect of tuning with 2D relays, we conduct an experiment in which we pick a null location that was previously shown in Chapter 3 and observe the change of resonant modes as we add additional relays to the system.

The configuration labeled as config a in Figure 5.3 is compared against four relay configurations that are labeled as config b, c, d in Figure 5.3. The red cross mark indicates the XY location of the receiver with 4.5 cm vertical distance apart from the transmitter plane. The relay transmitter and receiver used in the experiment are the same ones as shown in Figure 5.1.

From Figure 5.3a, when we add a relay in the direction of the misaligned receiver, it generates one resonant mode that has maximum $|S_{21}|$ at a higher frequency than the natural resonant frequency, which is the frequency where max $|S_{21}|$ occurs in config a. By adding another relay as shown in Figure 5.3b, an additional resonant mode is generated, and it pushes the frequency of the middle resonant mode to be smaller. We then add a third relay that forms a 2D cluster shape in Figure 5.3c. That results in the bandwidth of the middle resonant mode to be larger and shifts the center of the resonant mode closer to the natural frequency. Adding a fourth relay as shown in Figure 5.3d increases the $||S_{21}||$ by 0.07, which could be caused by the creation of the very narrow resonant mode that centers around

13.1 MHz. This improvement is small enough to be ignored, so configuration in Figure 5.3c is sufficient as the optimal choice among the test cases.

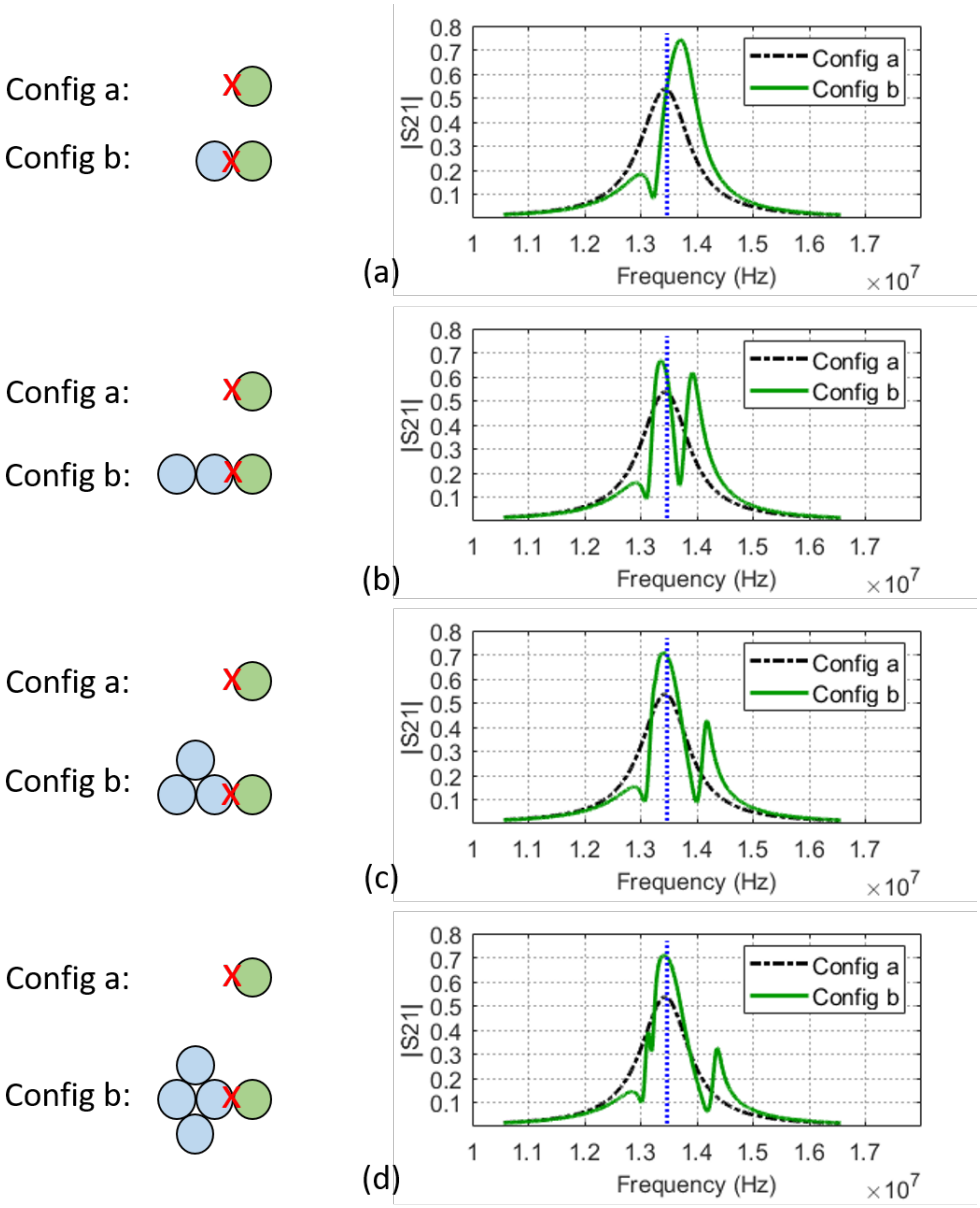

Figure 5.3: Experiments of efficiency improvement with 2D cluster relays using spatial tuning. The red cross mark indicates the location of receiver in the XY plane. The vertical distance between the relay plane and the receiver is 4.5 cm.

In summary, we demonstrate that 2D cluster relays are effective in spatial tuning and we should use it to improve efficiency with 2D relay platform.

5.2.2 Search for Optimal Relay Configuration

We have demonstrated in Chapter 3 that when a receiver is above and centered on a relay of a relay array platform with critical coupled distance, the relay path that connects the primary coil and that relay with the fewest hops is most likely the optimal configuration for steering power to the receiver. We call this method the "single-leg-end-hop strategy". However, when the receiver is not at the center of any unit relay of the array, the single-leg-end-hop strategy may no longer be optimal. Additionally, we have shown that by adding relays carefully to a group of relay networks, we are able to adjust the frequencies where peak $|S_{21}|$ occurs with both 1D and 2D relays. Section 5.2.1 shows that using of cluster relay can mitigate efficiency nulls. Therefore, to study the optimal configuration for each location on the platform, the method we employ is to first find the group of relay configurations that are expected to deliver good efficiency for the intended load conditions based on conclusions from previous sections; then we find the optimal configuration for each load condition by finding the maximum $|S_{21}|$.

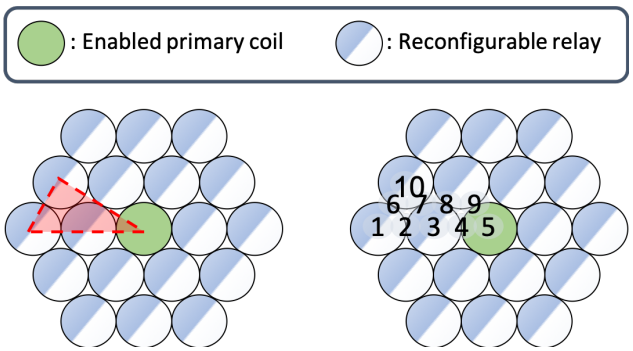

Figure 5.4: Relay transmitter under test.

Relay Configuration Test Candidates

We have chosen the relay transmitter as shown in Figure 5.4 to find the optimal configuration for each location. It is selected because it is a rotational symmetrical structure that contains the least number of hops that includes both linear relay configurations and cluster relay configurations. The test locations for the search are reduced to the red triangle section to reduce redundancy. This area is then divided into ten locations with resolution of the radius of the relay, marked in Figure 5.4.

The relay configuration candidates for the test locations are selected based on previously concluded rules:

- Single-leg-end-hop strategy is good for transferring power when receivers are critically coupled.

- The frequency of peak $|S_{21}|$ can be adjusted by spatial tuning, which is adding relays that are not along the shortest path between the primary coil and the receiver coil.

- Cluster relays can boost efficiency at some null locations that are created with linear arranged relays.

Therefore, twelve configuration candidates are selected and shown in Figure 5.5. All the single-leg options (config 2, 3, 7 and 8) that are included in the triangle area are selected due to single-leg-end-hop strategy. Middle-driven configurations (config 4 and 5) are also selected for its ability on frequency tuning of peak $|S_{21}|$. Config 6 is a special case of linear arranged relay to diversify the test space. Three cluster relays (config 9 to 11) that include parts of the test locations and with the fewest number of hops are selected. Cluster relays that are far away from the test locations are not included because the non-adjacent relays do not boost the coupling between the receiver and transmitter. Config 0 is a special configuration that does not contain any relays but only a driven loop. Config 1 represents another special case with only primary relay coil but zero-hop.

Exploration of Optimal Configurations

To search for the optimal configuration for each location, we set up the receiver in parallel to the relay plane at the ten locations with a separation distance of 0 cm and 4 cm, which represents over coupling and critical coupling respectively. At each location, $|S_{21}|$ is collected with a vector network analyzer (VNA) while the relays are configured to each of the twelve configurations shown in Figure 5.5.

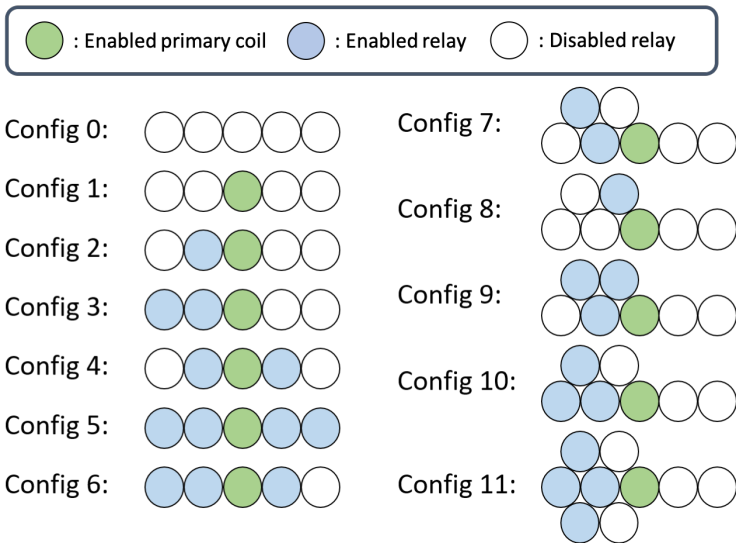

Figure 5.5: Selected twelve relay configurations to be tested for optimal configuration at each location in Figure 5.4

.

The configurations with the highest $|S_{21}|$ at each location of each chosen frequency are selected as the first step. Secondly, because the frequency used at different locations needs to be the same due to regulation, the optimal configuration at each location is determined by selecting the frequency that has the largest average $|S_{21}|$, and then the corresponding configurations become the optimal configurations for the test locations. Figure 5.6 shows the statistics of the best $|S_{21}|$ achieved at each receiver location when the receiver is separated with 4 cm from the relay plane, and Figure 5.7 shows the same with 0 cm receiver separation.

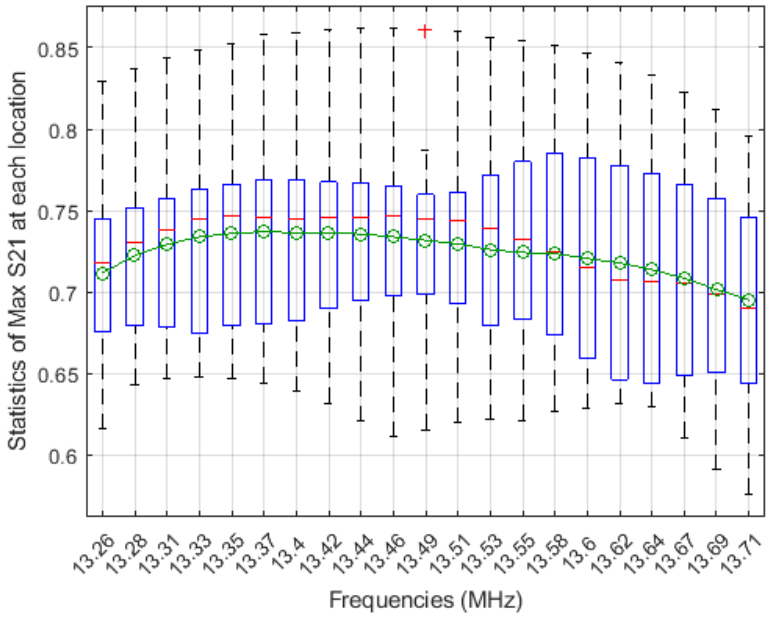

Figure 5.6: The statistical distribution of maximum $|S_{21}|$ received at each location (in Figure 5.4) tested with all the configurations (in Figure 5.5) across a range of selected frequencies. The distance between receiver and relay plane is 4 cm. The green line is the mean of the best $|S_{21}|$ at each location for the corresponding frequency.

From the statistics plot Figure 5.6, the frequency that has the largest average $|S_{21}|$ of the 4 cm case is 13.37 MHz, though it is not significantly larger than the $|S_{21}|$ at the natural frequency of each relays. On the other hand, the optimal frequency of the 0 cm case is 13.49MHz (Figure 5.7). Thus, we choose to use the natural frequency as the optimal frequency. The configurations used at 13.49MHz are summarized in Figure 5.8. Figure 5.9 shows the $|S_{21}|$ measured at each location with the selected configurations.

The results show that the linear path relay configuration is better than cluster relays when the receiver is very close to the transmitter plane. When the receiver is 4 cm above and centered on a relay (Location 1, 3, 10), the optimal configuration can either be linear arranged relays or cluster relays. This implies that spatial tuning effect with cluster relays

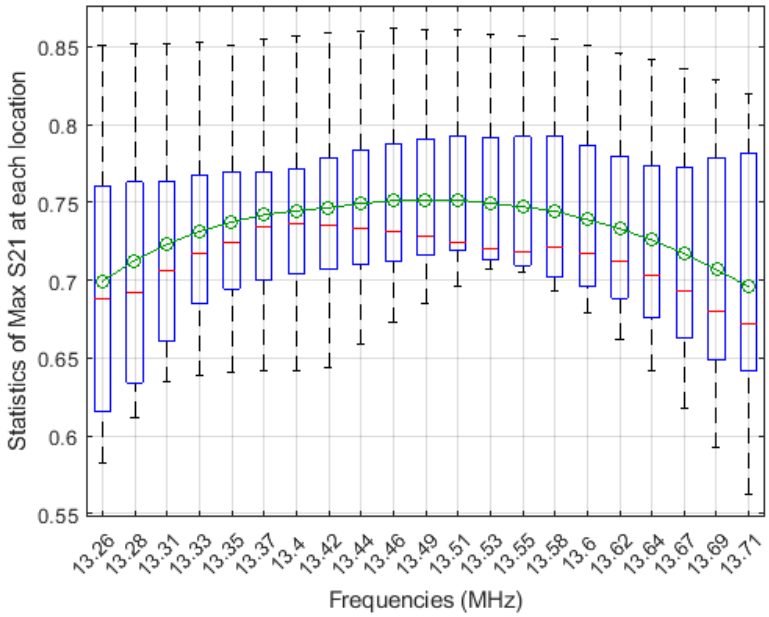

Figure 5.7: The statistical distribution of maximum $|S_{21}|$ received at each location (in Figure 5.4) tested with all the configurations (in Figure 5.5) across a range of selected frequencies. The distance between receiver and relay plane is 0 cm. The green line is the mean of the best $|S_{21}|$ at each location for the corresponding frequency.

can not only help with receiver located in between relays but also on locations that linear arranged relays are supposed to be best suited for. This is because manufacture variations and capacitor imprecision can alter the frequency response of high Q relay systems. When this inconsistency emerges, spatial tuning may be used for efficiency improvement. In summary, when deciding for the optimal configuration for one loading condition, both linear shaped and cluster relays should be considered.

Figure 5.8: Optimal relay configuration based on experimental results at each receiver location, when a receiver is placed 4 cm and 0 cm from the transmitter plane respectively.

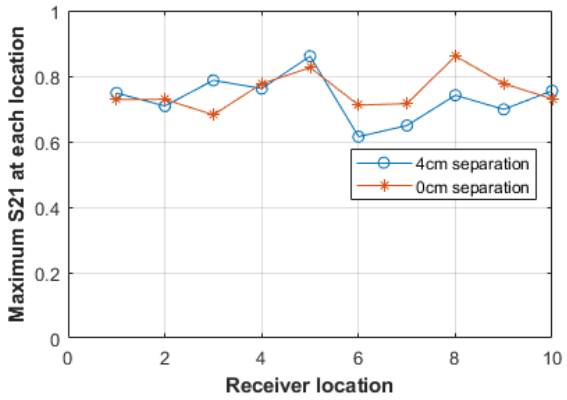

Figure 5.9: $|S_{21}|$ measured at each location with selected optimal relay configurations in Figure 5.5

5.3 Design of 2D Relay Transmitter Geometries

5.3.1 Coverage area extension with planar relays

In this section, we explore the advantages and drawbacks of using 2D reconfigurable relay transmitter to extend wireless power transfer coverage. The relay transmitter is compared with a single loop-coil transmitter on both range extension in coplanar dimension and vertical dimension.

To determine the conditions when it is better to use relay transmitters instead of single large transmitter, we compare relay transmitters with different number of hops to single transmitter with equivalent sizes as the vertical distance between receiver and transmitter increases. At the same time, we want to observe the range extension performance of relays when the receiver is much smaller than the unit relays. We define the ratio between the radius of the unit relay and the receiver as **unit-relay-Rx ratio**. The $|S_{21}|$ of the relay transmitter is calculated with Eq.3.1, Eq.3.3 and Eq.3.4. The equation used for calculating $|S_{21}|$ of single coil transmitters is for the condition when the receiver moves vertically along the coaxial path of the transmitter, which receives the maximum efficiency in that plane of separation distance. Because the efficiency of the relay transmitter is modeled at the edge of the relay while that for the single coil transmitter is modeled for its best condition, the comparison result is very conservative and more convincing.

First, we model a relay transmitter to have its unit cell relay the same size as the receiver, resulting the unit-relay-Rx ratio of 1. By constructing the relay transmitter with 1, 2 and 3 hops, we form the transmitter plane with diameters that are 3, 5 and 7 times the receiver diameter. The radius of the single transmitter is determined by the effective radius of the relay transmitter, which is shown in Eq.5.1.

$$r_{eff} = (\#hops \cdot 2 + 1) \cdot r_{relay} \tag{5.1}$$

where r_{eff} is the radius of the effective coverage area of the relay plane, $\#hops$ is the number of relays that connect the primary relay to the edge of the plane with the shortest straight

line, and r_{relay} is the radius of the each unit relay.

Figure 5.10a-c show the $|S_{21}|$ of the relay transmitter and the single transmitter with three different coverage areas, where the unit relay cell is constructed to be the same size as the receiver coil. The single coil transmitter is better when the Tx-Rx ratio is 3 and 5. When the Tx-Rx ratio is increased to 7 and the vertical distance is from half to one receiver diameter away, the relay transmitter is more efficient.

Next, we compare the same transmitters with a smaller receiver to characterize systems with larger unit-relay-Rx ratio (Figure 5.10d-e) and therefore larger Tx-Rx ratio. The second test setup has a unit-relay-Rx ratio of 2.8. The $|S_{21}|$ with the smaller receiver is worse than those with the bigger receiver, when measured with the same transmitter, due to a smaller Q and larger Tx-Rx ratio. However, the advantage of the relay transmitter is more obvious when Tx-Rx ratio is 14 and larger. When Tx-Rx ratio is 19.6, the maximum $|S_{21}|$ received with the relay transmitter is more than two times larger than with the single transmitter. In summary, the relay transmitter has higher efficiency than single coil transmitter when large Tx-Rx ratio is required. The threshold of the ratio of when a relay array transmitter is preferred depends on both transmitter and receiver coil geometry.

To further characterize the difference between the two configurations on coverage area extension and vertical range, Figure 5.11a-b plot the peak $|S_{21}|$ that each configuration can achieve with given Tx-Rx diameter ratio. Figure 5.11c-d show the vertical range difference where $|S_{21}|$ is within the -3dB range of the peak $|S_{21}|$.

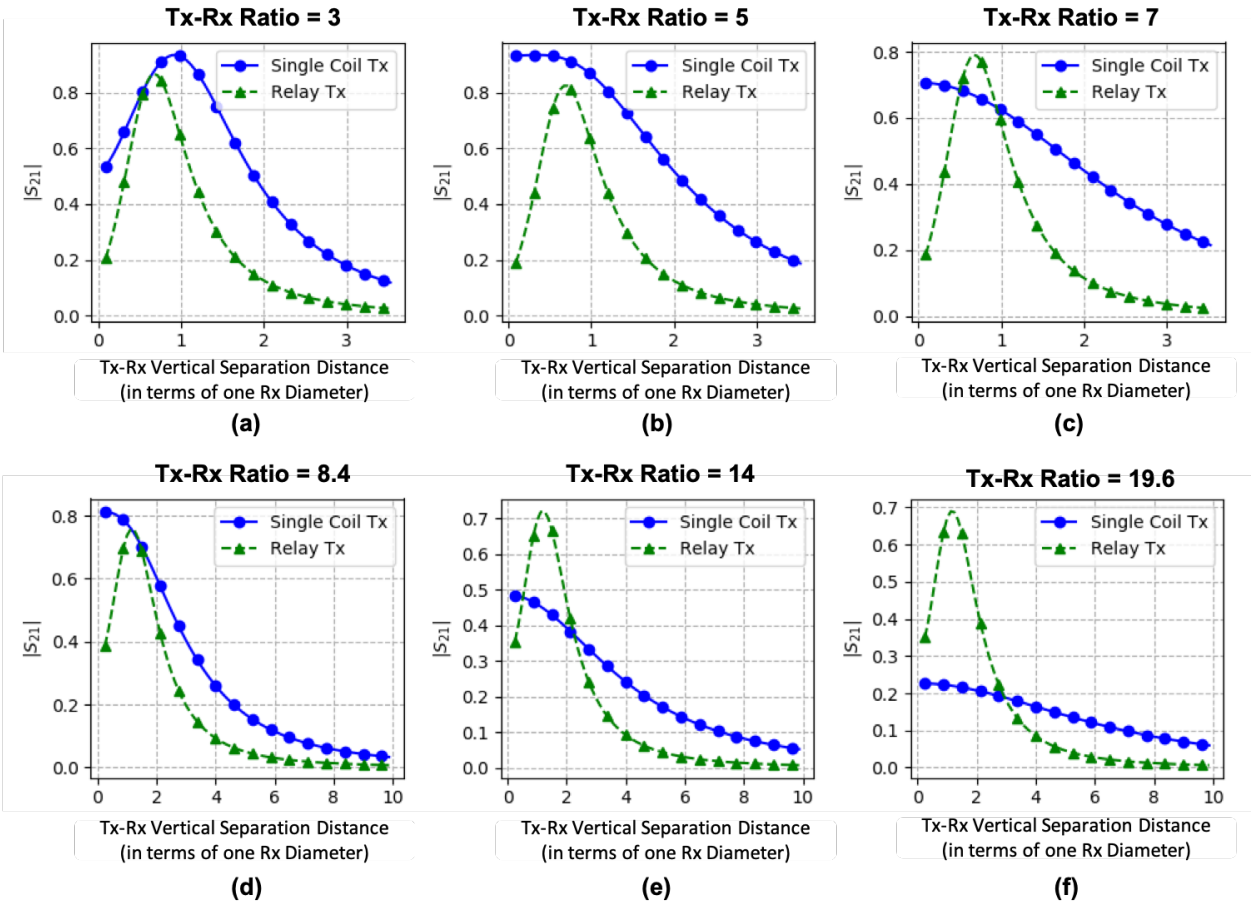

Figure 5.10: Comparing $|S_{21}|$ between single coil transmitter and relay transmitter with different coverage area, different vertical range, and different receiver size. The relay transmitter in plot (a), (b), and (c) are constructed with relays that are the same size as the receiver with 1 hop, 2 hops, and 3 hops respectively. The diameter of the receiver used in the top row is 5.6 cm. The relay transmitters in the second row are the same as ones in the first row, but the receiver used is smaller which has diameter of 2 cm.

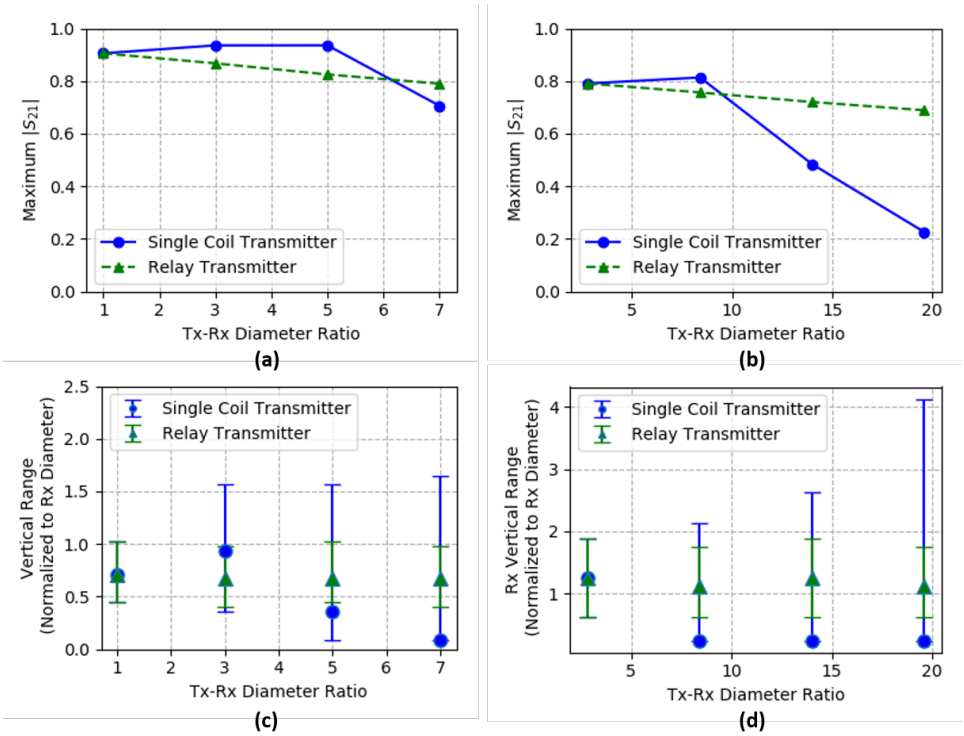

Figure 5.11: (a) and (b) shows the peak $|S_{21}|$ can be achieved with given Tx-Rx diameter ratio and coil geometries. The markers in (c) and (d) indicate the separation distances where the peak $|S_{21}|$ occurs and the bars indicate the range of vertical distance where $|S_{21}$ is within -3dB from the peak value. The result of (a) and (c) used the receiver that has the same geometry as the unit relay which has a 5.6 cm diameter, and that of (b) and (d) used the receiver with 2 cm diameter.

From the plots, we can infer several characteristics of the relay system and the single coil system:

- The peak transmission efficiency of adding additional hops to extend the coverage area to a relay system decreases much slower than increasing the size of a single coil transmitter.

- For system that needs coverage area larger than maximum Tx-Rx ratio, choosing relay system is better in efficiency improvement.

- The efficiency reduction of the relay system is faster than the single coil transmitter system as the receiver moves further away from the transmitter plane.

- For the same receiver and relay transmitter, the efficient vertical range stays mostly constant among different number of hops.

Thus, to design a relay system, we need to setup a model and metric to optimize the number and the size of the relays.

5.3.2 Choosing the Relay Size

Last section described the characteristics of efficiency change as number of hops are added with different unit-relay-Rx ratio. This section discusses how to choose the size of relays. To cover a fixed area with tessellated relays, the larger the unit relay is, the less the number of total relays is needed. The geometric parameters of relays directly contribute to the Tx loop-coil parameter A defined in Eq. 3.12 in Section 3.4.3 and the required number of relays n. Therefore, it directly affects the end-hop-gain according to Eq.3.16. While the end-hop-gain is an important measure on how efficient the range extension capability of the relay system is, it does not measure the uniformity the power distribution is. Depending on user applications, these two parameters can be equally important. This section first talks about

how to choose the relay size to maximize end-hop-gain, then it discusses the uniformity aspect that will result in a figure of merit which takes both parameters in consideration.

If the design goal of the relay system is to maximize the coverage area and the receiver can be very close to the TX plane, the size of the relay coil should be chosen as the size whose frequency splitting caused by over coupling just starts to disappear with the receiver being very close. If the receiver has some clearance requirement from the TX plane, the relay size should be chosen to be the largest that gives the highest $|S_{21}|$ to the receiver at a given clearance distance. Even though coils with the same outer diameter can be made with different Q based on its geometry, here we assume the coils are designed with the highest Q for a given diameter. For either case, the number of relays needed are the number that can fill the intended area with the selected unit relay, where the relays are spaced by their critical coupling distance with their neighboring coils.

For example, if we are to design a relay transmitter that targets to deliver power to a receiver that is 2 cm in diameter with a minimum transmitter-to-receiver clearance 2 cm, and the diameter of the transmitter can be no more than 45 cm, the process is split into the following steps. Firstly, the relay size options are calculated based on number of hops. They are 15 cm, 9 cm, 6.5 cm, 5 cm for 1-hop, 2-hop, 3-hop, and 4-hop, respectively. Then we pick the relay size that has the largest $|S_{21}|$ with the given receiver and given clearance.

Figure 5.12 shows the simulated $|S_{21}|$ relationship between each relay option and the receiver at various separation distances. It gives an insight of choosing the optimal relay size with given receiver clearance requirement. Because the minimum clearance is 2 cm, we pick the relay size of 6.5 cm, which has the highest $|S_{21}|$ at 2 cm separation distance. This results in a 2-hop relay transmitter to cover an area of 45 cm. The largest end-hop-gain that can be achieved with this configuration can be estimated with Eq.3.16. Figure 5.13 compares the result of $|S_{21}|$ if different relay sizes are selected for the same coverage space. The result shows that with the same overall transmitter size, the 1-hop, 2-hop, and 3-hop relay transmitters are all better than the single coil transmitter at delivering power to a small receiver of 2 cm. The 2-hop transmitter is better than the 1-hop when the receiver is situated

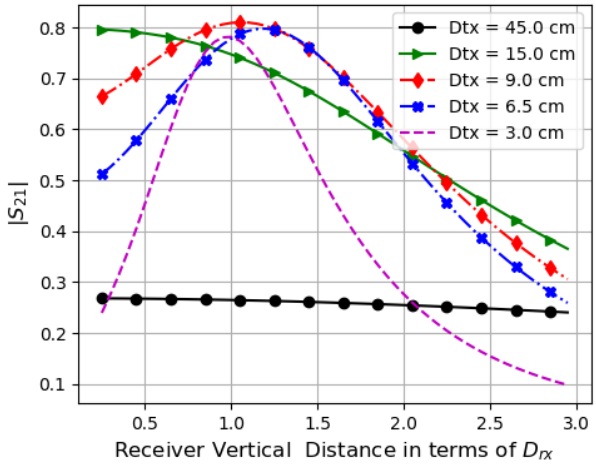

Figure 5.12: $|S_{21}|$ with single coil transmitter of different sizes to a function of receiver and transmitter vertical distance. Dtx represents the diameter of each tested single coil transmitter. The receiver has diameter of 2 cm.

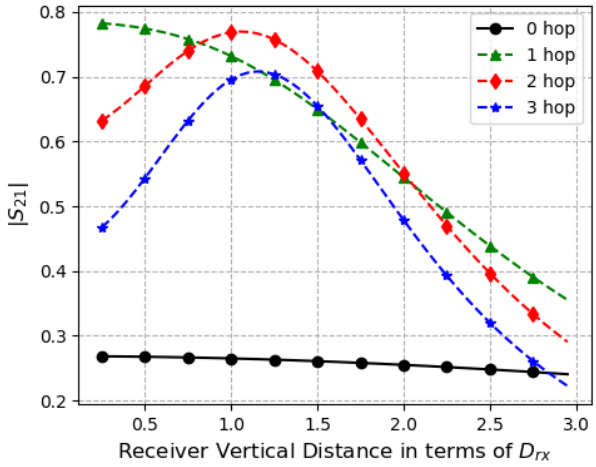

Figure 5.13: $|S_{21}|$ with relays transmitters that are same in coverage area (45 cm in diameter) but different unit relay sizes. The diameter of the unit relay is 15 cm for the 1-hop case, 9 cm for the 2-hop, and 6.5 cm for the 3-hop.

away from the transmitter plane three quarters to two times of the receiver diameter. The 1-hop transmitter is better when the receiver is closer to the transmitter plane.

Another aspect that relay size affects is power transfer uniformity. Because the transmitter to receiver coupling decreases as the two coils are more misaligned, the efficiency along the path where a small receiver moves across a large transmitter is not uniform. Even though there are methods to improve the uniformity of a coil, it has its limit [11]. Because it is hard to have a general characterization of the uniformity without including specific coil geometry, optimizing uniformity is not directly in the model of designing the relay system. Thus, in order to quantitatively evaluate the relay system and help with guiding the design decisions, we have developed the FOM that includes the uniformity factor in addition to average efficiency, coverage area and vertical range in Eq.5.2.

$$FOM = S * H * P * (1 - CV) \tag{5.2}$$

where S stands for the coverage area of the relay transmitter normalized with receiver area, P represents the average efficiency achieved when the receiver is moving on the plane with intended test separation distance, H stands for the vertical separation distance when the receiver gets the best average efficiency, which is normalized to the diameter of the receiver, and CV is the coefficient of variation of the efficiency collected at all the locations. Thus, a wireless power transfer system with a high FOM demonstrates the ability to deliver power uniformly to a receiver over a large area with high efficiency at a long range.

5.4 Design of Switchable Coils

To control the active relay pattern, we chose to use a digitally controlled switch to enable or disable each individual relay. Because the Q of relays plays a large role in coil efficiency, we want to introduce minimal resistance when we enable each relay. Also, we want to completely remove the impact of a relay when it is deactivated. However, because digitally controlled switches have limitations such as parasitic resistance and capacitance, breakdown voltage

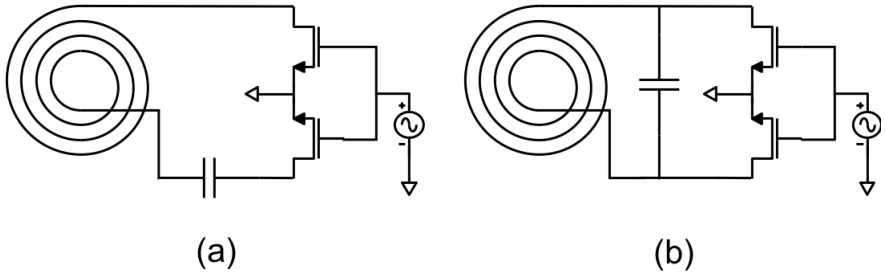

Figure 5.14: Illustration of two switchable coil configuration options. (a). Switch is in series. (b). Switch is in parallel

limit, switching speed limit etc., we have to design the switching circuit according to these criteria.

Most analog switches do not meet this requirement, so we choose to use MOSFETs. Because each relay resonator does not connect to the ground, or any signal source directly, we use the configuration of a pair of MOSFETs instead of a single one to enable and disable the relay as shown in Figure 5.14. There are two possible configurations. One is having the switch serially connected to the resonator (Figure 5.14 a). When the switch is on, the relay is activated and the switch introduces additional resistance. The other one is to have the switch connected in parallel to the tuning capacitor (Figure 5.14 b). When the switch is off, the relay is active, and the switch introduces additional capacitance in parallel to the tuning capacitor. Even though we do not want to introduce resistance with serial connection when the relay is active, the voltage swing across the parasitic capacitor in a high Q resonating coil can easily exceed the breakdown voltage of the switch. Thus, the serial connection configuration (Figure 5.14 a) is chosen and the switching section should have an on-resistance as low as possible. Additionally, because the deactivated switch has an output capacitance, the switch has to be selected whose output capacitance is much smaller than the tuning capacitor, so it can move the resonant frequency of the relay off the operating frequency enough to act as a de-activated relay.

In addition to low on-resistance and small output capacitance, we also need the breakdown voltage of the switch to be high. Even though the serial configuration avoids high voltage swing stress across the switch when the relay is active, it still applies a short period of voltage swing across the switch after the MOSFET is switched off due to the energy stored in the high Q resonator.

The higher the Q is, the longer the resonator will resonate. The higher the transfer power is, the larger the amplitude of the resonation. The relationship of energy decay in a resonator with Q_{off} is shown in Eq.5.3, where Q_{off} is the quality factor of the coil after the switch is turned off.

$$E = E_0 e^{-\frac{\omega_{off} t}{Q_{off}}} \tag{5.3}$$

E_0 is the initial energy stored in the resonator, and ω_{off} is the new resonant frequency after the switch is turned off. The time it takes for the resonator to deplete energy is equal to 5τ, where τ is the time constant of each resonator represented in Eq.5.4.

$$\tau = \frac{Q}{\omega_0} \tag{5.4}$$

After the instantaneous spike caused by the switching action, the voltage across the switch is shown in Eq. 5.5, where V_C is the voltage across the capacitor while the relay in enabled.

$$V_{switch} = V_C \cdot \frac{C}{C + C_{switch}} \tag{5.5}$$

Thus, the most qualified switch has to meet the voltage breakdown requirement of not exceeding the voltage V_{switch} is deactivated for a period of 5τ.

In summary, the switch needs to have a low on-resistance that ideally is smaller than the parasitic resistance of the resonator itself, a small output capacitance that is smaller than the tuning capacitor, and a high voltage breakdown limit that can tolerate V_{switch} for the intended WPT power level.

5.5 Power Steering Algorithm for CARR system

We have talked about the motivation of reconfigurable relays, the design suggestions on relay geometries, and optimal configurations with various receiver locations. This section

talks about the algorithms in determining the control of enabling and disabling relays based on receivers' positions.

With individually switchable relay array, the activated relays can be selected to form any intended shape such as straight line, curved line, or any cluster combinations. To accommodate conditions with different receiver motion patterns and multiple receivers, we design two operation modes: *broadcasting mode* and *receiver tracking mode*. With broadcasting mode (Section 5.5.1), the power is distributed everywhere on the transmitter regardless of receiver position. Receiver tracking mode sets the instructions to reconfigure relays based on receiver position, which makes power steering more focused and specific.

5.5.1 Broadcasting Mode

The broadcasting mode continuously enables each combination of relay coils with time multiplexing, so the receiver can always get power at any location on the plane. Thus, the operation tasks are divided into two major steps: divide the coverage space into small sections, for each divided section find the optimal relay configuration for it, and lastly turn on and off each selected relay configuration one by one with equal on time.

The power expected to be received at each location under this mode can be estimated with Eq.5.6, where P_r is the receiver power with the relay configuration selected for that location. Because more than one relay configurations may deliver power to the same location, the average received power P_{ra} is expected to be larger than the estimated value in Eq.5.6.

$$P_{ra} \approx \frac{P_r}{number\ of\ combinations} \tag{5.6}$$

Because each relay is enabled at different time, multiple receivers can be charged at the same time with P_{ra}. In fact, the algorithm behaves the same whether there is single receiver or multiple receivers, so that such a algorithm is straightforward to implement. With more receivers added to the system, the total efficiency of the system will increase. Because it does not need feedback as input to the algorithm, the hardware required is less complicated, which reduces the cost. However, the drawback is that the greater number of relay configurations

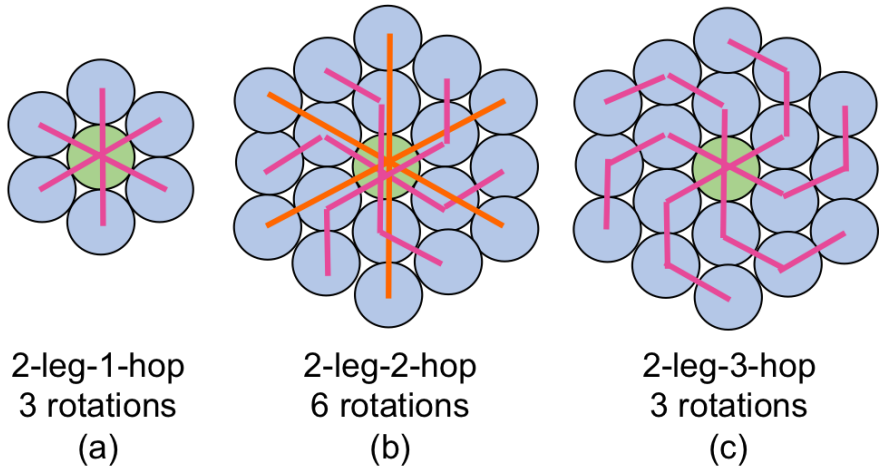

Figure 5.15: Examples of reconfiguration plans with broadcasting mode with the middle-driven strategy.

are, the less average receive power (P_{ra}) is at each location. Because P_{ra} changes as a function of the number of scanning combinations, keeping P_{ra} constant as the number of relays increases is a challenge. Figure 5.15 shows three examples of reconfiguration plans with the broadcasting mode using the middle-driven strategy.

5.5.2 Receiver Tracking Mode

Rather than providing power everywhere with broadcasting mode, tracking mode tracks the receiver motion and reconfigures the system based on the changing load conditions. The advantage of doing so is this method confines the power within a specific space, which is great from an energy saving point of view, and can also increase the available power at each target location compared to the time-multiplexing method. In this section, we develop control algorithms which meet the goals of high efficiency and fast receiver tracking using the characteristics of the relay array system. We start with finding the parameters for tracking receivers, then we talk about algorithms designed for the single receiver case and the multiple receivers case respectively.

Use of the Reflection Coefficient for Tracking Receivers

A multi-hop system can be regarded as a passive 2-port system, where port 1 is the transmitter and port 2 is the receiver. For efficient power transfer, the goal is to optimize $|S_{21}|$. However, $|S_{21}|$ would be very difficult to practically measure during system operation, as it requires additional instrumentation on both transmitter and receiver. To address this, we propose use S_{11} as a proxy for $|S_{21}|$. Because reflection coefficient (Γ), which is equivalent to S_{11} when the load and source impedance are matched, can easily be measured from the transmitter side, this would greatly simplify system topology. When there is a receiver moving on top of the relay array, the change of impedance causes a change in the reflected signal. As an added benefit, the change of $|S_{11}|$ happens instantaneously with the change in load condition, making the tracking inherently fast.

We use the well-known rule that the sum of $|S_{21}|^2$ and $|S_{11}|^2$ is no more than 1 for a passive 2-port system as seen in Eq.5.7.

$$|S11|<= \sqrt{1-|S21|^2} \tag{5.7}$$

From Eq.5.7, large $|S_{21}|$ implies small $|S_{11}|$, but small $|S_{11}|$ does not necessarily mean large $|S_{21}|$. To show that this converse relationship is also generally true, we compare actual $|S_{11}|$ measurements at various receiver locations with corresponding $|S_{21}|$ measurements. We first compare the two with 1D relay array, and then we add cluster relay arrays in the comparison as well.

Figure 5.16 shows the relay array and the tested area that are divided into five receiver locations. The relays are configured into three options at each location. Figure 5.17a shows the corresponding S parameter results when a receiver is separated by 4 cm, the location that makes the input impedance of the multi-hop network 50 Ω. At each location, the configuration that has the minimum $|S_{11}|$ has the maximum $|S_{21}|$. However, we are not able to detect the receiver position by merely finding the relay configuration with the minimum $|S_{11}|$ result. This would cause the system to incorrectly settle on a relay configuration with the lowest $|S_{11}|$, even when no receiver is present, rather than continuing to search. Also,

this method doesn't work when there is more than one receiver in the system, as the global minimum $|S_{11}|$ will only identify one of the receivers.

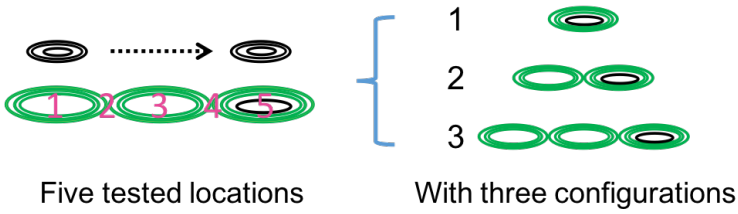

Figure 5.16: Test setup for S parameters measurement with 1D relay array.

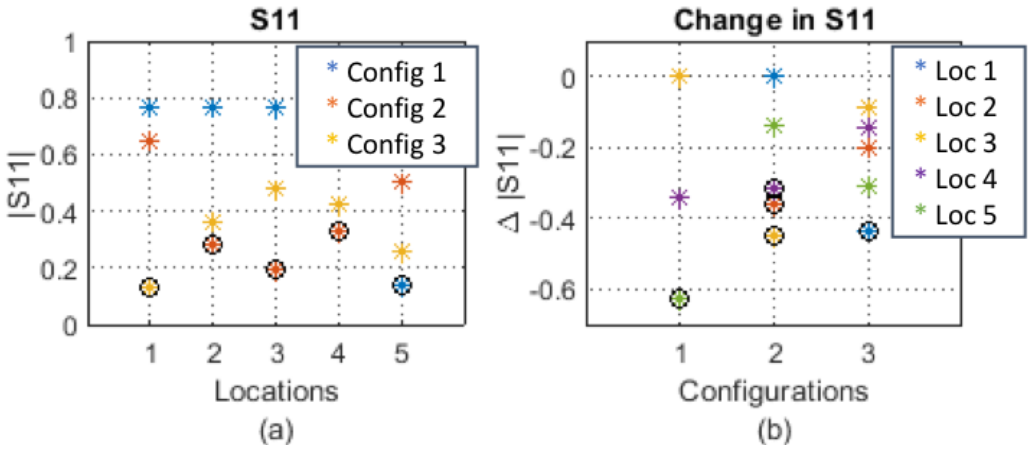

Figure 5.17: (a). $|S_{11}|$ measured across three relay configurations, with receiver placed at each of five test locations. (b). Change in $|S_{11}|$ seen with each configuration when a receiver is present at each of the five test locations. The circled data in both (a) and (b) are the data points where maximum $|S_{21}|$ was observed, representing best efficiency. Note that test cases where $|S_{11}|$ is lowest, or changed the most, correlate with the best $|S_{21}|$ values and thus best power delivery to the receiver.

One approach to resolve these issues is to use the change in $|S_{11}|$ as an indicator of a receiver's presence. Figure 5.17b shows the change in $|S_{11}|$ seen by each configuration when a

receiver is present at each of the five test locations. If the change in $|S_{11}|$ from some baseline value exceeds a threshold for a particular configuration, we decide that the receiver must be powerable via that configuration. However, because the amount of change in $|S_{11}|$ (Figure 5.17b) is different for different relay configurations, receiver locations, and receivers, optimizing tracking accuracy would mean tediously characterizing all possible loading conditions to determine the threshold setting for each configuration. In summary, this algorithm is fast during run time operation but requires prohibitively complex prior calibration of the system.

To observe whether the same trend of S parameter relationship applies to system with cluster relays. We setup another test case where both 1D relays and cluster relays are included in the test configurations. Figure 5.18 shows the test setup and locations, and the relays are configured into eleven option. Figure 5.19 shows the $|S_{11}|$ results when a receiver is vertically separated from the relay array by 4 cm, the location that makes the input impedance of the multi-hop network close to 50 Ω.

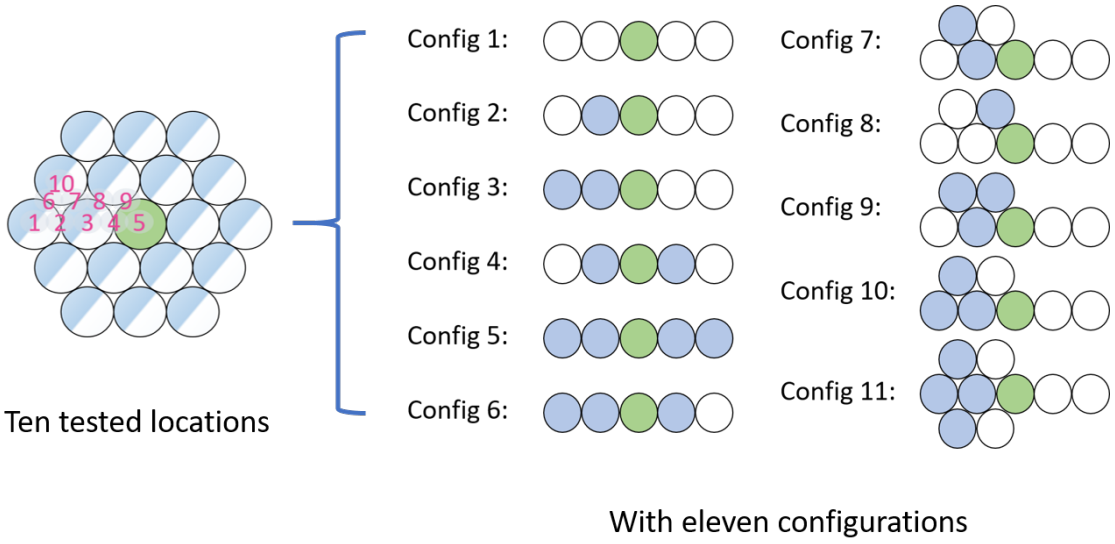

Figure 5.18: Test setup for S parameters measurement with 2D relay array.

At each location, the configuration that has the maximum $|S_{21}|$ does not always have the minimum $|S_{11}|$. This is different from the observation with the 1D relay case, but it reassures

that minimum $|S_{11}|$ is not suitable for use as the decision parameter of the power steering algorithm.

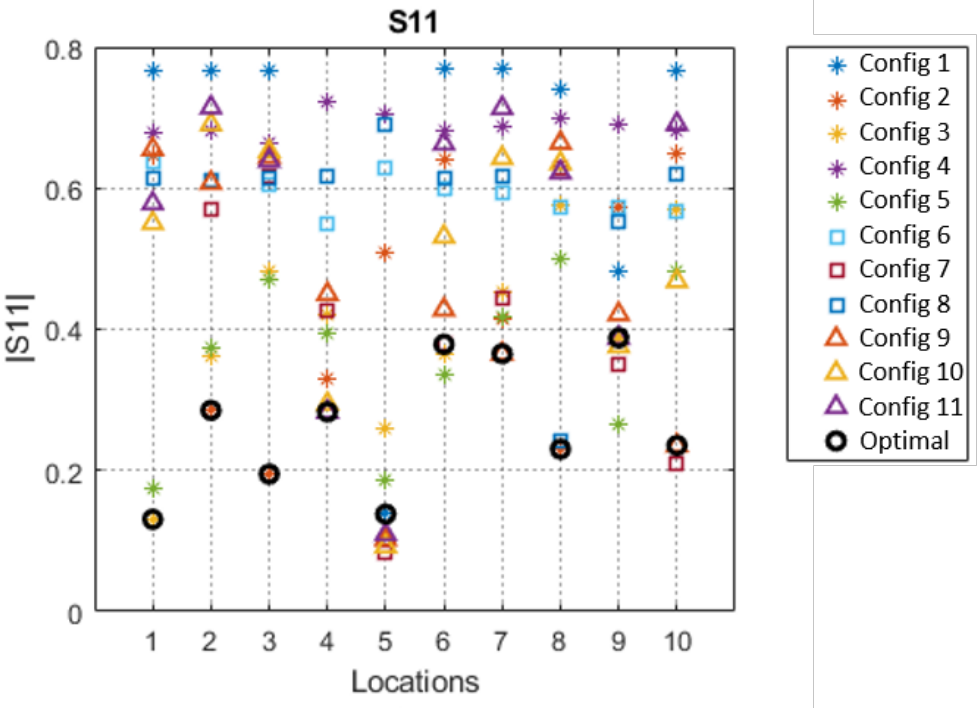

Figure 5.19: $|S_{11}|$ measured across eleven relay configurations, with receiver placed at each of ten test locations (Figure 5.18). The circled data are the measurements where maximum $|S_{21}|$ was observed, representing the optimal efficiency.

Next, we observe the change in $|S_{11}|$ with the cluster relay system. Figure 5.20 shows the change in $|S_{11}|$ with each relay configuration in each test location. At each location, the configuration that has the largest change in $|S_{11}|$ has the maximum $|S_{21}|$, and the amount of change at each location is different. The system with cluster relays has the same property of the change in $|S_{11}|$. Thus, change in $|S_{11}|$ is a good candidate to be used as decision parameter of the receiver tracking algorithm. Due to the difficulty of measuring $|S_{11}|$ in real time of a wireless power transfer system, we instead use the reflection coefficient which is

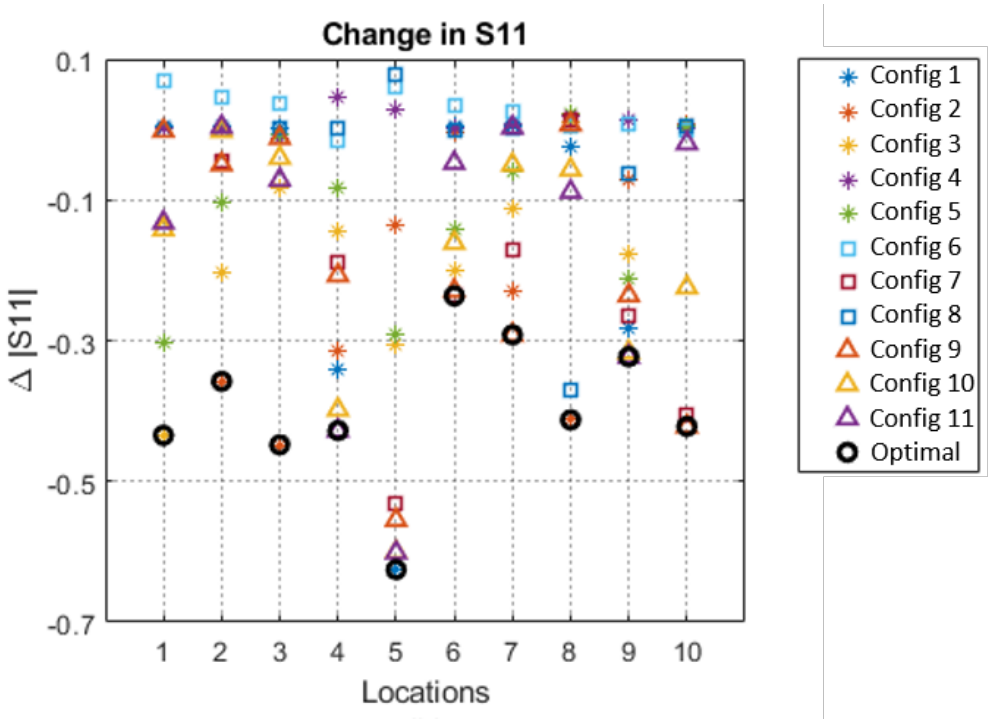

Figure 5.20: Change in $|S_{11}|$ with eleven relay configurations, when the receiver is placed at each of ten test locations (Figure 5.18). The highlighted data with black circles are the data points where maximum $|S_{21}|$ was observed, representing optimal efficiency.

equivalent to S_{11} when the source and load impedance are matched.

5.5.3 Description of the Power Steering Algorithm for Single Receiver Case

Based on the above insights, we propose a tracking algorithm consisting of three sequential tasks: **calibration**, **rough-scanning** and **focused-scanning**.

1. The **calibration** process can take place once after manufacture of the relay array, or on each system boot. In calibration, the reflection coefficient (Γ) value of all selected relay configurations are measured one-by-one and saved as system calibration values.

2. During normal operation, the **rough-scanning mode** is the way each receiver search

cycle starts. In rough-scanning, we switch between a prioritized set of possible configurations until we detect a change of Γ from the calibration value. The threshold of change detection is small. The first configuration in which a change in Γ is detected is called the **pilot configuration**.

3. The configurations that share *any one* of the unit relays in the pilot configuration are referred as the **related configurations**. After the pilot configuration has been identified, we enter the **focused-scanning mode**, where we switch between all the related configurations and select the one with the largest change in Γ for the detected receiver. The selected relay configuration is used for power steering.

Possible configurations used in the rough scanning modes are selected with the optimal configurations selected for all the locations on the plane. However, as the number of configurations used in rough-scanning becomes larger, the tracking speed becomes slower. So even though the cluster relays are better than 1D relays under certain conditions, possible configurations do not include cluster relays for tracking speed optimization, because a related 1D relay that shares some mutual relays with the cluster relay can also see change in Γ when load condition that is not optimal. Cluster relays are only used during the focused-scanning mode as the related configurations.

To Prioritize possible configurations means that the order of trying different relay configurations is ranked based on power efficiency and the likelihood of detecting receiver successfully. To minimize the power consumed while scanning for a receiver, we prioritize the types of patterns used in scanning based on a consideration of the power amplifier characteristics and system input impedance. Because the class E power amplifier, which is commonly used in the wireless power transfer system, is designed for a specific output impedance, mismatch of load impedance with the power amplifier output impedance results in efficiency reduction. As the input impedance of 1D relay arrays changes as the number of hops changes, the algorithm should prioritize the 1D relay arrays that pull less power because the power consumed in the scanning stage is wasted. If the input impedance does

not contribute significantly for the intended power amplifier, one should elect to prioritize the relay configurations with more hops, which are more likely to detect receivers with larger coverage.

5.5.4 Description of the Power Steering Algorithm for Multiple Receivers Case

Unlike the algorithm designed for a single receiver in which the end of rough-scanning is triggered when there is significant change in the reflection signal, the algorithm for tacking multiple receivers needs to scan the entire plane to know how many receivers there are as the first step before entering the focused-scanning mode to locate receivers.

The tracking algorithm for multiple receivers consists of four sequential tasks: **calibration**, **rough-scanning** and **focused-scanning**, and **duty-cycle power steering**.

1. The **calibration** process is the same as the one for the single receiver case. It can take place once after manufacture of the relay array, or on each system boot. In calibration, the reflection coefficient (Γ) value of all selected relay configurations are measured one-by-one and saved as system calibration values.

2. During normal operation, the **rough-scanning mode** is the way each receiver search cycle starts. In rough-scanning, we switch between a set of possible configurations and store every configuration which detects a change of Γ from the calibration value. The threshold of change detection is set small. After finishing searching the whole set, if there are no saved configurations with change of Γ, the rough-scanning is restarted with a new round of searching. The saved configurations are called **pilot configurations**.

3. The configurations that share *any one* of the unit relays in the pilot configuration are referred as the **related configurations**. If any pilot configuration a is the related configuration of another pilot configuration b in the same search round, we define the set C that is the union of A and B as **one search partition**, where A is the set of related configurations of a and B is the set of related configurations of b. If a pilot

configuration is not related to any other pilot configurations, the related configuration set of its own is considered as one search partition. After all the search partitions have been identified, we enter the **focused-scanning mode**, where we find one relay configuration with the largest change in Γ in each search partition, and define it as a **target configuration**.

4. After all the target configurations have been elected, the system enters the **cycling mode**. In this stage, we cycle the configuration of the relays between the target configurations. By configuring the relay transmitter to one target configuration for longer time, we can increase the power delivered at that location.

Rather than locating the specific location of each receiver, the transmitter finds the largest change in Γ, which effectively tries to deliver power with the optimal efficiency. Thus, even when two receivers are placed closely, which results in a state that is hard to locate and differentiate between them, the result of the target configuration is selected such that the net efficiency is optimal.

5.5.5 Conclusion

Three power steering algorithms are introduced in this section: broadcasting mode, single receiver tracking mode and multiple receivers tracking mode. The broadcasting mode distribute power everywhere on the plane by time-multiplexing between different relay configurations so it can support multiple receivers without needing to worry about the interference among the receivers. Both receiver tracking modes track the receiver position and reconfigure relays accordingly. The receiver tracking mechanism is based on monitoring the change of the reflection coefficient at the output of the power amplifier. The single receiver tracking mode is optimized for the single receiver case so it is faster than the multiple receivers tracking mode.

5.6 Prototype Implementation and Evaluation of a CARR system

5.6.1 Implementation

We have proposed a reconfigurable multi-hop relay transmitter system that is centrally controlled as shown in Figure 5.21. In order to validate the design of the system, a prototype is implemented as shown in Figure 5.22.

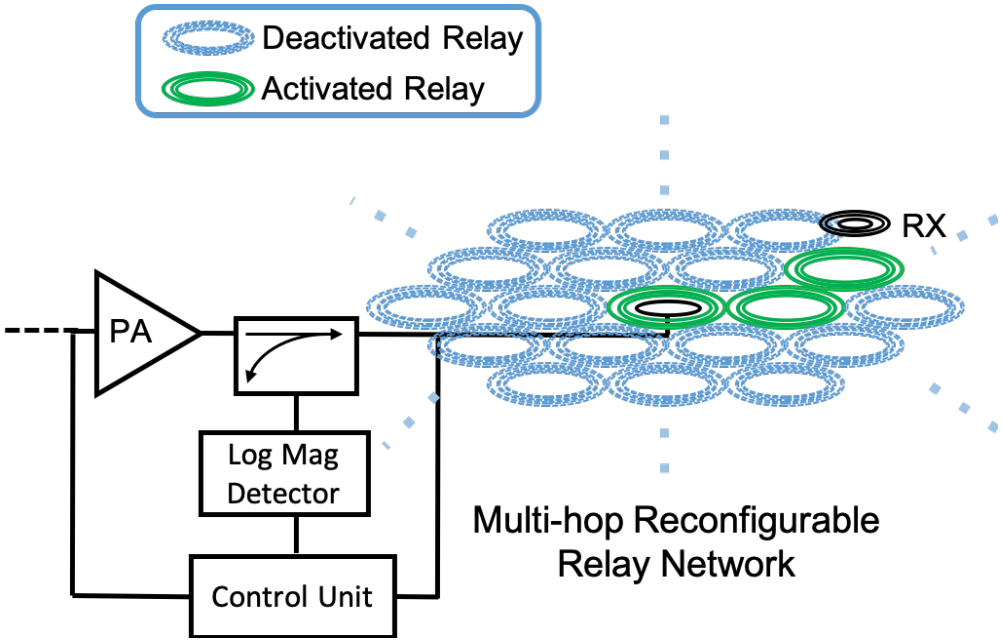

Figure 5.21: Illustration of a planar reconfigurable relay wireless power transfer system.

The relay transmitter prototype consists of two parts: a reconfigurable relay board and a relay control board. The relay board is implemented on a four-layer FR4 PCB, has nineteen hexagonally arranged coils. Each coil has five turns and is 59 mm in diameter. Each pair of adjacent coils are slightly overlapped to approach the optimal coupling condition concluded in Chapter 3. We choose to use a maximum of 2 hops between the primary coil and the edge of the board with the shortest path. As a result, it is 29 cm in diameter at its widest point.

The driven loop is mounted under the center coil of the board, and is connected in series

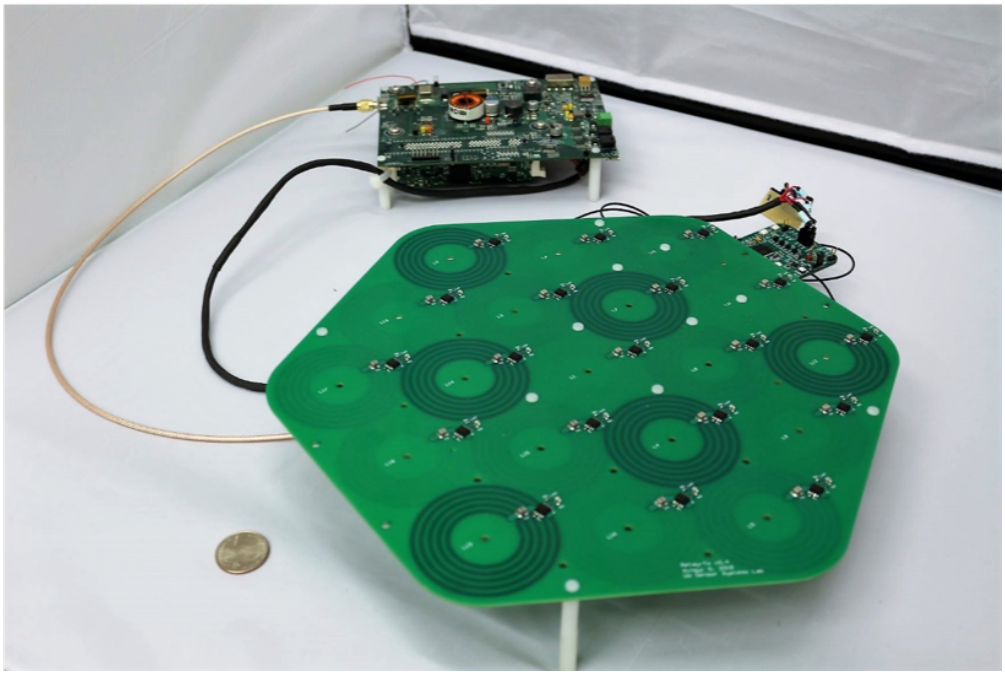

Figure 5.22: Hardware prototype of a centrally controlled relay transmitter system.

with a 100 pF tuning capacitor and a pair of BUK7K134-100E MOSFET switches that share a source and gate as shown in Figure 5.23. When the gate voltages are high, the series switches allow current flow and the relay may resonate. When the gate voltages are low, the switches block current flow, pushing the resonant frequency very far from the system's operating frequency and thus effectively shutting off the relay. An RClamp2431TQ transient-voltage-suppression (TVS) diode is connected in parallel with the MOSFET pair to protect the MOSFETs from high voltage spikes caused by each switching action. The control signals that reconfigure all relays are generated by a microcontroller, then level shifted to 10 V. A pull down resistor is placed at the gate to reduce the coupled noise on the control line.

As shown in Figure 5.23, the power signal is provided by an existing power transmitter, the same one used in [41]. It consists of a signal source, and a Class E amplifier designed for a 50 Ω load. At the output of the power amplifier, a SYDC-20-22HP+ directional coupler is connected in series to obtain reflection coefficient that is used in the tracking algorithm. The

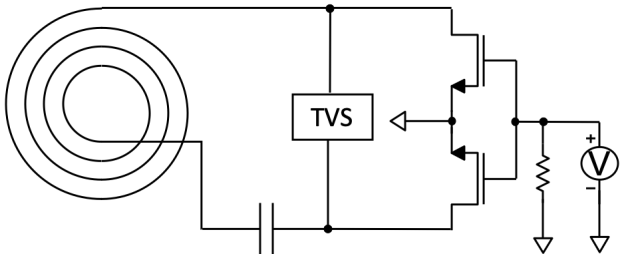

Figure 5.23: Circuit diagram of a reconfigurable unit relays.

reflection coefficient from the coupler is processed by an AD8302 gain and phase detector, and then gain and phase values are sampled by an ADC on a microcontroller. A monolithic RC low pass filter, the ELK-EV333FA, is placed between the detector and ADC to reduce noise at the carrier frequency.

The control algorithm is implemented using the TI MSP432P401R. This microcontroller is chosen because of its fast and high-resolution 1-Msps, 14 bit ADC, which is used to collect samples from the output of the gain and phase detector. For each reflection coefficient data point, seven consecutive samples are taken, and they are digitally averaged to further reduce the impact of noise. The entire controller firmware uses 5.7 kB of MSP432 program memory.

The relay control board contains a button, with which users can switch between different power steering algorithms, which include broadcasting mode, single receiver tracking, and multiple receivers tracking described in Section 5.5. In broadcasting mode, the transmitter switches between eighteen configurations which include twelve 1-leg-2-hop and six 1-leg-1-hop. For both receiver tracking modes, the calibration procedure is triggered once on system power-on and used to provide the baseline reflection coefficient value for each configuration. In the single receiver tracking mode, once a possible receiver has been identified in the rough-scanning mode, the algorithm transitions to focused-scanning mode. At the end of the focused scan the system will remain in the configuration which best targets the receiver. The system continues sampling the reflection coefficient until it observes a significant change,

which may indicate that the receiver has moved. Following the change, the system will return to rough-scanning mode. In the multiple receiver tracking mode, the rough scanning cycle repeats until one or more receivers have been detected, and then the algorithm transitions to focused scanning mode. At the end of the focused scan the prototype knows the configuration(s) that can deliver power to the receiver(s) optimally. The relay transmitter then cycles through these optimal configurations to steer power to receivers at different locations. As before, throughout its operation, the system samples the reflection coefficient until a significant change happens, which may indicate that one or more receivers have moved. This triggers the prototype to reset to rough scanning mode.

5.6.2 Evaluation

To evaluate the reconfigurable relay system, we characterize the performance with regards to efficiency, coverage, and tracking speed, and compare it with a single loop-coil transmitter that was used in [31]. The single transmitter has a diameter of 28 cm. To reflect the improvement in efficiency attained by arranging coils such that the critical coupling relationship suggested in Chapter 3 is approached, we also compare our prototype with an earlier unoptimized prototype where adjacent coil pairs are side by side instead of overlapping.

Two receivers with different sizes are used in the tests to characterize performance as the Tx-Rx ratio and unit-relay-Rx ratio becomes larger. The larger receiver is a five-turn PCB coil with a diameter of 5.5 cm and Q of 125. The smaller one has eight turns, is 2 cm in diameter, and has a Q of 90.

To evaluate the power routing performance of the reconfigurable relay system, for each transmitter and receiver combination we measure $|S_{21}|$ with the receiver placed at different locations above the plane. Figure 5.24 shows the $|S_{21}|$ measurement setup with the smaller receiver and a HP8753ES vector network analyzer (VNA). The receiver is placed at 35 locations across one radial arc of the transmitter with a resolution of one-quarter of the relay spacing in the horizontal plane. The vertical separation distance between each receiver and each transmitter plane is selected to be the critical coupling distance between the primary

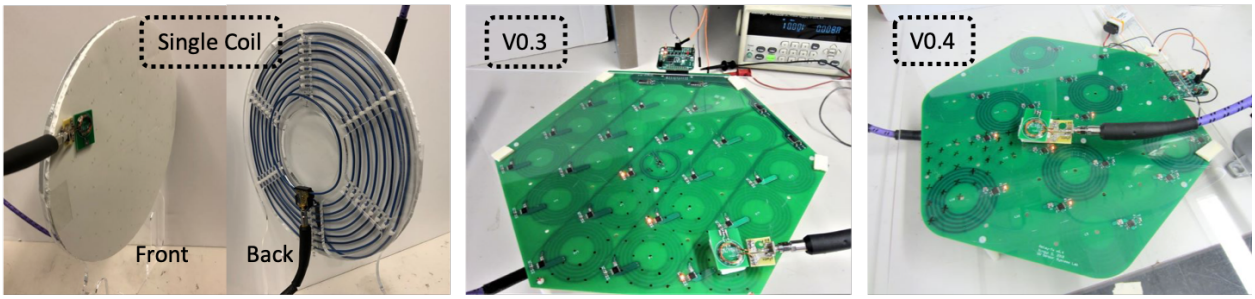

Figure 5.24: (a) The hardware setup for $|S_{21}|$ measurement with a VNA between the single coil transmitter and the smaller receiver with 2 cm diameter. The separation distance is 5 mm. (b) The hardware setup for $|S_{21}|$ measurement with an earlier version of the relay transmitter prototype, v0.3. The separation distance is 1.6 cm. (c) The hardware setup for $|S_{21}|$ measurement with the latest relay transmitter prototype, v0.4. The separation distance is 1.6 cm. The lighted LEDs indicate the activated relays.

coil and the receiver. With the 5.5 cm receiver, the vertical separation distances with the three transmitters are all set to the same value of 4 cm. With the 2 cm receiver, the vertical separation distances with the three transmitters are 5 mm, 1.6 cm, and 1.6 cm, respectively. Results are then extrapolated to the rest of the surface area based on the rotational symmetry of the transmitter.

Figure 5.25 shows the $|S_{21}|$ with the six combinations: single coil transmitter with the larger receiver (a), relay transmitter v0.3 without optimal coupling arrangement with the larger receiver (b), relay transmitter v0.4 with overlapping coils and the larger receiver (c), single coil transmitter with the smaller receiver (d), relay transmitter v0.3 with the smaller receiver (e), relay transmitter v0.4 with the smaller receiver (f).

When the Tx-Rx ratio is small (Figure 5.25 a-c), using single coil transmitter (Figure 5.25 a) gives higher efficiency at the center region but poor efficiency near the edge, and using the relay transmitter with overlapping coils gives a higher overall average efficiency; when the

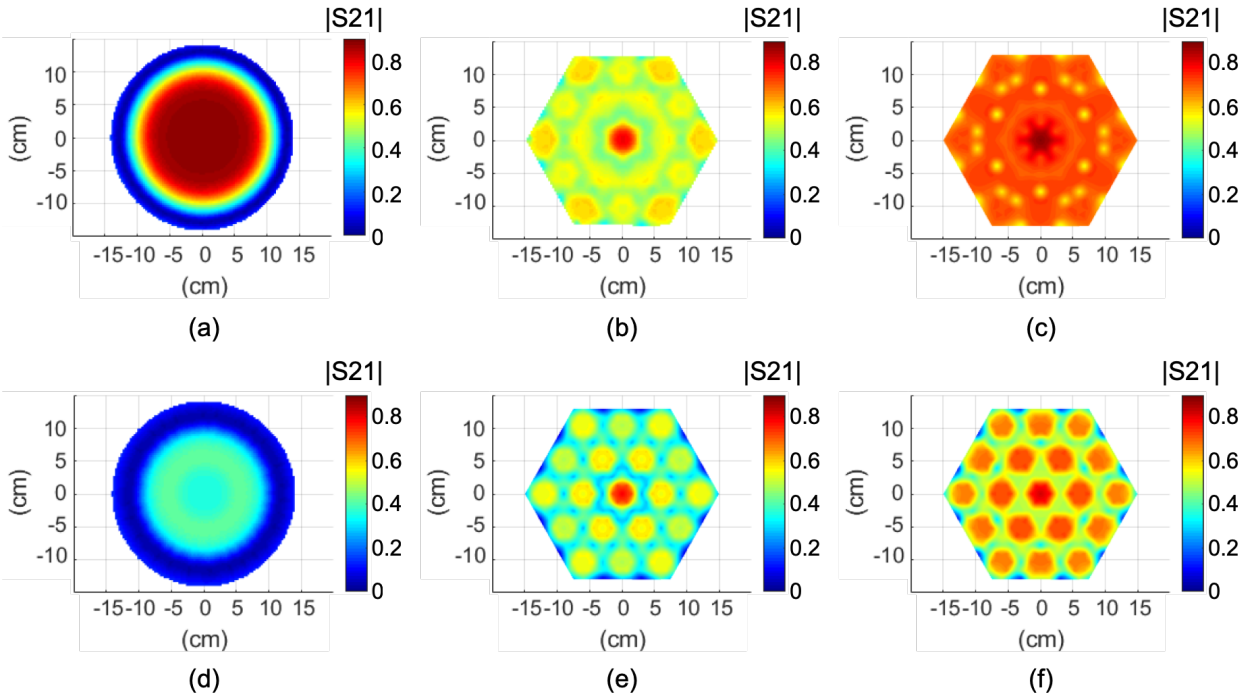

Figure 5.25: Comparing the $|S_{21}|$ between a single coil and two variations of a relay transmitter with similar coverage area. (a), (b) and (c) show the $|S_{21}|$ of the single coil, the relay transmitter v0.3, and the relay transmitter v0.4 shown in Figure 5.24, respectively, with a receiver size that is about the same as the unit relay, which has a diameter of 5.5 cm. (d), (e) and (f) show the $|S_{21}|$ of the single coil, and the two relay transmitters shown in Figure 5.24, respectively, with a 2 cm diameter receiver. The separation distance is 4 cm in (a), (b) and (c), 5 mm in (d), and 1.6 cm in (e) and (f).

Tx-Rx ratio is large (Figure 5.25 d-f), both of the relay transmitters provide better average efficiency than the single coil transmitter, while the relay transmitter with overlapping coils shows an improvement in efficiency. With either receiver, but especially the smaller one, the single coil transmitter becomes very inefficient near its edge, so if a single coil transmitter of this type is to be employed, one should design the transmitter such that the size is larger than the intended coverage area.

In Section 5.3.2, we have defined the FOM for characterizing a wireless power transmitter with respect to its efficiency, coverage area expressed as a ratio between transmitter and receiver area, vertical range in terms of receiver diameter, and uniformity. We evaluate these four setups with the FOM using Eq.5.2 and obtained the result in Table 5.1.

Table 5.1: FOM of the two transmitters

	Single Coil Tx	**Relay Tx v0.3**	**Relay Tx v0.4**
With 5.5cm receiver	3.6	9	13
With 2cm receiver	4.2	53	73

We can conclude that the relay transmitter is exceptionally better than the single coil transmitter when powering small receivers. The relay transmitter with overlapping coils (v0.4) is better than the one with side by side coils (v0.3). The good efficiency near the edge with the relay transmitters improves its average efficiency and uniformity, which in turns makes their FOM higher than the single coil transmitter despite the high peak efficiency with the single coil (Figure 5.25 a-c). In other words, relay transmitters are better than single large coil transmitters at extending the range of WPT with good efficiency and uniformity. As the receiver becomes smaller, power delivery with the relay transmitter becomes more spotty (Figure 5.25 c, f). However, this is offset by the dramatic increase in the coverage area to receiver size ratio.

The speed of locating a receiver is related to how fast the relays can be switched on and off, and the number of paths searched during of the entire scanning process. The rough scanning mode scans the entire search space 2083 times per second. Once a pilot configuration is found, the focused scan takes only 120 microseconds. With this fast-tracking algorithm, power is automatically routed to the receiver as it moves, at a rate faster than the eye can detect.

Chapter 6

LOAD MODULATION WITH HIGH Q RESONATORS

Communication between devices in a wireless power system can be highly useful. For instance, communication from the WPT receiver back to the WPT transmitter could allow the WPT transmitter to identify a particular receiver and understand its power requirements. Load modulation is a low power communication mechanism involving changing the load condition of wireless power receivers in order to produce a reflection detectable at the power provider. The added cost of implementing load modulation in a wireless power system is low, as it can be done as easily as adding a switch to the receiver. Due to this ease of implementation, load modulation is a good candidate system for allowing communication between a WPT receiver and transmitter.

A key design conflict in using load modulation on wireless power system is that, because the resonators are optimized for high efficiency, the quality factor Q is high, which results in lower bandwidth for communication [17]. However, techniques have been developed to work around this limit [49, 7, 8, 6]. On the plus side, load modulation has an irreplaceable capability that other out-of-band communication methods cannot achieve: Load modulation as a communication method takes place via the same channel as the wireless power transfer itself, and only when the two resonators are close enough to transfer power. Thus, with careful design of the load modulation system, we may extract valuable information that other out-of-band radio links cannot. For instance, information about the location of the receiver and how best to deliver power to it may be extracted through the use of load modulation.

This chapter describes a method for implementing a load modulation communication link on a wireless power transfer system, and characterizes the trade-off between efficiency and

communication. It then discusses how to use load modulation to extract location information that is not possible to extract from other communication links.

6.1 Communication Methods for Wireless Power Transfer Systems

Generally, the communication architecture design for a WPT system is based on its application, power requirement, and data rate. Communication solutions can be grouped into two classes: in-band communication and out-of-band communication. In a WPT system, in-band communication refers to using the same antenna, at the same frequency, for both power and communication. Out-of-band communication refers to adding an additional antenna or an additional frequency band for communication purposes, to separate the communication and power link.

One argument for out-of-band communication is given in [17], in which a theoretical analysis of the trade-off between quality factor (Q) of the resonant coupled network (a factor in wireless power efficiency) and achievable communication bandwidth is given. However, the most popular industrial standards for WPT systems, Qi and A4WP, implement in-band communication and out-of-band communication, respectively [3, 2]. Neural implant systems in research have used out-of-band load modulation, modulating an isolated secondary coil instead of the primary coil used for power transfer [38]. These systems have demonstrated high communication rate and low energy per bit [27, 4]. However, this architecture raises the added challenge of eliminating cross-coupling between the power and communication coils [4]. Still others have demonstrated in-band load modulation for neural implants that obtain high data rate and low efficiency degradation [46].

6.2 Load Modulation Performance Analysis

6.2.1 System Overview

The power transmitter is referred to as power host, and the power receiver is referred to as power client. The data link from the power client to the power host is the uplink, and

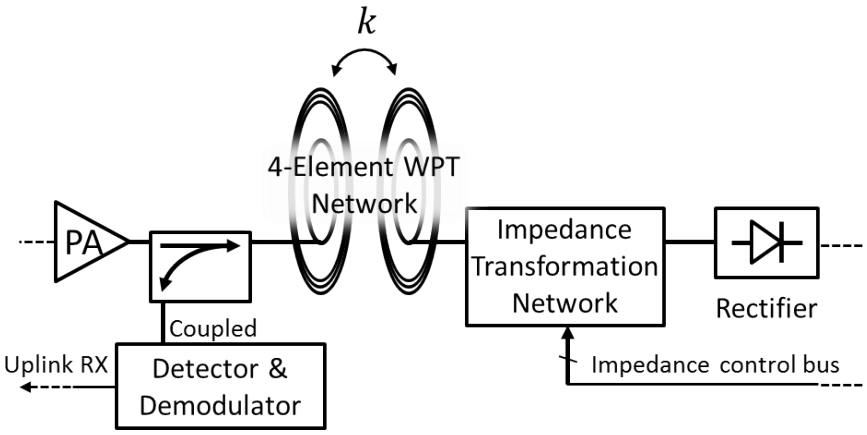

Figure 6.1: A magnetic resonance wireless power transfer system employing load modulation to transfer data from the power client to the power host. The effective load impedance is altered by a controllable impedance transformation network in order to produce detectable changes in the reflected signal.

the link in the reverse direction is the downlink. The power host analyzed here is a near field resonant wireless power transmitter. For high efficiency, it employs a Class E power amplifier. A directional coupler and an In-phase/Quadrature (IQ) demodulator are used as the uplink receiver (Figure 6.1). A four-coil system of magnetically coupled resonators connects the power host and power client. The power client includes a pi-match network with switchable tuning capacitor banks, a full-bridge rectifier, and a load.

Traditionally, to get a clean signal, a load modulation system is often designed to switch between the load impedance states that result in the highest contrast in the reflected signal. Because our goal is to understand the trade-off between load modulation communication capability and WPT efficiency, rather than choosing the highest contrast pair, the modulation is configured to include a range of options, allowing experimentation with both small impedance contrast and large impedance contrast.

Due to the difficulty of serially switching in and out components in an RF system, and the additional challenges of inductor switching, the low pass pi-match network in Figure 6.2 is

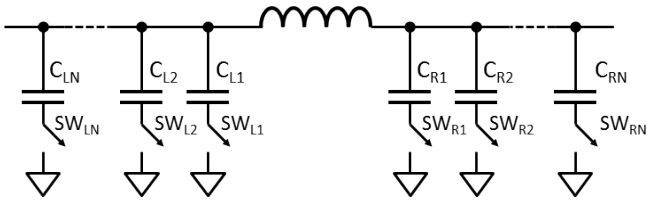

Figure 6.2: The switching pi-match topology allows for a wide range of impedance transformations. One switch configuration will produce the maximal efficiency case Z_{MATCH}, and another will correspond to the load modulation impedance Z_{LM}.

chosen, where the serial inductor doesn't need to be switched. During pure power transmission, the pi-match network transforms the rectifier impedance such that the PA experiences a conjugate match to the transmit coil, resulting in maximum power efficiency. When doing load modulation, our topology simultaneously switches in and out capacitor or capacitor pairs on both sides of the pi-match such that the resulting load impedance experienced by the PA moves between the matched condition and a desired mismatched impedance Z_{LM}. The mismatched condition results in a change in the reflected signal, which is observed at the power host via the directional coupler.

Theoretically, the pi-match network can transform the rectifier impedance value to any other impedance value to achieve an arbitrary Z_{LM}, but this complete coverage would require changing all three component values in the pi-match system. Because practical constraints prevent the switching of serial inductance values, the serial inductor must be a fixed value. Its value is dictated by the need to achieve the maximum power point match condition Z_{MATCH} when not performing load modulation. Thus, because of this fixed inductor constraint, achievable load modulation impedances with the chosen impedance transformation network will be those outside the shaded region of the Smith chart in Figure 6.3. To summarize, the real part of admittance for achievable modulation impedances must be smaller than 20mS.

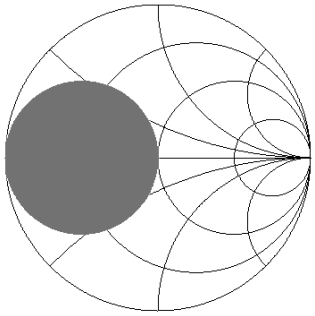

Figure 6.3: The shaded region shows unattainable impedance values for the proposed pi-match topology and a capacitive rectifier load.

6.2.2 Simulation Setup

The WPT system with load modulation is modeled and simulated in Cadence. A single-ended class E amplifier is modeled as the PA [26]. The output of the class E is connected to the input port of a directional coupler. The coupled port represents the reflected wave at the output port. The output port is connected to the transmitter coil.

The loop and coil parameters of a real four-coil system are extracted using a vector network analyzer (VNA) and computed by a MATLAB script based on the work in [33]. The transmit loop-coil and the receive loop-coil are critically coupled (coupling values are selected such that the impedance looking through the coil network is the same as the load impedance).

As the focus of this simulation is to get the general case result (not considering specific rectifier characteristics), passive load networks are employed to model both the Z_{MATCH} and Z_{LM} load conditions. These two loads are selected by an ideal switch, which is controlled by a digital signal modeling the information-carrying signal sent by the power client to the power host. The matched load condition Z_{MATCH} is set by default in the beginning of the transient simulation to give the Class E amplifier time to stabilize. Load modulation begins at t=100 μs, and involves alternating between load impedances of Z_{MATCH} and Z_{LM}. The

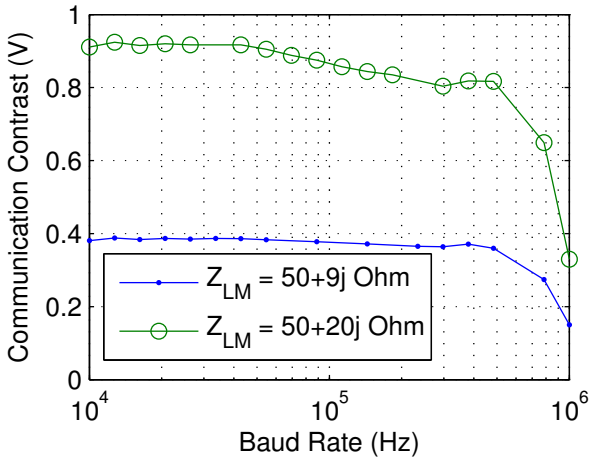

Figure 6.4: Communication contrast (the distance between points on the IQ plane, in Volts) as a function of the load modulation baud rate (symbol rate), in Hz. With a typical binary shift keying modulation scheme, the data rate (bps) will be equivalent to the baud rate. Using higher order modulation schemes such as QAM allows multiplicative increases in data rate.

Class E amplifier is designed for a 50 Ω output impedance, so Z_{LM} values are selected around 50 Ω. To provide different contrast, impedances are chosen along constant VSWR circles (1.2, 1.5, 2, 3, and 5). For each constant VSWR circle, we test all the real impedances, all impedances with 50 Ω resistance, and all impedances with 20 mS conductance. Though purely resistive Z_{LM} values over 50 Ω can't be achieved with the pi-match topology used herein, the trend of the system characteristics is still of interest as other matching topologies could potentially be used to achieve these impedances if desired.

The reflected wave as measured through a simulated directional coupler is recorded to disk, to be decoded by an IQ demodulator implemented in MATLAB. The received power P_{rx} is calculated as the sum of the average power of the two load impedances, and the input power P_{in} is measured with the DC power supplied to the PA. Because the PA is a non-linear switching amplifier, the input power at the MOSFET gate is constant, so we consider

drain efficiency rather than power added efficiency for the PA. Thus, we define our system efficiency as $P_{rx}/\ P_{in}$.

6.2.3 Communication Speed Limitation

Independent of how power efficiency is affected when doing load modulation, the communication bandwidth of load modulation is also inherently limited by the Q factor of the resonator.

$$Q = \frac{f_{operation}}{BW} \tag{6.1}$$

To evaluate the frequency response of this high Q WPT system, we estimate the cutoff frequency of the bandwidth by sweeping the load modulation baud rate from 10kHz to 1MHz. The result is presented in Figure 6.4 with two Z_{LM} values 50+9j Ω and 50+20j Ω. It shows that despite the different Z_{LM} value, the response stays similar until a 500kHz baud rate, which satisfies the requirement of many applications.

6.2.4 Communication Versus Power Trade-off

To understand how much the power efficiency of WPT with high Q resonators is affected while doing load modulation, we analyzed the uplink data at 100kHz baud rate. Figure 6.5a and Figure 6.5b show the communication contrast versus power efficiency as a function of the load modulation impedance as shown on a Smith chart. The points shown on the Smith charts for these two plots represent the equivalent reflected impedance seen by the PA. The two figures show that the power efficiency is inversely proportional to the communication contrast. Figure 6.5c and Figure 6.5d compare this trade-off dependence between the real LM impedance and imaginary LM impedance. To increase the communication contrast, the case when Z_{LM} is less than Z_{MATCH} is more sensitive than the case when Z_{LM} is greater than Z_{MATCH} (Figure 6.5c). For two points with the same absolute value and same real part of Z_{LM}, letting the imaginary part be positive rather than negative makes the communication contrast higher.

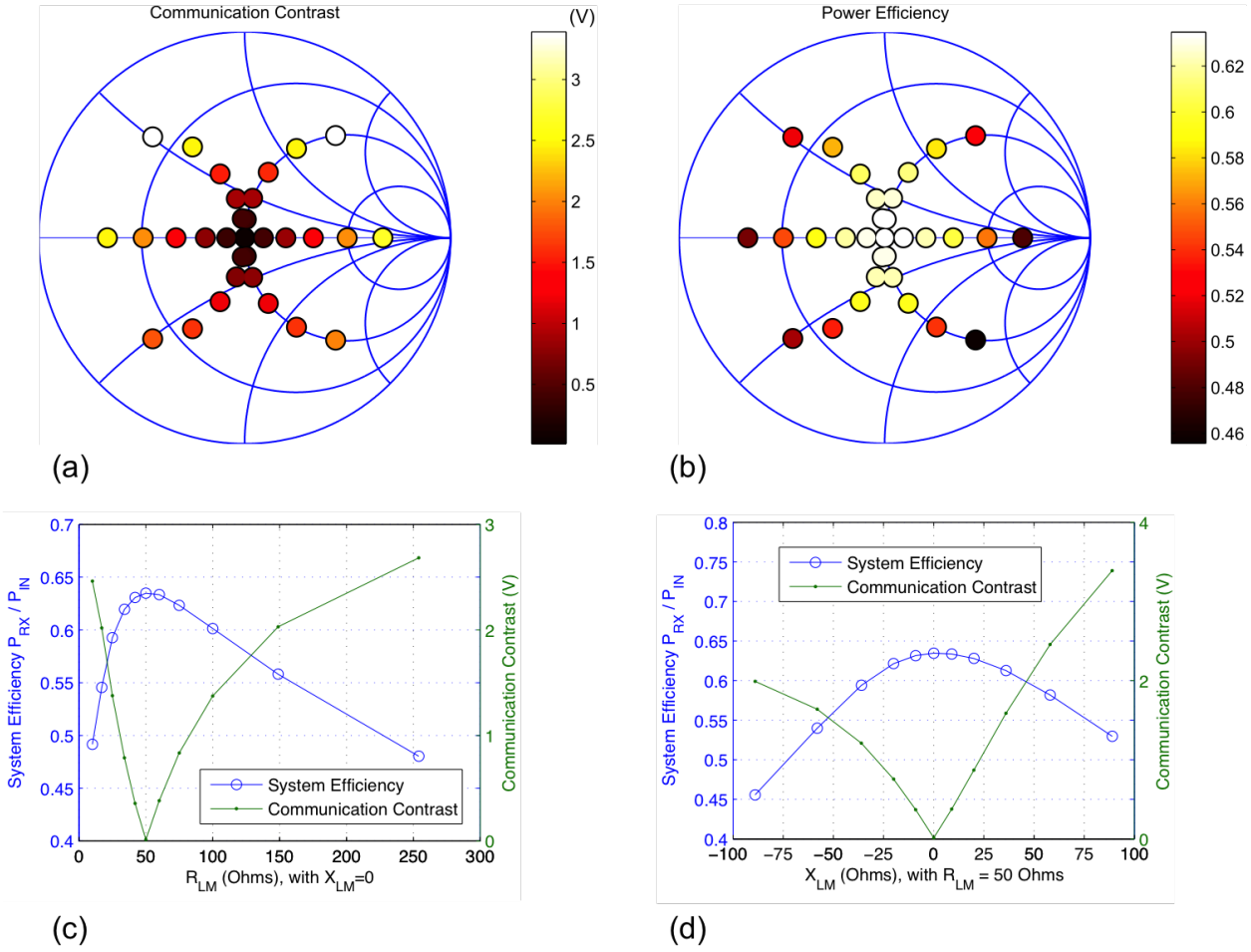

Figure 6.5: a).Communication contrast (the distance between points on the IQ plane, in Volts) as a function of effective load modulation impedance Z_{LM} experienced at the power host's PA. The power client switches between Z_{MATCH} and Z_{LM} at a rate of 100 kHz. b). Wireless power transfer efficiency (fraction of 1) as a function of effective load modulation impedance Z_{LM} experienced at the power host's PA. c). Communication contrast (the distance between points on the IQ plane, in Volts) and wireless power transfer efficiency as a function of real part of impedance seen by the power host's PA. d).Communication contrast (the distance between points on the IQ plane, in Volts) and wireless power transfer efficiency as a function of imaginary part of impedance seen by the power host's PA, when the real part is nearest the matched condition (50 Ohms).

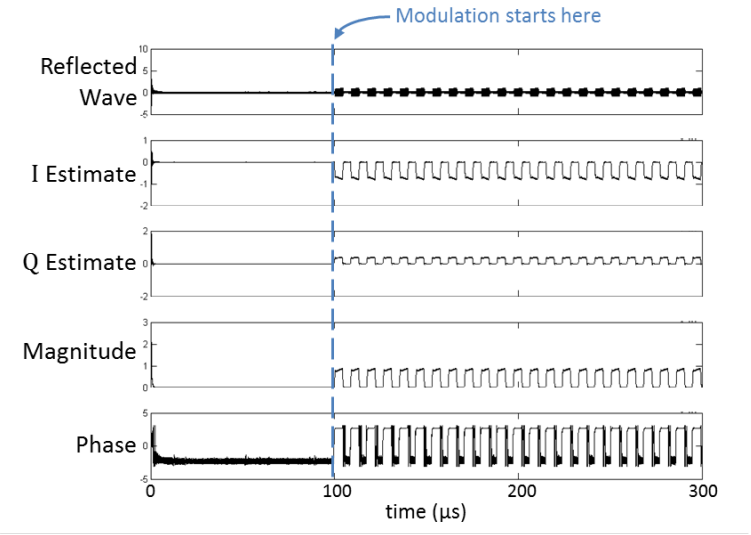

Figure 6.6: The time domain response of the reflected signal (as seen at the directional coupler) is shown along with the extracted In-phase (I) and Quadrature (Q) components of that signal and the corresponding magnitude and phase values.

Efficiency is reduced as communication contrast increases, but carefully choosing a point on the trade-off curve can still allow for good communication contrast while mitigating the impact of using load modulation. Figure 6.6 shows a good example of choosing based on this trade-off, with Z_{LM} set to $50 + 20j\ \Omega$. With this Z_{LM}, the system efficiency is 62.8% during load modulation mode while the maximum power efficiency is 63%, and the communication contrast at this point is 0.87 V (Figure 6.5c). Thus, even with decent communication contrast, the efficiency drop is only 0.2%. One reason the efficiency difference is very small is because of a reduction in the DC power consumption of the PA when Z_{LM} deviates from the matched condition, as the load impedance seen by the Class E PA also becomes more mismatched and results in less power dissipated by the amplifier. This reduced consumption slows the trend of efficiency degradation.

However, for a typical use case, a constant and stable load power is desirable. In order to maintain a constant load power as data transfer is occurring, the amplitude of the transmit signal could be adjusted during load modulation. An example of automatic load power tracking is presented in [45].

6.3 Extracting Location Information with Load Modulation in Relay Arrays

When we can't practically or affordably deploy the infrastructure required for a centrally controlled relay transmitter, an alternative to extend the power coverage of a simple single coil transmitter is to configure certain receivers in a group to themselves act as power relays for some of the time, rather than always simply acting as receivers. The selection of receivers to be reconfigured for optimal power relaying can reference the thorough studies on optimal relay configurations in Chapter 3 and Chapter 5. Based on our conclusions on optimal relay configurations, we can optimize the power delivery to any receiver if we can control all the receivers at once, and know the location relationships between each of them. However, even if we can add radio communication to coordinate the control of all the receivers at the same time, it is hard with the current localization technology to get the precise locations of the receivers. Location of the receivers, or knowledge about how best to deliver power to a receiver, is essential for implementation of a reconfigurable relay network.

Load modulation, suggested by its name, involves modulating the load impedance of a WPT receiver. In a wireless communication context, information to be transmitted is used to modulate the load impedance, resulting in a low power and simple communication method. However, in a wireless power transfer context, load modulation can be used in a different way; for coupled resonators WPT systems, a particular resonator can only impact others when it is close enough to them. For this reason, we propose to use load modulation to identify the relative locations between each device in a group of receivers.

Section 6.3.1 describes how each distributed receiver can identify the location of itself and the others in the system with load modulation.

6.3.1 Identify locations and number of receivers with load modulation

The motivation for each receiver knowing the locations and the number of receivers in the system is so that they can decide whether to configure themselves as relays, remove their interference from the neighbors by switching off, or to get charged themselves. We start by

assessing load modulation for location information extraction with the special case of when the receivers are placed one after another. Following the analysis of this simplified case, we next discuss what changes when the placement of the receivers is less constrained.

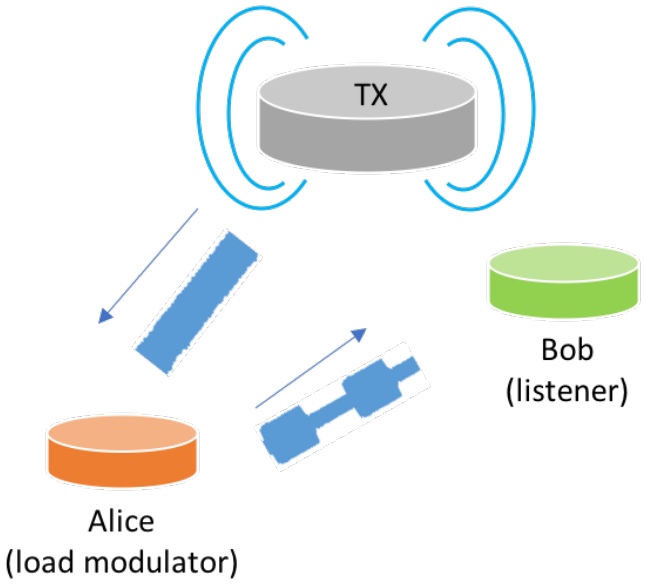

Figure 6.7: Illustration of two wireless power receivers (power clients) talking to each other by load modulating the power signal. Alice is the load modulator, and Bob is the listener.

To explain how a power client's relative location can be identified using load modulation, we use an example transaction between two power clients in the network. Fig.6.7 illustrates such a condition. Power client *alice* load modulates itself between two configurations: relay versus disabled. Nearby power client *bob* hears *alice*'s signal, and can take note of which configuration of *alice* (relay or disabled) is beneficial to itself by noting which of the two configurations results in *bob* receiving more power. One simple way to allow *bob* to distinguish between relay and disabled states of *alice* is by altering the duration of time during which *alice* dwells in each state. For example, if *alice* always spends a shorter time in relay mode than disabled, *bob* can easily determine which of the two modes is beneficial to its own power efficiency.

To identify the relative location of each distributed receiver in a system, we start with the simple case where receivers are placed side by side in a linear arrangement as shown in Fig.6.8.

Figure 6.8: Example of a line of side-by-side receivers waiting to be charged. The receivers can spend part of their time behaving as relays, allowing more distant receivers to attain much higher efficiency.

We evaluate the proposed method by setting up an experiment in which three receivers are placed one next to another as shown in Fig.6.9. Each receiver in listener mode is represented with a blue PCB, consisting of a coil and a loop. The loop is connected to an oscilloscope probe with an impedance of 1 MΩ. The receiver that load modulates (speaker mode) is

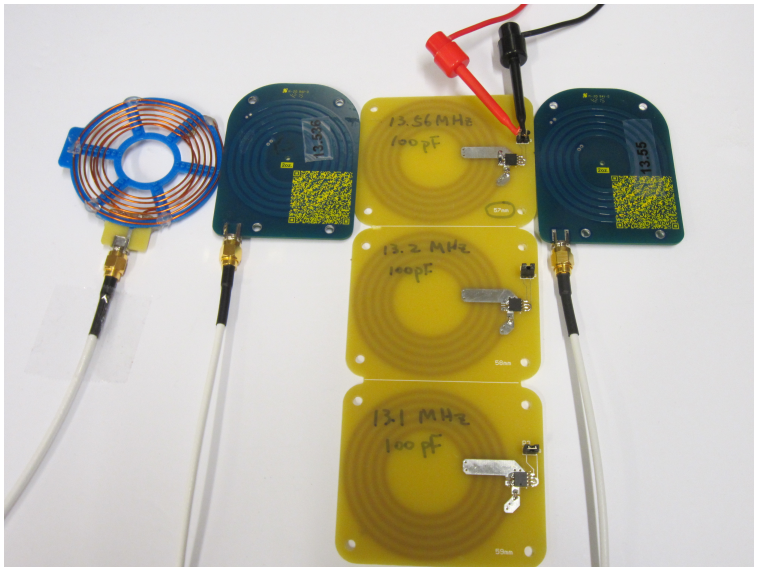

Figure 6.9: Test setup for load modulation in a linear array of receivers.

represented by a yellow coil, and has a switch connected in series to allow modulation. A load modulation signal is then fed to the switch. Fig.6.10 shows the load modulation signals received by two receivers in listener mode when load modulator is between them.

The duty cycle ratio between two configurations of the load modulation is chosen to be 3:7 to give a clear contrast on the pulse width difference when interpreting the results. In this test, the modulation frequency is set to 10 kHz. Because of the inverse relationship

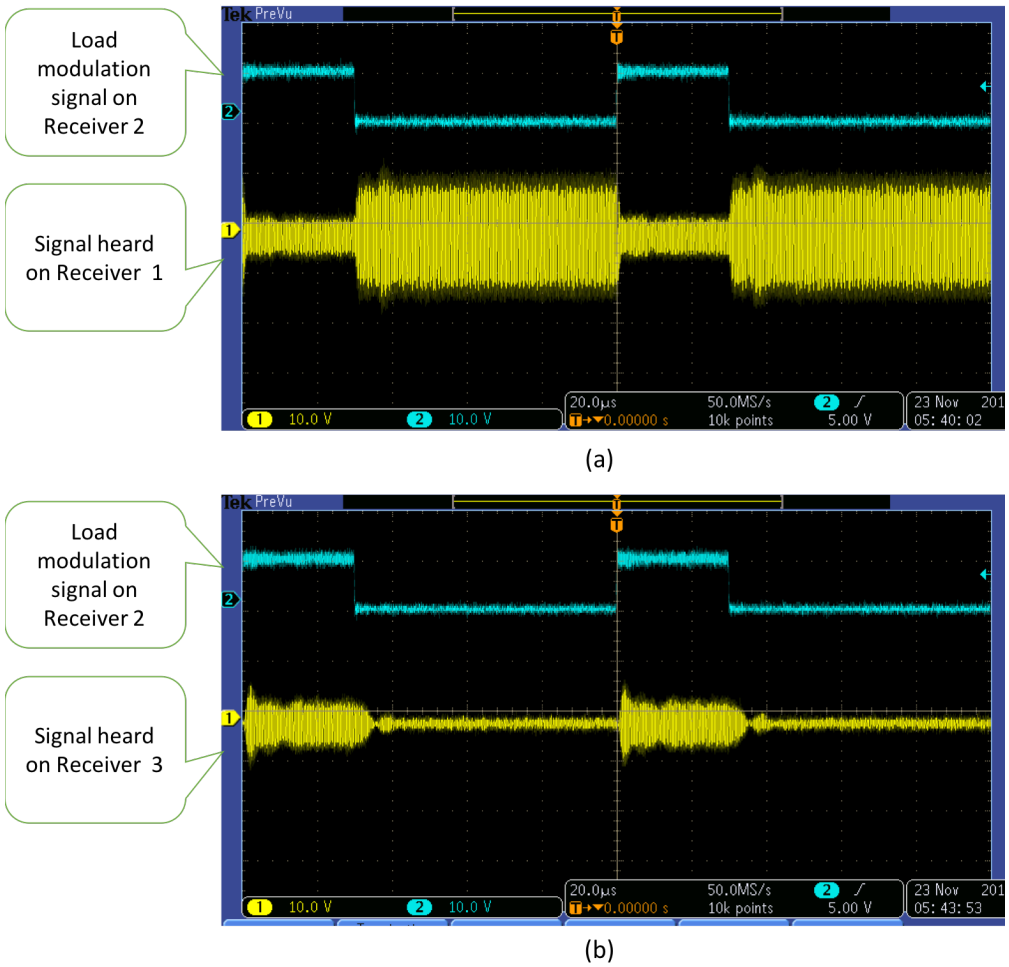

Figure 6.10: Load modulation signal from the same load modulator, as received by different listeners.

between the quality factor and the bandwidth of resonators, the frequency selected for the load modulation is constrained: The sum of the time the resonator is expected to be in a resonant relay state and the time the resonator continues ringing after it is turned off must be less than half of the load modulation period. The formula describing this relationship between the frequency of load modulation and the duty cycle chosen for the *high* pulse is shown in Eq.6.2:

$$f_{max} < (0.5 - duty\ cycle) \cdot \frac{\omega_0}{5Q} \tag{6.2}$$

where ω_0 is the resonant frequency of the coils, and Q is the quality factor of the coils. To obtain a positive frequency limit, the duty cycle should be less than 0.5. When the load modulation frequency is higher than f_{max} in Eq.6.2, the resonator does not reach steady state between switching events, and thus it will be difficult to discriminate between the two states on surrounding receivers. To demonstrate a load modulation frequency that is too high, Fig.6.11 shows the load modulation waveform with the same setup in Fig.6.10-b, but with 100 kHz modulation frequency instead of 10 kHz.

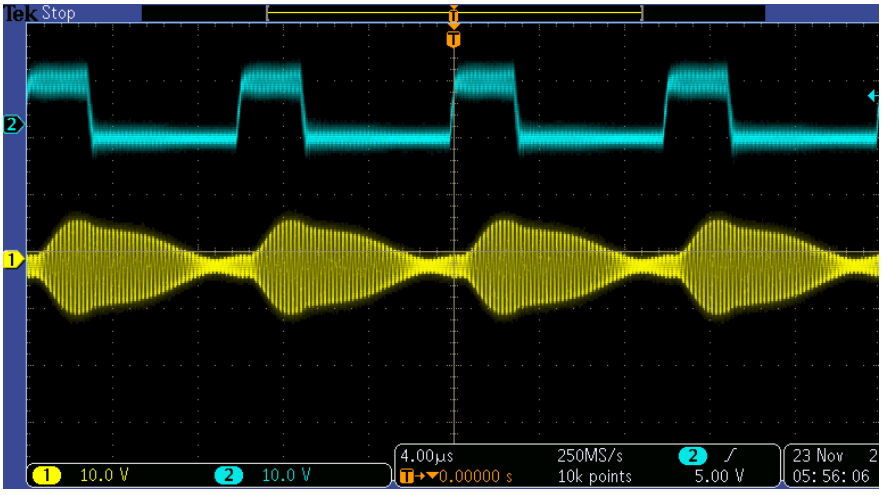

Figure 6.11: Load modulation waveform when the frequency of the modulation is 100 kHz, larger than f˙max of the coil system.

6.3.2 Location information extraction with clustered receivers

The previous section describes the method of extracting location information with load modulation in a special case: when receivers are located side-by-side in a linear pattern. This section briefly discusses how we can extract relative location using load modulation in a more general case, when receivers are clustered together but not necessarily in a linear arrangement.

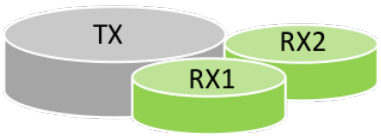

Figure 6.12: Example of clustered receivers waiting to be charged.

Fig.6.12 illustrates a cluster of receivers. In this case, the waveforms produced at a target receiver by load modulating another receiver in the system are not as clean as those seen in the linear arrangement. This is because, in this case, another pathway is present such that the two receivers can both receive power without the help of the other.

Fig.6.13 shows the load modulation signal received in such a system. When listener *bob* receives a signal similar to the waveform in Fig.6.13, it indicates that there is a receiver *alice* on a parallel path to *bob* and that *alice* does not need *bob*'s help to receive power. When this happens, *bob* can choose to disable itself more frequently to make *alice* charge quicker.

Another difference in use of load modulation for location extraction between clustered and linear arrangements is that, in some clustered cases, the speaker may be a competitor that shares the same relay path as the listener. When this condition happens, one may need to encode more information in the load modulation signal (as described in Section 6.2) for accurate relative location information.

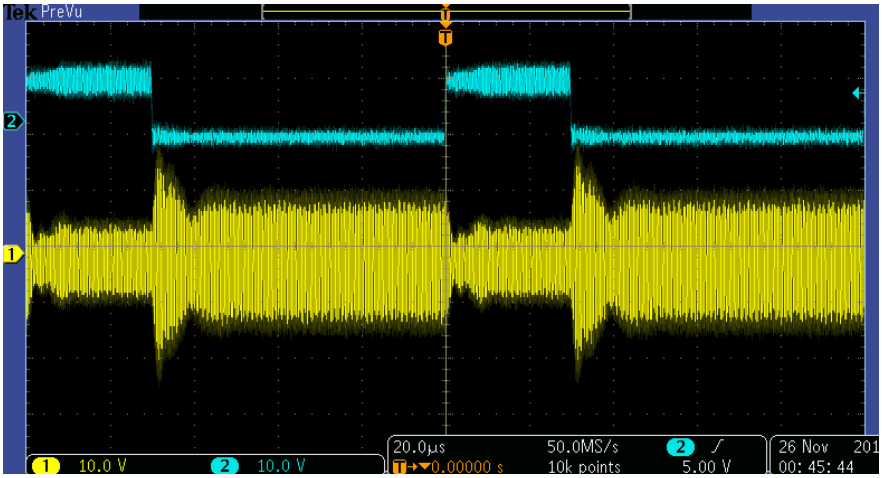

Figure 6.13: Load modulation signal received when two "clustered" receivers are placed side by side as illustrated in Fig.6.12. Channel 2 is the load modulation control signal of receiver 1 and Channel 1 is the received signal at receiver 2.

6.4 Conclusion

Load modulation has an advantage in being able to exchange data with low complexity and low cost of implementation. High Q power transfer coils limit the communication bandwidth, so load modulation may not be preferred for data streaming applications with wireless powered devices, but it is ideal for low bandwidth data exchange applications such as receiver detection and localization. By carefully selecting the load modulation impedance, we can have minimal impact on wireless power transfer efficiency. In addition, we have introduced the fundamental components of a method for extracting the location information within a network of receivers using load modulation. In summary, load modulation is a low cost, low complexity, practical way to add communication capability to wireless power transfer systems.

Chapter 7

SAFETY AND REGULATION OF COUPLED RESONATOR WIRELESS POWER TRANSFER SYSTEMS

7.1 Brief Overview of Regulations

With more wireless charging consumer devices entering the market, people have been benefiting from the convenience that wireless charging technology has brought. However, the concern for wireless power safety has also been raised. The safety concern is specifically focused around the interaction of electromagnetic (EM) fields in the human body.

Unlike X-ray or Gama rays, which belong to ionizing radiation and are a known health hazard, electromagnetic radiation belongs to non-ionizing radiation where the energy carrier does not have enough energy to ionize atoms or molecules, but it can induce current that causes tissue heating. In the U.S., any wireless device has to show the Federal Communications Commission (FCC) compliance, which is based on the recommendation conducted by independent organizations such as the International Commission on Non-Ionizing Radiation Protection (ICNIRP) and the IEEE-SA. The safety standard regulating human EM exposure is characterized by the specific absorption ratio (SAR). SAR is a measure of the rate of energy absorbed by the human tissue when exposed to an EM field. Figure 7.1 shows the EM exposure limit for the occupational exposure and general public exposure recommended by ICNIRP [20]. In addition, FCC specifies, for general population exposure, spatial peak SAR shall not exceed 1.6 W/kg as averaged over any 1g of tissue, except hands, wrists, feet and ankles, which shall not exceed 4 W/kg as averaged over any 10g of tissue [15]. Thus, SAR parameter is the most effective parameter to use for evaluating the EM impact on humans.

Exposure characteristics	Frequency range	Current density for head and trunk (mA m^{-2}) (rms)	Whole-body average SAR (W kg^{-1})	Localized SAR (head and trunk) (W kg^{-1})	Localized SAR (limbs) (W kg^{-1})
Occupational exposure	up to 1 Hz	40	—	—	—
	1–4 Hz	40/*f*	—	—	—
	4 Hz–1 kHz	10	—	—	—
	1–100 kHz	*f*/100	—	—	—
	100 kHz–10 MHz	*f*/100	0.4	10	20
	10 MHz–10 GHz	—	0.4	10	20
General public exposure	up to 1 Hz	8	—	—	—
	1–4 Hz	8/*f*	—	—	—
	4 Hz–1 kHz	2	—	—	—
	1–100 kHz	*f*/500	—	—	—
	100 kHz–10 MHz	*f*/500	0.08	2	4
	10 MHz–10 GHz	—	0.08	2	4

Figure 7.1: Basic restrictions for time varying electric and magnetic fields up to 10GHz for occupational exposure and general public exposure from [20]

7.2 Evaluation of Human Exposure to Magnetic Resonance Fields

SAR that characterizes the impact of EM exposure on humans is a function of the electric field E, electrical conductivity σ, and mass density of the material ρ under exposure.

$$\text{SAR} = \frac{\sigma E^2}{2\rho} \tag{7.1}$$

While σ and ρ are physical properties of human tissues, the intensity of the electric field is what characterizes the impact of magnetic resonance on humans. In a magnetic resonance system, when there are two high Q resonators critically coupled or under coupled [32], there exists a single resonant mode. In a single resonant mode, the two resonating magnetic fields are in-phase. However, when the magnetic resonance happens between two strongly coupled resonators, it induced two resonant modes that have two different field patterns, which effect human tissue differently ([32, 28, 37]). The magnetic fields in the lower frequency mode are in phase, but those in the higher frequency mode are out-of-phase [19].

Similarly, a magnetic resonant wireless power transfer system composed of an array of relay resonators can have multiple resonant modes [36], therefore the magnetic field pattern between the receiver and the relay coil can also be either in-phase or out-of-phase. Thus, it

is important to evaluate SAR for both the in-phase case and out-of-phase case.

In [13], Christ et al. studied the magnetic resonance with both measured and simulated dosimetry, but the wireless resonant model only includes the transmitter coil. Because magnetic resonance operates at near field where the existence of a receiver can change the field pattern, the result from [13] is not adequate to describe SAR with either in-phase or out-of-phase resonant fields. Therefore, our evaluation is conducted when both transmitter and receiver resonators are present. Because SAR in tissue is hard to measure directly with a physical instrument, the study is done through simulation with tissue parameters from [16] and [1]. In addition, to simulate wireless charging implanted devices, the receiver is modeled inside the tissue model.

7.2.1 Theory for Strongly Coupled Magnetic Resonator

The WPT configuration under test is the pair of magnetically coupled resonators shown in Figure 7.2. At the critical coupling point, there is only one frequency at which the system attains peak efficiency. This is called the critical coupling frequency. As the distance between the transmitter and receiver is reduced, the frequency of peak efficiency starts to split into two modes; a lower frequency peak and a higher frequency peak. These modes diverge in frequency as coupling increases.

In the lower frequency mode, the H fields of the resonators are in-phase; in the higher frequency mode, the resonator H fields are out-of-phase [28]. The resulting two modes can be understood by applying the coupling theory for microwave filters [19]. The coupling coefficient k which indicates the intensity of the coupling of the two resonators can be related by the two resonant frequencies as,

$$k = \frac{f_H^2 - f_L^2}{f_H^2 + f_L^2} \tag{7.2}$$

where f_L represents the lower resonant frequency and f_H represents the higher resonant frequency. In magnetically coupled resonator systems, if the coupling effect increases the stored magnetic flux, the resonant frequency shifts down from its critical-coupled frequency;

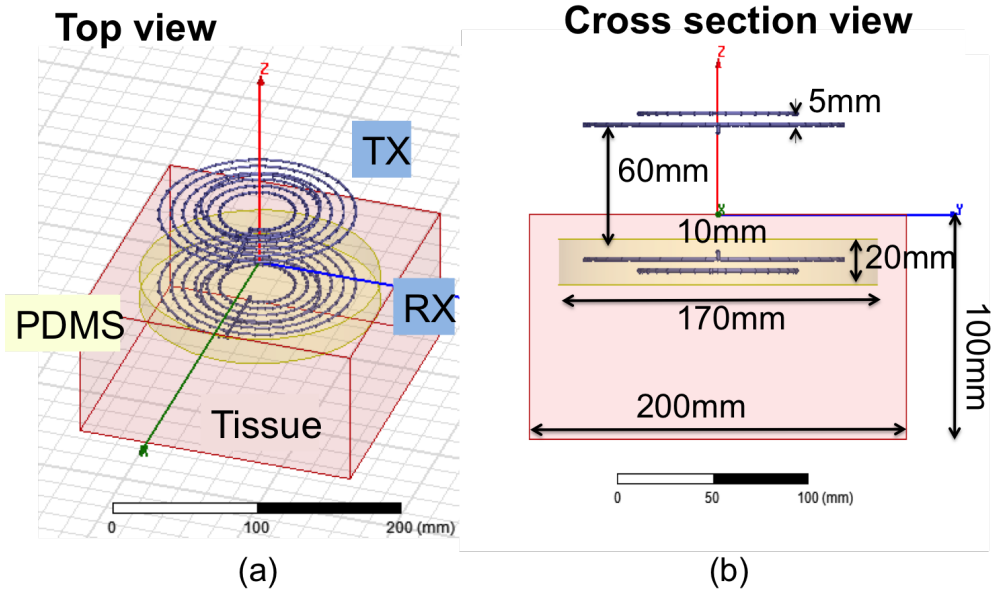

Figure 7.2: a) A strongly-coupled WPT system with an implanted receive coil is simulated to determine which of its two resonant modes results in lower SAR. The red box is a human tissue phantom, and the implanted receive coil is surrounded by a bio-compatible material shown in yellow. b) The side view of a) with scales.

otherwise, the resonant frequency shifts up from its critical-coupled frequency.

7.2.2 Modeling the Coils

The modeling of the simulation includes a 4-coil WPT system and a human tissue phantom in HFSS. Figure 7.2 shows the size and location of the model. The top loop-and-coil combination is the transmitter, and its location is swept vertically to achieve different coil separation distances. The bottom receiver is enclosed by a cylinder of has a Polydimethylsiloxane (PDMS) coating surrounded, highlighted in light yellow in the figure. PDMS is a material often used in implants for its bio-compatible properties. Because the strongest E field of the magnetic resonator is located near the wire, this bio-isolation can also reduce the E field induced in tissue, which reduces SAR. This encapsulating bio-compatible cylinder

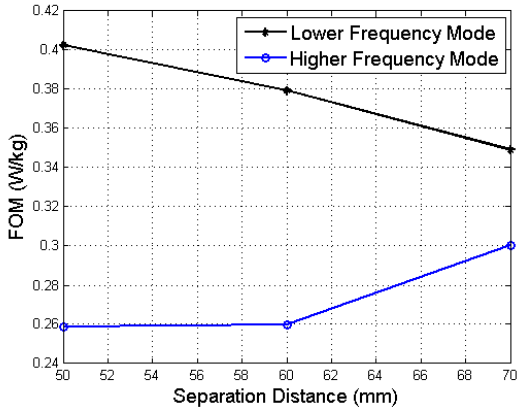

Figure 7.3: Comparing the figure of merit of SAR at two modes with varying distance.

has a radius of 85mm and a thickness of 20mm.

Because 13.56 MHz is one of the ISM bands that is popularly used by WPT systems, the operating frequency of the WPT system is designed near 13.56 MHz. However, in the over-coupled regime the two frequencies of peak efficiency will diverge, and therefore the frequency corresponding to maximum power transfer will be shifted away from the design frequency of 13.56 MHz. In this work, the coupling is adjusted such that the difference between the upper and lower peak efficiency frequencies is 4 MHz.

In HFSS, each turn of the coil and loop is modeled with 36 segment elements. Capacitors are modeled as lumped elements to form resonance. The design parameters for the system are listed in Table 7.1. The transmitter and receiver coils are symmetrically designed and the simulated result of $|S21|^2$ (WPT efficiency) is 94% at critical coupling at 14.5 MHz. Because the topic of coil design for high efficiency is not within the scope of this paper, the details of how the coil system is designed are not included, but one can reference tuning techniques from [33].

Table 7.1: Parameters for the Coil and the Loop

Coil Parameters	**Value**
Coil inner radius (mm)	22
Number of turns	6
Change of radius (mm)	8.5
Wire radius (mm)	0.85
Tuning capacitor (pF)	33
Loop Parameters	**Value**
Radius (mm)	42
Tuning capacitor (pF)	660
Loop to coil Distance (mm)	5

7.2.3 Modeling the Tissue

The tissue is modeled as a homogeneous muscle cube shown as the pink box in Figure 7.2, which has the dimension of 200mm×200mm×100mm. The frequency-dependent electrical parameters of muscle are listed in Table 7.2 [16] with density 1090 kg/m^3 [1].

Even though it is more accurate to use an anatomical human body model [14] or tissue recipe for the WPT simulation in the 10 MHz band because different layers (such as skin, fat and muscle) of human body has different dielectric properties, it is reasonable to use a homogeneous tissue model for this study because we intend to compare the different characteristics of the SAR distribution in one tissue type. HFSS computes SAR with Eq. 7.1. The conductivity σ is defined in the equation below,

$$\sigma = \omega\epsilon_0\epsilon_r tan\delta \tag{7.3}$$

where the simulation parameters used are listed in Table 7.2. A large air box is placed to surround this system and acts as the radiation boundary, but it is not shown in Figure 7.2.

Table 7.2: Electrical Parameters of Muscle

Frequency (MHz)	ϵ_r	$tan\delta$	σ (S/m)
12.25	147.97	6.1922	0.6244
12.5	145.98	6.1582	0.62515
12.75	144.08	6.1244	0.62589
14.75	131.35	5.8575	0.63131
15	130.01	5.8249	0.63193
15.5	127.47	5.7603	0.63315

7.2.4 Result and Analysis

The system is modeled using the Finite Element Method (FEM) in HFSS. The input port and the output port connecting the capacitor boundary and the loop are modeled as 50 Ω lumped ports. The basis function of the solution setup is selected as zero order, because the coil size is much smaller than the wavelength. Finally, the frequency resolution is set to 0.125MHz.

In all the simulations, the input source is set to a power level of 1 Watt. The SAR distribution for each of the two resonant modes is computed with three separation distances, 50mm, 60mm, and 70mm. The resulting distributions for the high and low frequency resonant modes are compared. Parameters including SAR 1g, SAR 10g and whole tissue SAR are collected in both resonant modes for the three locations (Table 7.3). The efficiency in each test ($|S21|^2$) is also included in the figure of merit (FOM) to compare between the low frequency mode and high frequency mode. Because the efficiency for each case is different, it is not fair to compare the SAR value alone with different receive power levels. Thus, we define the FOM using the normalized SAR and S21:

$$\text{FOM} = \frac{\text{normalized SAR}}{|\text{S21}|^2} \tag{7.4}$$

where normalized SAR is calculated by dividing SAR by the input power. In this way, either having a bad SAR performance or a low WPT efficiency will result in a large FOM, which is less desirable for an implanted WPT system. Figure 7.3 compares the FOM of the two modes at the three separation distances. It should be noted that, although the FOM is smaller as separation distance increases of the lower frequency mode, this does not necessarily mean that this is the preferred setup as the efficiency also decreases. However, as can be seen in the plot, the higher frequency mode is always better than the lower frequency mode for each separation distance.

Table 7.3: SAR comparison when varying distance and resonant mode

Dist (mm)	Freq (MHz)	S21 (dB)	Max SAR 1g (W/kg)	Max SAR 10g (W/kg)	Whole Tissue SAR	FOM
50	12.25	-2.39	0.232	0.198	3.80e-02	0.403
60	12.5	-2.79	0.200	0.166	3.33e-02	0.379
70	12.75	-3.67	0.150	0.122	2.52e-02	0.349
50	15.5	-1.64	0.177	0.133	1.76e-02	0.259
60	15	-2.26	0.155	0.116	1.65e-02	0.260
70	14.75	-3.12	0.147	0.111	1.61e-02	0.301

Fig 7.4 shows the field patterns at the 60mm separation case, including H field, E field and SAR 1g. The left column represents the result of the lower frequency mode at 12.5 MHz and the right column shows the higher frequency mode at 15 MHz. The H field of the higher frequency mode has a null in the center compared to the lower frequency mode, which has the same result as that in [28]. The E field patterns inside the tissue are quite different between the modes. At the lower frequency mode, the location with the greater E field intensity is near the top of the tissue; whereas at the higher frequency mode, the higher intensity E field is located behind the receive coil. The SAR 1g field follows the same trend

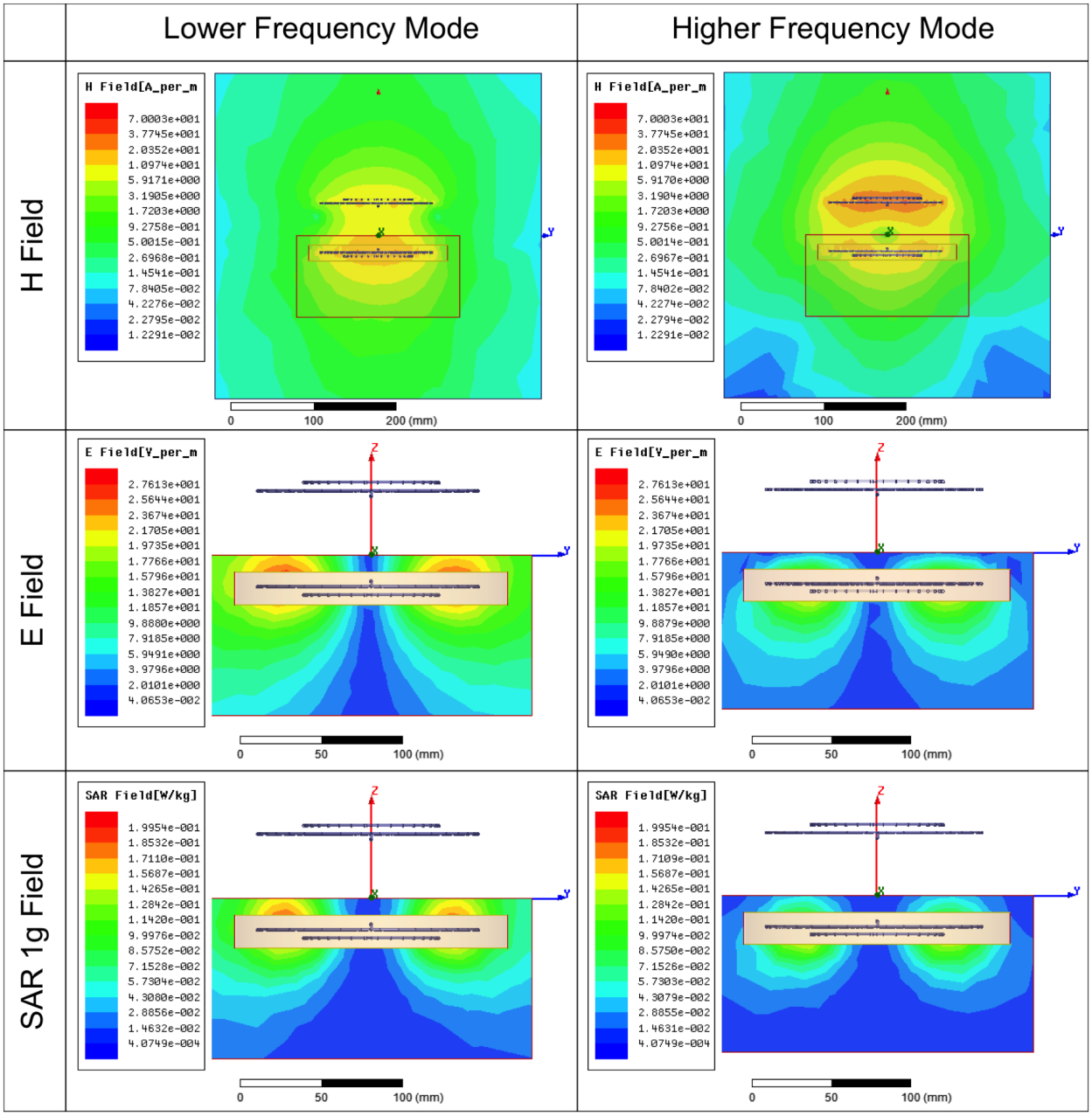

Figure 7.4: The YZ-plane cross section of field patterns when the transmitter and receiver separation distance is 60mm with input power of 1W. They are, from top to bottom, H field, E field, and SAR 1g field. The left column shows the field patterns of the lower frequency mode, and the right column shows those of the higher frequency mode. The E field pattern is captured at phase=0; the H field pattern is captured at phase=90; the SAR plot is the average SAR over 1g of tissue. The axes of each field pair are scaled to be the same so that a visual comparison can be made between low and high frequency mode plots.

as the E field pattern. To compare the field pattern of each case more clearly, the axes are scaled to be the same, but both the peak E field and SAR 1g field have lower maxima in the higher frequency mode than in the lower frequency mode.

7.3 Conclusion

The SAR value in the two resonant modes of the magnetic resonance system are different due to the different field pattern at different resonant mode. In this particular test setup, the higher frequency mode has higher power transfer efficiency while having a lower SAR. Thus, when using wireless power system with multiple resonant modes, it is better to check the field pattern in addition to efficiency to insure the least EM impact on human or animals.

Chapter 8

SUMMARY AND CONCLUSION

In order to apply wireless power technology to solve existing power solution challenges in industrial and medical fields, the range needs to be improved from the current state of the art. This dissertation has focused on developing a system for large area wireless power transfer with reconfigurable coupled relay resonators. This technology can achieve a wireless power transfer range that is larger than what a traditional single coil magnetic resonance transmitter can achieve, while preserving the positive features of the magnetic resonance system: efficiency, power output capability and safety.

Particularly, we have characterized techniques for optimizing coverage and efficiency for one-dimensional (1D) and two-dimensional (2D) relay arrays, through which we introduced a new adaptive tuning technique called spatial tuning. Spatial tuning is the changing of resonant mode to improve efficiency at the operating frequency, and is done by adding new resonators to or removing resonators from an existing group of resonators.

We have introduced a platform consisting of a centrally controlled array of reconfigurable relays (CARR) that implements spatial tuning. It is designed to extend the coverage of wireless power transfer in a 2D space. Three power steering algorithms have been designed and tested for different applications of CARR. One algorithm is designed to seamlessly track and deliver power to one moving target, and can be applied to power a patient's implanted devices. The second algorithm is designed to track and deliver power to multiple moving targets. It can be used for charging multiple electronics without much alignment constraint or used by researchers to power the implanted devices of test subjects in a cage. The third algorithm is a broadcasting scheme that time-multiplexes the power all across the space.

CARR is one example platform that uses reconfigurable coupled relay resonators for

large area wireless power transfer. We also demonstrated another approach to large area coverage with reconfigurable relays. In this alternate scheme, rather than requiring the infrastructure of CARR, there is only one simple single coil transmitter, and the receivers can be reconfigured into either relays or receivers to relay power to other receivers or be charged themselves. The challenge for such a system is for each receiver to obtain information from the others and make a configuration decision. We have demonstrated the use of load modulation as the communication method and a practical way to identify the relative location of each receiver in the network.

Lastly, a method of assessing the safety measure of magnetically coupled resonator systems is described, with an example of simulating specific absorption rate (SAR) of implanted coils. Through analyzing the difference in SAR between two resonant modes in the over-coupled region, we have concluded that using the mode with least field density and shape results in lower SAR, and therefore is safer. In this case, this preferable mode is the resonant mode with the higher frequency, that has out-of-phase resonant fields.

In conclusion, we believe that this thesis has made significant progress towards the goal of making large area wireless power transfer more practical and affordable.

BIBLIOGRAPHY

[1] ITIS Database for Tissue Properties. http://www.itis.ethz.ch/itis-for-health/tissue-properties/database/density/ Accessed: Feb, 2015.

[2] "A4WP Rezence Specification". Technical Report V1, Alliance for Wireless Power, 2014. http://www.rezence.com/technology/technical-specification.

[3] Wireless power specification part 1. Technical Report V1.1.2, Wireless Power Consortium, 2014. http://www.wirelesspowerconsortium.com/downloads/wireless-power-specification-part-1.html.

[4] S. Atluri and M. Ghovanloo. A wideband power-efficient inductive wireless link for implantable microelectronic devices using multiple carriers. In *Circuits and Systems, 2006. ISCAS 2006. Proceedings. 2006 IEEE International Symposium on*, pages 4 pp.–1134, May 2006.

[5] S. I. Babic and C. Akyel. Calculating mutual inductance between circular coils with inclined axes in air. *IEEE Transactions on Magnetics*, 44(7):1743–1750, July 2008.

[6] J. Besnoff, M. Abbasi, and D. S. Ricketts. High data-rate communication in near-field rfid and wireless power using higher order modulation. *IEEE Transactions on Microwave Theory and Techniques*, 64(2):401–413, Feb 2016.

[7] J. Besnoff, M. Abbasi, and D. S. Ricketts. Ultrahigh-data-rate communication and efficient wireless power transfer at 13.56 mhz. *IEEE Antennas and Wireless Propagation Letters*, 16:2634–2637, 2017.

[8] J. Besnoff and D. S. Ricketts. Near field wireless power transfer and quadrature amplitude modulated (qam) communication link. In *2015 IEEE Wireless Power Transfer Conference (WPTC)*, pages 1–4, May 2015.

[9] William C. Brown. History and status of beamed power technology and applications at 2.45 gigahertz. Technical report, Microwave and Power Tube Division, Raytheon Company, 190 Willow Street, Waltham, MA.

[10] William C. Brown. Experiments involving a microwave beam to power and position a helicopter. *IEEE Transactions on Aerospace and Electronic Systems*, AES-5(5):692–702, Sept 1969.

[11] J. J. Casanova, Zhen Ning Low, Jenshan Lin, and R. Tseng. Transmitting coil achieving uniform magnetic field distribution for planar wireless power transfer system. In *2009 IEEE Radio and Wireless Symposium*, pages 530–533, Jan 2009.

[12] Y. Cheng and Y. Shu. A new analytical calculation of the mutual inductance of the coaxial spiral rectangular coils. *IEEE Transactions on Magnetics*, 50(4):1–6, April 2014.

[13] A. Christ, M.G. Douglas, J.M. Roman, E.B. Cooper, A.P. Sample, B.H. Waters, J.R. Smith, and N. Kuster. Evaluation of wireless resonant power transfer systems with human electromagnetic exposure limits. *Electromagnetic Compatibility, IEEE Transactions on*, 55(2):265–274, April 2013.

[14] Andreas Christ, Wolfgang Kainz, Eckhart G Hahn, et al. The virtual family–development of surface-based anatomical models of two adults and two children for dosimetric simulations. *Physics in Medicine and Biology*, 55(2):N23, 2010.

[15] FCC. "Report and Order, FCC 96-326", 1996. https://transition.fcc.gov/Bureaus /Engineering˙Technology/Orders/1996/fcc96326.pdf.

[16] C Gabriel, S Gabriel, and E Corthout. The dielectric properties of biological tissues: I. literature survey. *Physics in Medicine and Biology*, 41(11):2231, 1996.

[17] P. Grover and A. Sahai. Shannon meets tesla: Wireless information and power transfer. In *Information Theory Proceedings (ISIT), 2010 IEEE International Symposium on*, pages 2363–2367, June 2010.

[18] John S. Ho, Yuji Tanabe, Shrivats Mohan Iyer, Amelia J. Christensen, Logan Grosenick, Karl Deisseroth, Scott L. Delp, and Ada S. Y. Poon. Self-tracking energy transfer for neural stimulation in untethered mice. *Phys. Rev. Applied*, 4:024001, Aug 2015.

[19] Jia-Sheng Hong and M. J. Lancaster. *Microstrip Filters for RF/Microwave Applications*. Wiley, 1st edition edition, 2001.

[20] ICNIRP. Guidelines for limiting exposure to time-varying electric, mag- netic and electromagnetic fields (up to 300 ghz), 1998.

[21] K. Kaiser. *Electromagnetic Compatibility Handbook*. CRC Press, 2004.

[22] Mehdi Kiani, Uei-Ming Jow, and Maysam Ghovanloo. Design and optimization of a 3-coil inductive link for efficient wireless power transmission. *IEEE Trans Biomed Circuits Syst*, 99:1–1, Jul 2011. 21922034[pmid].

[23] J. Kim, H. C. Son, K. H. Kim, and Y. J. Park. Efficiency analysis of magnetic resonance wireless power transfer with intermediate resonant coil. *IEEE Antennas and Wireless Propagation Letters*, 10:389–392, 2011.

[24] André Kurs, Aristeidis Karalis, Robert Moffatt, J. D. Joannopoulos, Peter Fisher, and Marin Soljačić. Wireless power transfer via strongly coupled magnetic resonances. *Science*, 317(5834):83–86, 2007.

[25] Byunghun Lee, M. Ghovanloo, and Dukju Ahn. Towards a three-phase time-multiplexed planar power transmission to distributed implants. In *Circuits and Systems (ISCAS), 2015 IEEE International Symposium on*, pages 1770–1773, May 2015.

[26] Zhen Ning Low, R.A. Chinga, Ryan Tseng, and Jenshan Lin. Design and test of a high-power high-efficiency loosely coupled planar wireless power transfer system. *Industrial Electronics, IEEE Transactions on*, 56(5):1801–1812, May 2009.

[27] S. Mandal and R. Sarpeshkar. Power-efficient impedance-modulation wireless data links for biomedical implants. *Biomedical Circuits and Systems, IEEE Transactions on*, 2(4):301–315, Dec 2008.

[28] SangWook Park, EunHa Kim, Kanako Wake, and Soichi Watanabe. Dosimetry for two modes of resonance-based wireless power transfer system. In *Electromagnetic Compatibility, Tokyo (EMC'14/Tokyo), 2014 International Symposium on*, pages 210–213, May 2014.

[29] Clayton R. Paul. *Inductance: Loop and Partial*. Wiley, 2009.

[30] David M. Pozar. *Microwave Engineering*. Wiley, 4th edition edition, 2011.

[31] A. P. Sample, B. H. Waters, S. T. Wisdom, and J. R. Smith. Enabling seamless wireless power delivery in dynamic environments. *Proceedings of the IEEE*, 101(6):1343–1358, June 2013.

[32] A.P. Sample, D.A. Meyer, and J.R. Smith. Analysis, experimental results, and range adaptation of magnetically coupled resonators for wireless power transfer. *Industrial Electronics, IEEE Transactions on*, 58(2):544–554, Feb 2011.

[33] A.P. Sample, B.H. Waters, S.T. Wisdom, and J.R. Smith. Enabling seamless wireless power delivery in dynamic environments. *Proceedings of the IEEE*, 101(6):1343–1358, June 2013.

[34] X. Shi, H. Lee, V. Jain, and J. R. Smith. Coil geometry optimization for wireless power delivery to moving receivers. In *2018 IEEE Wireless Power Transfer Conference (WPTC)*, pages 1–4, June 2018.

[35] X. Shi, A. N. Parks, B. H. Waters, and J. R. Smith. Co-optimization of efficiency and load modulation data rate in a wireless power transfer system. In *2015 IEEE International Symposium on Circuits and Systems (ISCAS)*, pages 698–701, May 2015.

[36] X. Shi and J. R. Smith. Large area wireless power via a planar array of coupled resonators. In *2016 International Workshop on Antenna Technology (iWAT)*, pages 200–203, Feb 2016.

[37] X. Shi, B. H. Waters, and J. R. Smith. Sar distribution for a strongly coupled resonant wireless power transfer system. In *2015 IEEE Wireless Power Transfer Conference (WPTC)*, pages 1–4, May 2015.

[38] V. Talla, V. Ranganathan, B. Mahoney, and J. R. Smith. Dual band wireless power and bi-directional data link for implanted devices in 65 nm cmos. In *2016 IEEE International Symposium on Circuits and Systems (ISCAS)*, pages 658–661, May 2016.

[39] Nikola Tesla. The future of wireless art. In *Wireless telegraphy & telephony*, pages 67–71, 1908.

[40] Bingnan Wang, W. Yerazunis, and Koon Hoo Teo. Wireless power transfer: Metamaterials and array of coupled resonators. *Proceedings of the IEEE*, 101(6):1359–1368, June 2013.

[41] B. H. Waters. *Adaptive Wireless Power for Ventricular Assist Devices*. Ph.D. dissertation, Dept. of Elect. Eng., Univ. Washington, Seattle, 2015.

[42] B.H. Waters, P.R. Fidelman, J.D. Raines, and J.R. Smith. Simultaneously tuning and powering multiple wirelessly powered devices. In *Wireless Power Transfer Conference (WPTC), 2015 IEEE*, pages 1–4, May 2015.

[43] B.H. Waters, B.J. Mahoney, Gunbok Lee, and J.R. Smith. Optimal coil size ratios for wireless power transfer applications. In *2014 IEEE International Symposium on Circuits and Systems (ISCAS)*, pages 2045–2048, June 2014.

[44] B.H. Waters, B.J. Mahoney, V. Ranganathan, and J.R. Smith. Power delivery and leakage field control using an adaptive phased array wireless power system. *Power Electronics, IEEE Transactions on*, 30(11):6298–6309, Nov 2015.

[45] B.H. Waters, A.P. Sample, P. Bonde, and J.R. Smith. Powering a ventricular assist device (vad) with the free-range resonant electrical energy delivery (free-d) system. *Proceedings of the IEEE*, 100(1):138–149, Jan 2012.

[46] G. Yilmaz and C. Dehollain. Capacitive detuning optimization for wireless uplink communication in neural implants. In *Advances in Sensors and Interfaces (IWASI), 2013 5th IEEE International Workshop on*, pages 45–50, June 2013.

[47] F. Zhang, S. A. Hackworth, Weinong Fu, and M. Sun. The relay effect on wireless power transfer using witricity. In *Digests of the 2010 14th Biennial IEEE Conference on Electromagnetic Field Computation*, pages 1–1, May 2010.

[48] Xiu Zhang, S.L. Ho, and W.N. Fu. Quantitative design and analysis of relay resonators in wireless power transfer system. *Magnetics, IEEE Transactions on*, 48(11):4026–4029, Nov 2012.

[49] Yi Zhao, Huaye Li, Saman Naderiparizi, Aaron Parks, and Joshua R. Smith. Low-cost wireless power efficiency optimization of the nfc tag through switchable receiver antenna. *Wireless Power Transfer*, 5(2):8796, 2018.

[50] W. X. Zhong, C. K. Lee, and S. Y. Hui. Wireless power domino-resonator systems with noncoaxial axes and circular structures. *IEEE Transactions on Power Electronics*, 27(11):4750–4762, Nov 2012.